THESIS FOR THE DEGREE OF DOCTOR OF PHILOSOPHY

Formation and Decay of Multiply-Charged Molecules upon Single-Photon Excitation

Måns Wallner

Department of Physics
University of Gothenburg
Gothenburg, Sweden, 2024

Doctoral Dissertation in Physics

Department of Physics
University of Gothenburg
SE-412 96 Gothenburg, Sweden

Main supervisor:
Raimund Feifel, Department of Physics, University of Gothenburg
Examiner:
Mattias Marklund, Department of Physics, University of Gothenburg
Opponent:
Arnaldo Naves de Brito, Department of Applied Physics, Campinas University, Brazil

© Måns Wallner 2024
ISBN: 978-91-8069-669-2 (printed)
ISBN: 978-91-8069-670-8 (pdf)
URL: http://hdl.handle.net/2077/80060

Cover: Illustration of a three dimensional coincidence map of the formation of doubly ionised electronic states versus ion mass/charge of OCS, measured at a photon energy of 41 eV. The intensity is on a logarithmic scale.

SVANENMÄRKET
Trycksak
3041 0234

Printed by Stema, Borås, 2024
Typeset in LaTeX.

“Some say the world will end in fire, some say in ice.”

- Robert Frost

Abstract

This thesis presents the investigation of dissociative multi-ionisation processes in gas-phase molecules through single photon absorption, employing a combination of ion spectrometry and electron spectroscopy, relying on a magnetic bottle time-of-flight principle. This method is pivotal for capturing all electrons emitted during ionisation, enabled by its unique electric and magnetic field configuration.

The initial part of the thesis (Paper I) explores Coulomb explosion in CD_3I, induced by deep inner-shell ionisation with hard X-rays. The study examines core vacancy relaxation through Auger-Meitner cascades. Using a a comparatively simple model, the relaxation and subsequent dynamics of Coulomb explosions are simulated, yielding results that align well with experimental data for medium charge states, although limitations are noted for higher charge states. The research provides insights into the distribution of final charge states following L-shell ionisation, including the involvement of rapid Coster-Kronig transitions.

Papers II-V focus on the dissociation mechanisms of small molecules (SO_2, OCS, and HNCS) upon single photon double valence ionisation, employing the same experimental approach. Paper II discusses an unconventional dissociation mechanism in SO_2 leading to the unexpected charge retaining SO^{2+} species via autoionisation of the super-excited 2h-1p Rydberg state of SO_2^{+*} at long bond distances. Paper III reports on the production of molecular oxygen, O_2, in an ionic pathway via a newly revealed metastable state of $O\text{-}O\text{-}S^{2+}$. Paper IV examines bond rearrangement upon double ionisation in OCS, establishing a newly identified metastable isomer COS^{++}. Paper V details the dissociation pathways of the main fragmentation channels of HNCS. Each paper contributes to a broader understanding of molecular behaviour under double ionisation.

Paper VI focuses on the sequential three-body dissociation mechanisms leading to unusual shapes, that also deviate from the expected limiting slope of $-m_B/m_{BC}$. Two isomers of perflouro-propyl iodide are found to sequentially break into three fragments, $ABC^{++} \rightarrow A^+ + BC^+$ followed by $BC^+ \rightarrow B^+ + C$, where simulations suggest that the bow-tie and twisted shapes arise from femtosecond secondary lifetimes. At these short time scales the BC^+ is placed well within the effective Coulomb range of A^+.

Overall, this thesis sheds light on the complex dynamics of dissociative multi-ionisation in several molecules, paving the way for future research in molecular dynamics and chemical reactions in more complex environments.

Keywords: Molecule, electrons, ions, dissociation, fragmentation, coincidence, time of flight, VUV, X-radiation.

Svensk populärvetenskaplig sammanfattning

Denna avhandling handlar om molekyler och hur de bryter isär när de utsätts för starkt ljus. Molekyler är en sammansättning av flera atomer som binds ihop genom att dela elektroner. Elektronerna som binder ihop atomerna kan växelverka med ljus och på så sätt absorbera dess energi. Energin omvandlas till rörelseenergi, vilket kan leda till att elektronen flyr i en process som kallas jonisering. Den kallas så eftersom processen skapar en jon, en positivt laddad atom eller molekyl. Om en elektron som är ansvarig för att binda ihop molekylen lämnar kan det leda till att bindningarna bryts och molekylen delar på sig.

Elektroner växelverkar med protonerna i atomenkärnan med hjälp av den elektromagnetiska kraften. På så sätt kan man tänka sig att electronerna försätter sig i banor kring atomen, likt hur planeterna i vårt solsystem kretsar kring solen. Denna semi-klassiska förklaringsmodell var inte tillräcklig för att förklara alla delar av atomens fysik, vilket i början av 1900-talet ledde till utveckligen av kvantmekanik.

Kvantmekaniken kunde förklara flera av de tidigare okända fenomen som uppstår på atomär nivå. Genom kvantmekaniken blev det exempelvis möjligt att förstå varför elektroner inte störtar in i atomkärnan, trots deras negativa laddning och attraktionen till de positivt laddade protonerna. I stället för att betrakta elektronernas rörelse som klassiska banor, beskriver kvantmekaniken dem med hjälp av vågfunktioner som representerar sannolikhetsfördelningar. Detta innebär att elektronerna inte har en exakt position och hastighet, utan snarare en sannolikhet att finnas på olika platser runt kärnan. Kvantmekaniken tillhandahåller även förklaringar till hur kemiska bindningar uppstår. I en molekyl delar elektroner från olika atomer vågfunktioner, vilket skapar en stark bindning mellan atomerna.

Ljus färdas i en stråle som består av massa partiklar, som kallas för fotoner. När en av fotonerna träffar en molekyl kan energin absorberas och denna energi kan inte förintas utan måste ta vägen någonstans. En utväg är att det blir rörelseenergi för en av molekylens elektroner som kan leda till att den lämnar molekylen. Fotonens energi kan delas mellan flera elektroner och om energin är tillräckligt hög kan det leda till att två eller fler elektroner lämnar molekylen samtidigt, och molekylen blir flerfaldigt positivt laddad. Om det skapas flera laddningar kan de vara lokaliserade hos olika atomer i molekylen. De positiva atomkärnorna kan då stöta ifrån varandra så att molekylen bryts isär och flera laddade fragment skapas i en process som kallas dissociation eller fragmentering. Den repulsiva kraften kallas för Coulombkraften, döpt efter Charles-Augustin de Coulomb.

I denna avhandling används flera spektroskopiska metoder för att analysera processer där molekyler fragmenterar. Detta görs genom att mäta de frigjorda elektronernas rörelseenergi och på så sätt se hur hårt bundna de var till molekylen. Med denna information kan man avgöra vilka specifika elektronbanor som kan leda till att molekylen bryter isär. I relation till detta kan vi samtidigt mäta vilka fragment som har skapats, vilket förstärker karaktäriseringen av processen.

Utveckligen av spektroskopiska metoder startade på tidigt 1900-tal och används i de flesta områden inom fysiken. Studering av joner började redan 1912 när Joseph J. Thomson byggde den första masspektrometern och upptäckte att det finns isotoper - olika varianter av samma grundämne. Det dröjde till 1955 innan W. Wiley och I. H. McLaren konstruerade den första apparaten som liknar det vi har idag, där två elektriska fält placerade efter varandra accelererar jonerna mot en detektor. Detta gav en upplösning och flexibilitet som aldrig tidigare skådats och masspektrometrarna kunde fortsättningsvis byggas mer kompakta. Spektroskopi för att mäta elektroner som frigörs med hjälp av fotoner, så kallad fotoelektronspektroskopi, kom 1967 när Kai Siegbahn presenterade sin metod ESCA (Electron Spectroscopy for Chemical Analysis), som gav honom Nobelpriset i fysik. Idag mäts elektroner på många sätt och i denna avhandling används en metod som bygger på en magnetisk flaska och som presenterades 2003 av John H. D. Eland. Metoden är utvecklad ur principer som var kända sedan tidigare där ett starkt magnetfält skapat av en permanentmagnet med en konisk topp kopplas ihop med ett svagare magnetfält längre bort. Tillsammans skapar magnetfälten en flaskliknande form som fångar upp alla elektroner oavsett vilken riktning de skickas ut från molekylen. Metoden bygger på att studera korrelation mellan samtliga elektroner som frigörs från en och samma process därför är det extra viktigt att fånga upp så många elektroner som möjligt för att får en fullständig bild av det som händer som följd av foton-absoption.

För experimenten i denna avhandling används en masspektrometer av Wiley & McLaren-typen tillsammans med en magnetisk flaskspektrometer för att helt studera fragmentationsprocesser i små molekyler (3-4 atomer) som bestrålas av ljus så att två eller fler elektroner frigörs. Detta har gjorts med molekylerna SO_2, OCS och HNCS som har släppts in i kammaren i gasform. Från studier av SO_2 har två nya mekanismer identifierades. Den första visar hur dissociation kan leda till att ett fragment tar bägge laddningarna, SO^{2+}, vilket är kanske oväntat men förekommer i större andel än tidigare trott. Det har även identifierats produktion av molekylärt syre, O_2, som produceras i mycket större grad än väntat vid dubbeljonisering, som kan initieras i rymden bland annat av solljus. Detta innebär att syrgas kan skapas utan påverkan av levande organismer eller vatten, vilket kan ha varit en bidragande faktor i syreproduktionen i jordens tidiga stadie. Det kan även antyda att syrgas kan finnas på vulkaniska exoplaneter rika på SO_2, även i miljöer fattiga på vatten.

Precis som i fallet av dubbeljonisation av SO_2 kan vi se från studier av OCS att dubbeljonisering kan leda till en omfattande omorganisation där atomerna byter plats i molekylen innan den bryter isär för att forma COS. I studier där den interstellära molekylen HNCS bestrålas av ljus detaljeras molekylens vanligaste fragmentationsprocesser vid dubbeljonisering, men även i detta fall finns det antydan på omorganisation av atomerna.

För att få djupare förståelse för fragmentationsprocesser har i denna avhandling studier utförts med en masspektrometer. En av processerna är den stegvisa processen där en molekyl bryts först i två fragment, och sedan bryter ett av dessa isär ytterligre. Tidigare har man trott att det andra steget alltid sker efter väldigt lång tid, vilket ger förutsägbar mätdata. Här visar vi fall där det andra steget sker väldigt snabbt efter det första. Detta leder till viktiga observationer i mätdatan som har tagits fram med en relativt enkel teknik och som fram till nu har varit oförklarade. En annan process kallad Coulomb-explosion har också studerats, där många laddningar skapas på kort tid i en molekyl som leder till en snabb explosion. Molekylens alla atomer får en laddning och stöter starkt ifrån varandra och hela molekylen går sönder väldigt snabbt. Vi har studerat Coulomb-explosion i molekylen CD_3I (D står för deuterium som är en isotop av väte) som bestrålats av väldigt energetiskt ljus för att skapa många laddningar. Det har visat sig att alla laddningar skapas först hos den tunga atomen jod och distribueras till de andra atomerna över tid. När tillräckligt med laddning har nått grannatomerna startar den starka Coulomb-explosionen.

Genom att kombinera våra experimentella metoder med olika teoretiska ramverk har vi lyckats identifiera flertalet nya processer hos små molekyler som bestrålas av ljus vid energier som förekommer bland annat i vår atmosfär. Fortsatt forskning med dessa metoder kan förhoppningsvis visa på fler intressanta och viktiga processer även i system ännu mer komplexa som kan förklara vad som händer i atmosfären på jorden och på andra planeter.

List of Publications

This thesis is based on the following publications:

I. **Coulomb explosion of CD_3I induced by single photon deep inner-shell ionisation**
M. Wallner, J. H. D. Eland, R. J. Squibb, J. Andersson, A. Hult Roos, R. Singh, O. Talaee, D. Koulentianos, M. Novella Piancastelli, M. Simon and R. Feifel
Scientific Reports, **10**, 1246 (2020)
My contributions: Project planning, simulations and data analysis, writing the manuscript.

II. **State selective fragmentation of doubly ionized sulphur dioxide**
M. Jarraya, **M. Wallner**, G. Nyman, S. Ben Yaghlane, M. Hochlaf, J. H. D. Eland and R. Feifel
Scientific Reports, **11**, 17137 (2021)
My contributions: Project planning, data analysis, contributed to the computations and the manuscript.

III. **Abiotic molecular oxygen production – Ionic pathway from sulphur dioxide**
M. Wallner, M. Jarraya, E. Olsson, V. Ideböhn, R. J. Squibb, S. Ben Yaghlane, G. Nyman, J. H. D. Eland, R. Feifel and M. Hochlaf
Science Advances, **8**, eabq5411 (2022)
My contributions: Project planning, data analysis, contributed to the computations and theoretical analysis, writing the manuscript.

IV. **Doubly ionized OCS bond rearrangement upon fragmentation – experiment and theory**
M. Jarraya, **M. Wallner**, S. Ben Yaghlane, E. Olsson, V. Ideböhn, R. J. Squibb, J. Palaudoux, G. Nyman, M. Mogren Al-Mogren, J. H. D. Eland, R. Feifel and M. Hochlaf
Physical Chemistry Chemical Physics, **25**, 19435-19445 (2023)
My contributions: Conduction of experiment, data analysis, contributed to the manuscript.

V. **Double ionisation and fragmentation of HNCS**
M. Wallner, E. Olsson, V. Daver Ideböhn, M. Parriani, R. J. Squibb, S. Lundberg, D. Cole, G. Nyman, J. H. D. Eland, M. Hochlaf and R. Feifel
In manuscript
My contributions: Project planning, conduction of experiment, data analysis, contributed to the computations, writing the manuscript.

VI. **Femtosecond lifetimes from island shapes in sequential three-body dissociations**
S. Price, **M. Wallner**, E. Olsson, M. Parkes, V. Daver Ideböhn, M. Parriani, R. J. Squibb, J. H. D. Eland and R. Feifel
In manuscript
My contributions: Project planning, conduction of experiments, data analysis, co-writing the manuscript.

Reprints were made with permission from the publishers.

Other publications by the author, not included in this thesis, are:

- **Relative extent of triple to single Auger decay in CO and CO_2**
  A. Hult Roos, J. H. D. Eland, J. Andersson, R. J. Squibb, **M. Wallner** and R. Feifel
  Physical Chemistry Chemical Physics, **21**, 9889 (2019)

- **Parametrization of energy sharing distributions in direct double photoionization of He**
  J. Andersson, S. Zagorodskikh, A. Hult Roos, O. Talaee, R. J. Squibb, D. Koulentianos, **M. Wallner**, V. Zhaunerchyk, R. Singh, J. H. D. Eland, J. M. Rost and R. Feifel
  Scientific Reports, **9**, 17883 (2019)

- **Double and Triple Ionisation of Isocyanic Acid**
  J. H. D. Eland, R. J. Squibb, A. Sterling, **M. Wallner**, A. Hult Roos, J. Andersson, V. Axelsson, E. Johansson, A. Teichter, S. Stranges, B. Brunetti, J. M. Dyke, F. Duarte and R. Feifel
  Scientific Reports, **10**, 2288 (2020)

- **Ultrafast dynamics of 2-thiouracil investigated by time-resolved Auger spectroscopy**
  F. Lever, D. Mayer, D. Picconi, J. Metje, S. Alisauskas, F. Calegari, S. Düsterer, C. Ehlert, R. Feifel, M. Niebuhr, B. Manschwetus, M. Kuhlmann, T. Mazza, M. S. Robinson, R. J. Squibb, A. Trabattoni, **M. Wallner**, P. Saalfrank, T. J. A. Wolf and M. Gühr
  Journal of Physics: B, **54**, 014002 (2020)

- **Core-Level Spectroscopy of 2-Thiouracil at the Sulfur L1- and L2,3-Edges Utilizing a SASE Free-Electron Laser**
  F. Lever , D. Mayer, J. Metje, S. Alisauskas, F. Calegari, S. Düsterer, R. Feifel, M. Niebuhr, B. Manschwetus, M. Kuhlmann, T. Mazza, M. Scott Robinson, R. J. Squibb, A. Trabattoni, **M. Wallner**, T. J. A. Wolf and M. Gühr
  Molecules, **26**, 6469 (2021)

- **Single photon double and triple ionization of allene**
  V. Ideböhn, A. J. Sterling, **M. Wallner**, E. Olsson, R. J. Squibb, U. Miniotaite, E. Forsmalm, M. Forsmalm, S. Stranges, J. M. Dyke, F.

Duarte, J. H. D. Eland and R. Feifel
Physical Chemistry Chemical Physics, **24**, 786-796 (2021)

- **Following excited-state chemical shifts in molecular ultrafast x-ray photoelectron spectroscopy**
  D. Mayer, F. Lever, D. Picconi, J. Metje, S. Alisauskas, F. Calegari, S. Düsterer, C. Ehlert, R. Feifel, M. Niebuhr, B. Manschwetus, M. Kuhlmann, T. Mazza, M. S. Robinson, R. J. Squibb, A. Trabattoni, **M. Wallner**, P. Saalfrank, T. J. A. Wolf and M. Gühr
  Nature Communications, **13**, 198 (2022)

- **Formation and relaxation of K^{-2} and $K^{-2}V$ double-core-hole states in n-butane**
  D. Koulentianos, V.Carravetta, R. Couto, J. Andersson, A. Hult Roos, R.J. Squibb, **M. Wallner**, J. H. D. Eland, M. Simon, H. Ågren and R. Feifel
  The Journal of Chemical Physics, **12**, 12236 (2022)

- **An experimental and theoretical characterization of the electronic structure of doubly ionised disulfur**
  E. Olsson, T. Ayari, V. Ideböhn, **M. Wallner**, R. J. Squibb, J. Andersson, A. Hult Roos, S. Stranges, J. M. Dyke, J. H. D. Eland, M. Hochlaf and R. Feifel
  Scientific Reports, **12**, 12236 (2022)

- **Symmetry breaking in core-valence double ionisation of allene**
  V. Ideböhn, R. Linguerri, L. M. Cornetta, E. Olsson, **M. Wallner**, R. J. Squibb, R. C. Couto, L. Karlsson, G. Nyman, M. Hochlaf, J. H. D. Eland, H. Ågren and R. Feifel
  Communications Chemistry, **6**, 137 (2023)

Contents

Abstract i

Svensk populärvetenskaplig sammanfattning iii

List of Papers vii

I Overview 1

1 Introduction 3
- 1.1 Atoms 5
- 1.2 Molecules 10

2 Electronic processes 13
- 2.1 Photoionisation 13
- 2.2 Multi-electron photoionisation 15
  - 2.2.1 Direct processes 16
  - 2.2.2 Auger-Meitner effect 17
  - 2.2.3 Molecular fragmentation 19

3 Experimental techniques 23
- 3.1 Light sources 23
  - 3.1.1 Pulsed helium discharge lamp 24
  - 3.1.2 Synchrotron radiation 25
  - 3.1.3 Mechanical chopper 26
- 3.2 Light, electron, and ion detectors 27
- 3.3 Magnetic bottle electron spectrometer 28

3.4 Ion mass spectrometry 30
    3.4.1 The basic TOFMS 30
    3.4.2 Improved Wiley & McLaren TOFMS 33
    3.4.3 Ion mass spectrometer 35
3.5 Augmented in-line electron and ion spectrometers 36
3.6 HNCS synthesis 37

4 Data analysis **39**
4.1 Time of flight conversion 39
4.2 Calibration of electron spectra 41
4.3 Coincidence analysis 45
    4.3.1 Electron-electron 46
    4.3.2 Multi-ion 49
    4.3.3 Sequential ion fragmentation processes 50
    4.3.4 Electron-ion 52
4.4 First-principle computations 54
    4.4.1 Geometric minima and dissociation limits 54
    4.4.2 Electronic Structure Computations 55
    4.4.3 Interpretation and comparison to experiment 55
4.5 Modelling fragmentation dynamics 57
    4.5.1 Coulomb explosion 57
    4.5.2 Deferred charge separation 58
    4.5.3 Ion trajectory calculations 59

5 Results **61**
5.1 Coulomb explosion of CD_3I upon L-shell photoionisation . . . 61
5.2 Dissociative double ionisation dynamics in molecules 65
    5.2.1 SO_2 66
    5.2.2 OCS 72
    5.2.3 HNCS 77
5.3 Femtosecond lifetimes in sequential decay 81

6 Conclusions and outlook **87**
6.1 Conclusions 87
6.2 Outlook 89

Acknowledgements **93**

Bibliography **95**

II Papers 99

I Coulomb explosion of CD_3I induced by single photon deep inner-shell ionisation I–1

II State selective fragmentation of doubly ionized sulphur dioxide II–1

III Abiotic molecular oxygen production – Ionic pathway from sulphur dioxide III–1

IV Doubly ionized OCS bond rearrangement upon fragmentation – experiment and theory IV–1

V Double ionisation and fragmentation of HNCS V–1

VI Femtosecond lifetimes from island shapes in sequential three-body dissociations VI–1

Part I

Overview

CHAPTER 1

Introduction

The nature of light, or electromagnetic radiation, has fascinated humans since the early days of science. The ancient Greeks fixated on the idea that light was connected to vision according to tactile theory, where vision was initiated by rays originating from the eye that touched or felt objects. This predecessor to the emission theory met its end in the 11th century by the works of Alhazen, who was the first to explain that vision is a result of light reflecting off objects that reach the eye.

The heavy influence of Isaac Newton and the particle corpuscular theory of light impeded the progression of the wave theory, which was postulated already in the 1600s by Descartes, Hooke and Huygens. It was not until 1865 that James Clerk Maxwell [1] showed mathematically that light was an electromagnetic wave, which was experimentally proven by Heinrich Hertz in 1887 [2]. In the early 1900s the wave theory was contradicted by the measurements of black body radiation, the spectral radiance of an object with a given temperature. Rayleigh and Jeans had formulated an expression treating the problem as a classical, continuous wave-like phenomenon which led to an infinitely large emission of energy at short wavelengths. To correct the anomaly, it took the birth of quantum mechanics and the revival of the particle theory of light. Albert Einstein postulated that light comes in discrete packets called quanta, today known as photons, built on Max Planck's hypothesis that the photon energy E is directly proportional to the frequency ν, $E = h\nu$ [3] where h is Planck's constant.

Einstein's theoretical explanation of Hertz's experimental observation of the photoelectric effect states that if radiation can only be absorbed as individual quanta then for any and all energies below the threshold there is not enough energy to remove an electron. This is the basis of the photoelectric law [4]:

$$E_k = h\nu - W \ , \tag{1.1}$$

where E_k is the kinetic energy of the emitted electron from a surface and W is the work function, which is the minimum energy necessary to remove the electron. For free atoms or molecules the work function is substituted by the electron binding energy, E_B, which is the minimum energy required to remove an electron bound to a particular discrete orbital.

$$E_k = h\nu - E_B. \tag{1.2}$$

The electron was discovered just a few years prior to Einstein's work, in 1897, by the English physicist Joseph J. Thomson [5]. Thomson went on to construct the first mass spectrometer in 1912 [6] and uncovered the first evidence of isotopes, laying the foundation for the fields of photo-electron and photo-ion spectroscopy, whereby light is used to study the processes by which ions are created in liberating electrons from their parent species. Later, the ability to generate and manipulate short electrical pulses made it possible to construct the first time-of-flight mass spectrometer (TOFMS). The early TOFMS designed in the 1940s used only a single electric acceleration field and had rather poor mass resolution. The TOFMS was substantially improved in 1955 by Wiley & McLaren [7] by using two separate acceleration fields that allows one to fine tune the mass focusing. We still use this basic principle today.

The birth of photoelectron spectroscopy took place in 1957, when Kai Siegbahn used X-ray photons to study the energy levels of atomic core electrons in solids by measuring the kinetic energy of the emitted electrons. By serendipity, the technique became ESCA (Electron Spectroscopy for Chemical Analysis) [8] and for which he was awarded the Nobel prize in physics. In 1962, D. W. Turner used ultraviolet photons from a pulsed helium discharge lamp to study the valence electrons in free molecules. The technique was combined with mass spectrometry, in 1967 by Burkhard Brehm and Ewald von Puttkammer [9] and the combined method utilizing the strength of both techniques together was named photo-electron photo-ion coincidence (PEPICO) spectroscopy.

In this thesis, interaction of matter with ultraviolet and X-radiation is used to probe *photoionisation* processes in molecules which are investigated using the combined method PEPICO. Sufficiently high-energy photons allow for the removal of several electrons, creating multiply charged molecular ions, and it is these processes which are the primary interest of this work. By losing several electrons, the net positive charges in the different constituents of a molecule repel each other, and with a strong enough repulsion the molecule will break apart, called dissociation or fragmentation.

The fragmentation of molecules can happen in different ways and result in different final ion states depending on the energy of the absorbed photon and the electrons involved in the processes. In this thesis, the fragmentation processes are investigated experimentally using electron spectroscopy and mass spectrometry, both separately and together in coincidence. To detect electrons, a magnetic bottle time of flight coincidence apparatus is used to efficiently collect all electrons emitted in all directions over a wide range of kinetic energies. For mass detection a two-field Wiley-McLaren type apparatus is used to separate ions based on their mass-to-charge ratio. Use of a pulsed light source allows for the unambiguous correlation of all emitted electrons and created ions from the same event for a detailed coincidence analysis.

This thesis aims to contribute new insights into dissociative multi-ionisation processes of gas-phase molecules. The utilisation of the spectroscopic techniques in addition to the numerical models used in this work offers a deep understanding of the fundamental mechanisms driving these processes. The implications of this thesis extend beyond the field of atomic and molecular physics to the realms of, among others, atmospherical physics, geophysics, and astrophysics, where insight into how molecules behave upon absorption of radiation is crucial. The results from papers I-VI are presented in Chapter 5, and summarised in Chapter 6. However, we remind ourselves about the foundations, continuing this chapter by discussing theoretical descriptions of atomic and molecular structure. Subsequent chapters present the necessary background of the field. Specifically, in Chapter 2 the necessary electronic processes are presented, followed by the experimental techniques in Chapter 3 and finally the framework for the data analysis in Chapter 4.

1.1 Atoms

The atom can be considered as a small particle that is basically comprised of two parts, the atomic nucleus of protons and neutrons, and the electron cloud surrounding it. The two parts are by no means equal in size, in fact, more than 99.9% of the atom's mass is in the nucleus. Conversely, the diameter of the nucleus is only about 1 fm (10^{-15} m) whereas the much larger electron cloud is on the order of Ångströms (10^{-10} m).

Different kind of atoms, called chemical elements, are distinguished by the number of protons in the nucleus, equal to the atomic number Z. Each proton carries one unit of positive electric charge which in atomic systems are neutralised by the electrons carrying one unit of negative electric charge, while the neutrons are electrically neutral. The role of the neutrons is to stabilize the nucleus by the strong nuclear force by distancing the positive protons since equal charges repel each other. The number of neutrons can vary for the same element, which defines different isotopes of that element. For example, carbon with its 6 protons has two stable isotopes: ^{12}C with 6 neutrons (98.9%) and ^{13}C with 7 neutrons (1.06%). A third commonly known isotope of carbon is the one with 8 neutrons with a total atomic mass of 14. The unstable ^{14}C has a known lifetime and a known abundance in living matter such that it can be used to date the age of objects in nature from its present concentration.

Neutral atoms can sometimes lose or gain electrons, and if this results in an unequal number of protons and electrons the the system is called an ion. An atom with fewer electrons than protons is positive and is called a cation and conversely that with excess electrons is negatively charged and called an anion. The cation is by far the most common type found in nature, primarily in the form of plasma which comprises over 99% of normal matter in the universe.

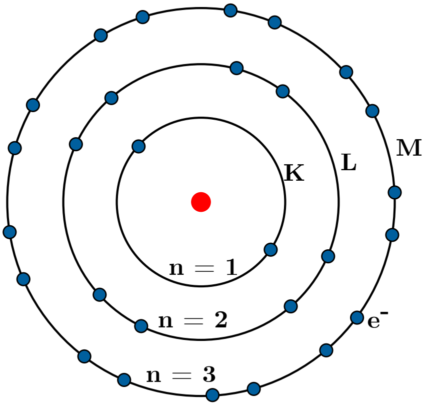

Figure 1.1: The Bohr model of an atom. The nucleus of protons and neutrons are grouped in red in the middle. The electrons are in discrete orbits around the core very similar to a solar system of planets.

At the beginning of the 20th century, the Danish physicist Niels Bohr observed spectral lines of discrete energy radiating from atoms and subsequently developed a simple atomic shell model [10], depicting the basic structure of the electrons, shown in Figure 1.1. This is known as the

Bohr model and postulates that electrons revolve around the atom at fixed distances in stable orbits without radiating any energy. The radius of the orbit is predicted by the electron's angular momenta at integer multiples, n, of the reduced Planck's constant, $\hbar = h/2\pi$. Classical angular momentum, $L = mvr$ with mass m, angular velocity v and radius r, yields $n\hbar = m_e vr$. Today, n is known as the principle quantum number, taking integer values $n = 1, 2, 3...$, with $n = 1$ giving the lowest possible radius of 0.529 Å, referred to as the Bohr radius. In the Bohr model, the shells are labelled by their number. Alternatively, the capital letters K, L, M, N for $n = 1, 2, 3, 4$, originating from the field of X-ray spectroscopy can be used, respectively.

With the development of quantum mechanics, the simple, semi-classical Bohr model was replaced by the more powerful theory of quantum mechanics leading to atomic orbitals, however, the modern theory still uses the same principle quantum number, n. In the atomic theory, after Heisenberg formulated the uncertainty principle [11], it was realised that electrons cannot possibly be restricted to a single geometric point as it would result in an infinitely large particle momentum. The electrons' position is rather viewed as a wave described by a probability distribution. Three additional quantum numbers are introduced to describe the resulting subshell structure: the azimuthal quantum number l, the magnetic quantum number m_l and the spin quantum number m_s.

l quantum number	Subshell name	Shape	
0	s	Sphere	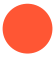
1	p	Dumbell	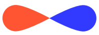
2	d	Double dumbell	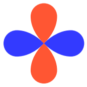
3	f	Multiple lobes	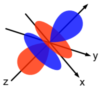

Figure 1.2: The angular momentum quantum number with its corresponding subshell name and atomic orbital shape. The colours indicate different signs of the phase of the spatial part of the wave-function.

The l quantum number denotes the orbital angular momentum of an electron and defines the shape of the orbital as shown in Figure 1.2. It may take integer values $l = 0, 1, 2, ..., n - 1$ where n is the principle quantum number. It is common to label the l quantum number using small letters such as: s, p, d, f, for $l = 0, 1, 2$ and 3, respectively. These first four letters correspond to the attributes of spectral lines associated with transitions involving electrons with such angular momenta, namely **s**harp, **p**rinciple, **d**iffuse and **f**undamental.

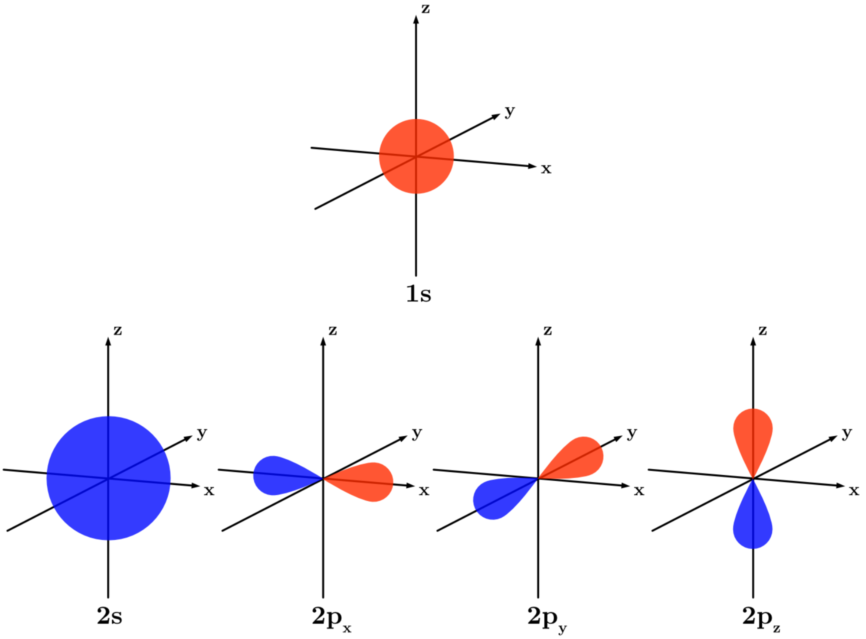

Figure 1.3: The shape of the first few atomic orbitals. 1s and 2s have the same shape with different radii. The three different 2p components have the same shape but different orientation in space. The colours indicate different signs of the phase of the spatial part of the wave-function.

The magnetic quantum number m_l denotes the component of the angular momentum along a given axis (conventionally the z-axis), where $m_l = -l, .., 0, .., l$. For the s-orbital, $l = 0$, the magnetic quantum number can only take on one value, which is immediately evident as any rotation of a sphere is invariant. For the p-orbital, $l = 1$, m_l can be $-1, 0, 1$, which is shown in Figure 1.3.

Finally, the fourth quantum number is the projection of the spin leading to the quantum number m_s, which describes the intrinsic angular momentum of the electron itself. Classically this would be described as the electron rotating around its own axis, which is not feasible as it would require the electron to rotate faster than the speed of light. Thus its description requires a relativistic formulation of quantum mechanics. As a result of that, the electron has an intrinsic half spin $m_s = +\frac{1}{2}, -\frac{1}{2}$, or more commonly referred to as “spin up” and “spin down”.

The electron is a fermion, which is a half-integer spin particle that follows Fermi-Dirac statistics and thus obeys the Pauli exclusion principle. The exclusion principle states that any many-particle wave-function must be antisymmetric with respect to exchange, meaning that the wave function must change sign when particles are interchanged. This implies that if two electrons hypothetically occupy the same quantum state, swapping them would do nothing and thus such an exchange is forbidden. In practice, this means that two electrons cannot have the same set of quantum numbers, which is a practical tool when describing the electronic structure around an atom.

In quantum mechanical language, the energy of an electron is the eigenstate solution to the Schrödinger equation $\hat{H}\,|\Psi\rangle = E\,|\Psi\rangle$, where $\hat{H}$ is the Hamiltonian describing the system, $|\Psi\rangle$ is the wave function and E is the total energy of the system. Solving the Schrödinger equation for the hydrogen atom directly leads to the first three quantum numbers, n, l and m_l, and their respective selection rules. For larger atomic systems the solutions to the Schrödinger equation are merely approximate and obtained by expanding into linear combinations of anti-symmetrized products of one-electron functions, where the spatial component is the atomic orbital. Figure 1.3 depicts an illustrative picture of the first few hydrogen-like atomic orbitals in an atom, 1s ($n = 1$, $l = 0$), 2s ($n = 2$, $l = 0$) and 2p ($n = 2$, $l = 1$, $m_l = 1, 0 - 1$). The shapes represent the spatial probability of where the electron is likely located.

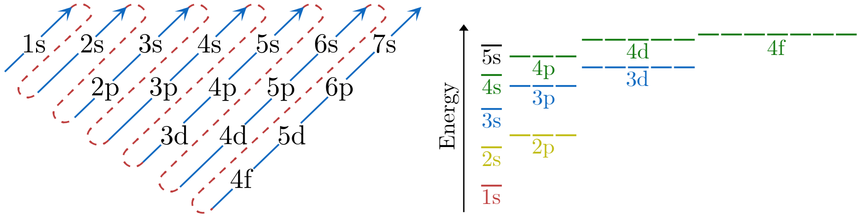

Figure 1.4: The left panel shows the Aufbau principle for constructing the electronic ground state of atoms and ions. The right panel shows the energy levels of these different atomic orbitals.

For an atom or ion with a single electron, the orbital energies within a shell are degenerate, meaning that 2s and 2p are on the same level. When more electrons are involved, the repulsive interaction between the electrons is present in addition to the attractive interaction with the positive nucleus. If an electron is located far away from the nucleus, most other electrons will be situated in between, cancelling or shielding a portion of the attractive force of the nucleus. In a given shell the energy increases with shape (l quantum number) due to the lower l orbitals penetrating further into the shield and thus feeling a stronger attraction to the nucleus. Hence, in multi-electron systems the orbital energy depends both on the shell-number and on its shape. From this, the filling of orbitals typically follows the predictable pattern of the Aufbau principle, which means “building-up”, as shown by the left panel in Figure 1.4. The principle states that in the ground state of an atom or ion, the electron fills the subshell of lowest available energy, as visualised by the right panel of Figure 1.4.

1.2 Molecules

Molecules are systems that contain two or more atoms that are bound together by their electrons. The constituent atoms may be of the same species, or different species, and vary greatly in mass and size. The smallest molecule is molecular hydrogen, H_2, and the largest may potentially be of limitless size, such as massive polymers or planet-sized diamonds.

A chemical bond is a persistent attraction between two atoms or ions. There are several types of bonds playing a role in the formation of molecules. There are weaker bonds such as dipole-dipole or hydrogen bonds and stronger bonds such as the metallic bond (e.g. a copper wire) or the ionic bond (e.g. NaCl). The strongest bond, and the most relevant in the context of this thesis, is the covalent bond whereby each atom shares electrons with

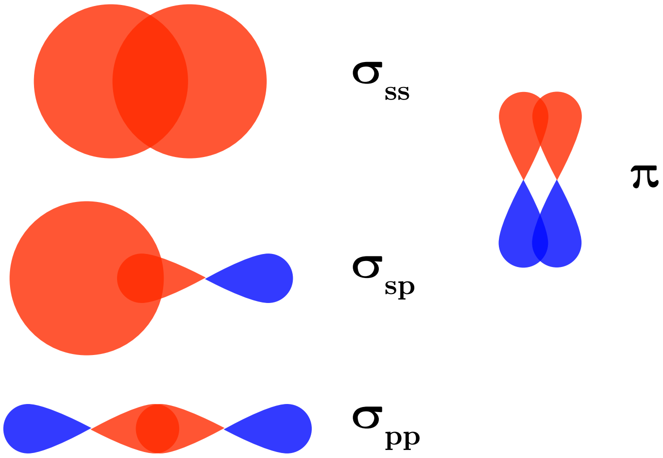

Figure 1.5: Pairs of atomic s and p orbitals that depict the overlap which creates molecular σ and π orbitals. The colours indicate different signs of the phase of the spatial part of the wave-function.

its partner. The shared electrons have a strong attraction to both atomic nuclei and simultaneously, the repulsion of the positive cores keep them from merging and the result is that the atoms oscillate around a fixed inter-atomic distance.

Generally, an atom is most stable and least reactive when its outermost electron shell is full. For the atoms typically involved in covalent bonding (primarily non-metals) this implies a full s- or p-orbital which is only achieved by the noble gases for free atoms. In order to fill its outer shell, two atoms may share electrons with each other in a favourable way such that both atoms fill their shells. This sharing is achieved by the spatial overlap of atomic orbitals, creating molecular orbitals. The molecular many-body system is complex and will here be restricted to an approximate methodology, based on s- and p-orbitals, which works surprisingly well for most diatomic molecules. Consider the orbitals in Figure 1.3, where the colour of the shapes determines the sign of the wave function, red for positive and blue for negative. Orbitals that overlap constructively (in phase) will form the bonding orbital symmetries σ and π as crudely depicted in Figure 1.5. More orbital overlap creates a stronger bond and as such the σ-bond is the strongest type of covalent bond, formed by head-on overlapping the atomic orbitals. Figure 1.5 shows three examples of σ-bonds formed by orbital overlapping: two atomic s-orbitals; one s- and one p-orbital; and two aligned p_z-orbitals. The last example in Figure 1.5 shows the formation of a molecular π-orbital by overlapping two lobes, i.e. two atomic p_x -or p_y-orbitals.

In molecular formation, the aforementioned, in-phase, overlapping atomic orbitals are in constant competition with their out-of-phase counterparts, where the overlap results in the orbitals partially or fully cancelling out. These type of orbitals are denoted with a star as σ^* and π^* and are called anti-bonding orbitals. A third case, where no overlap is present due to geometric constraints, such as p_x with p_y, are called non-bonding orbitals.

The covalent bonding and the coalescence of two atoms into a molecule is illustrated in Figure 1.6 for the case where two oxygen atoms form the oxygen molecule. The bonding orbitals decrease the total energy of the system and are thus filled first. When the bonding orbitals are full, the anti-bonding orbitals are next to be filled which counteract the bonding but are required since all valence electrons are involved in the bonding process. In terms of energy, the π and π^* essentially cancel and the number of remaining electrons responsible for the bond from each atom is 2, which means a double bond, which is expected from two atoms missing 2 electrons. More generally, the number of bonds is the same as the bonding order which is

$$\text{bond order} = \frac{1}{2}(\#\text{bonding electrons} - \#\text{anti-bonding electrons}). \tag{1.3}$$

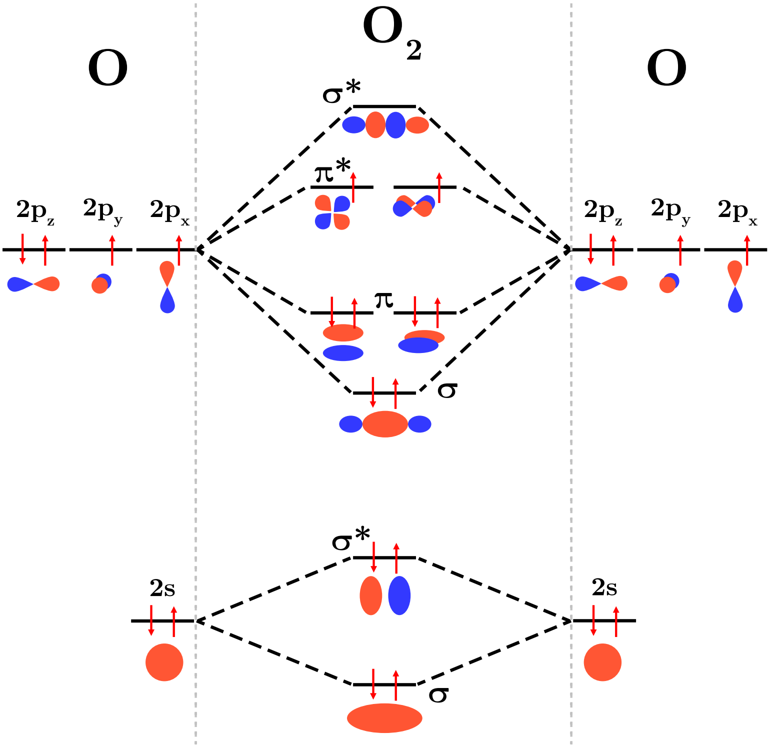

Figure 1.6: Two oxygen atoms are combined to form molecular oxygen. The total overlapping molecular orbitals are shown and the antibonding orbitals arise from opposite wave function signs cancelling.

For example, for H-C≡C-H the bond order between the two carbons is 3 and the bond order between a carbon and its neighbouring hydrogen is 1. Some molecules can have non-integer bond orders due to delocalized molecular orbitals, such as benzene with bond order of 1.5 between its carbon atoms.

For molecules with more than two atoms, the bonding structure is more involved and the simple picture described above fails in most cases. Here, for instance, hybridisation of orbitals may come into play where atomic s- and p- orbitals mix to form hybrid orbitals for pairing electrons in chemical bonds. One example is found in the carbon atom, which forms four single bonds as the valence s- and p-orbital mixes to form the hybrid sp^3 bonds in a tetrahedral arrangement around the carbon atom.

CHAPTER 2

Electronic processes

A general thermodynamic property is that all objects have a tendency to seek the minimum energy state with maximum entropy. A similar principle is true for the electrons in atoms and molecules which, unless acted on by an external force, are found in an energetic local minima, called the ground state. The Aufbau principle states that electrons fill any lower-energy orbitals before filling higher-energy ones.

This thesis presents investigations of the processes initiated in ground state molecules that are exposed to photons in the ultraviolet and X-ray spectral region, ranging from 21 eV to several thousand eV. The photon energy absorbed by the molecule may ionise the system by ejecting one or more electrons, whereby the molecule becomes charged. The created ion will naturally seek to minimise its energy which may be achieved by changing the bond length or angles between the atoms, or more drastically by breaking apart into smaller fragments.

2.1 Photoionisation

Energy supplied to an atom or a molecule, sufficiently high, can lead to the emission of an electron. The energy can be provided in the form of an impacting electron, a strong external electric field, or a photon. When an electron has been removed from the neutral atom, the number of protons in the atomic nucleus exceeds the number of bound electrons and the net electric charge is increased by one elementary charge. Atoms and molecules with net charge other than zero are called ions and the act of creation is called *ionisation*.

Photoionisation occurs when a photon of sufficiently high energy is absorbed to liberate an electron, as illustrated by the left panel of Figure 2.1. The energy required to remove the most loosely bound electron, a valence electron, is called the first ionisation energy (IE) or sometimes referred to as ionisation potential (IP). For an atomic system with total energy $\mathrm{E_A}$ and final ion with total energy $\mathrm{E_A^+}$ this is quantitatively expressed as

$$\mathrm{E_A} + h\nu = \mathrm{E_{A^+}} + \mathrm{U}_{e^-}, \tag{2.1}$$

where the excess energy is converted to the kinetic energy, U_{e^-}, of the electron liberated by the photon, called photoelectron. By shuffling the expression, the IE can be determined as the difference between the photon energy and the kinetic energy of the outgoing electron:

$$h\nu - \mathrm{U}_{e^-} = \mathrm{E_{A^+}} - \mathrm{E_A} = \mathrm{IE}. \tag{2.2}$$

The IE varies between different atomic species, where caesium is lowest at 3.9 eV and helium is highest at 24.6 eV [12].

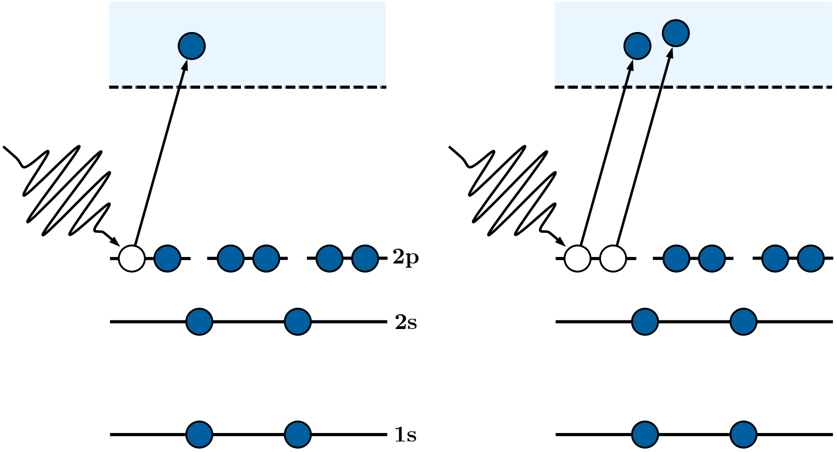

Figure 2.1: The left panel illustrates photoionisation, where one electron from the valence band is lifted to the continuum using the energy of one photon. The right panel illustrates direct double photoionisation where two electrons are directly moved to the continuum, sharing the energy from a single photon.

The first IE is a fairly simple quantity to detect experimentally and to calculate numerically, hence most stable atomic and molecular systems have been studied in numerous works carried out in this way.

2.2 Multi-electron photoionisation

The removal of more than one electron is called multi-ionisation where the simplest case is double ionisation by liberation of two electrons. A rudimentary case is where multiple photons remove one electron each, but in the present work the prime interest is multiple ionisation from single photon absorption. By irradiating an atom with a single photon of sufficient energy, because of electron correlation, two or more electrons may be directly removed, where the excess energy is shared between the ejected electrons as kinetic energy, as depicted in the right panel of Figure 2.1. Quantitatively the direct double ionisation process for an atomic system, with energy $\mathrm{E_A}$ to the doubly charged form at energy $\mathrm{E_{A^{++}}}$, is expressed as:

$$\mathrm{E_A} + h\nu = \mathrm{E_{A^{++}}} + \mathrm{U}_{e_1^-} + \mathrm{U}_{e_2^-} \tag{2.3}$$

leading to the expression for the double ionisation energy (DIE),

$$\mathrm{DIE} = h\nu - \mathrm{U_{tot}} = h\nu - (\mathrm{U}_{e_1^-} + \mathrm{U}_{e_2^-})\,, \tag{2.4}$$

where $\mathrm{U}_{e_1^-}$ and $\mathrm{U}_{e_2^-}$ are the kinetic energy of electron 1 and 2, respectively.

Intuition might suggest that the energy required to remove two electrons is twice the energy to remove one electron. In reality, however, the screening effect of the electrons changes the effective nuclear charge as electrons are removed due to the decreased influence of the electron-electron repulsions. The most loosely bound electron in the ion is more tightly bound than that of the neutral atom, and each electron removed increases the energy required to remove the next. The energy required for double ionisation of an atom has been shown experimentally to quite closely follow an empirical rule-of-thumb [13]

$$\mathrm{DIE} \approx 2.8 \cdot \mathrm{IE}\,. \tag{2.5}$$

This formula has been very useful when preparing new investigations of double ionisation in hitherto unstudied species.

However, for many molecules this first rule-of-thumb is not so accurate, and for very large molecules the DIE is expected to approach the limit of 2·IE. This is partly due to the increase in the physical distance of the electron vacancies that are created, which in larger systems are several or 10s of Ångströms apart. Another contributor to such a low DIE can be the increased number of electrons available which diminishes the relative change in the screening effect from the removal of one electron. Thus, a refined rule-of-thumb [14] was derived by Molloy and Eland, where the Coulomb repulsion of the electron vacancies is taken into account. The empirical formula for DIE in molecules is given by

$$\mathrm{DIE} \approx 2.2 \cdot \mathrm{IE} + \frac{11.5\ \mathrm{eV\AA}}{r_{12}}\,, \tag{2.6}$$

where r_{12} is the distance between the initial localisation of electron 1 and 2.

2.2.1 Direct processes

The process of direct single photon double ionisation is categorised in two dominant mechanisms called *knock-out* and *shake-off* [15]. Here, the incoming photon is absorbed by one electron and in the process of leaving the bound state, part of the energy is redistributed to another electron. The two electrons leave the atom or molecule with shared excess energy in the form of kinetic energy.

The knock-out mechanism is a semi-classical process and describes the correlation dynamics of electrons. The primary electron absorbs the photon, and in a collision-like interaction transfers some of its energy to a second electron on its way out, resulting in the second electron being “knocked out”. For higher energies, the primary electron is ejected so quickly that there is less time to transfer energy to a second electron and the probability of this process diminishes [15].

In contrast, the shake-off mechanism is a purely quantum mechanical process where the primary electron is modelled to leave instantaneously. The sudden removal causes a change in the atomic field which the system must relax into which can be viewed classically as the system shaking. There is a probability that the second electron relaxes to an unbound state, i.e. it is “shaken off” [15, 16]. Moreover, the shake-off mechanism depends entirely on the initial state correlations where the primary electron takes all the angular momentum from the photon and the second electron’s angular momentum is unchanged. The knock-out mechanism has no such restrictions as it takes all the post absorption interaction into account.

The distribution of the energy between the electrons depends greatly on the quantity of available excess energy left upon double ionisation. For low excess energies (< 10 eV) the sharing is arbitrary with a uniform energy sharing distribution. For higher energies the tendency leans heavily to one electron taking almost all the excess energy with the other left with very little. [17]

2.2.2 Auger-Meitner effect

The Auger-Meitner effect is a decay process discovered independently in the 1920s by both Pierre Auger [18] and Lise Meitner [19]. It is the process where electrons of characteristic energy are emitted from atoms (or molecules) in response to the relaxation of an excited state. The simplest picture of the Auger-Meitner effect assumes a two-step process involving three electrons where two electrons leave the atom. There are also resonant cases where an electron is excited to a higher orbital within the system but these are generally less common as in this case the photon energy must match the transition energy for the resonant excitation. Also, the resonant case will lead to a singly charged state akin to auto-ionisation, whereas the Auger-Meitner process will put two electrons in the continuum which implies the formation of a dicationic state. When an Auger-Meitner process occurs in more than two steps it is referred to as an Auger-Meitner cascade, and these will lead to higher charge states.

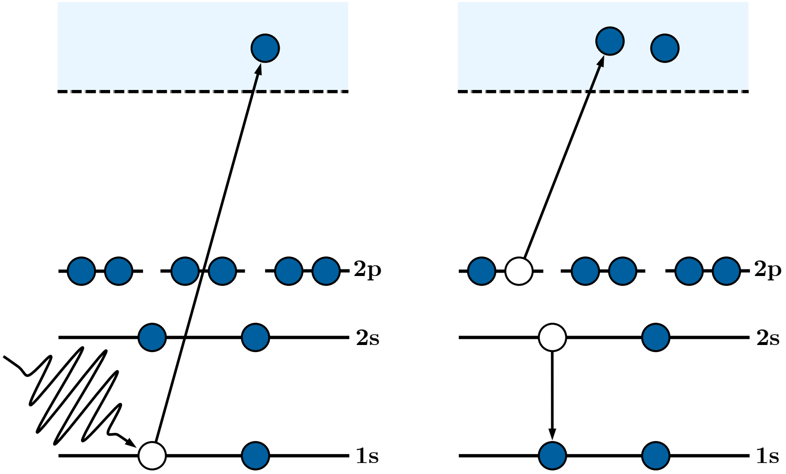

Figure 2.2: The left panel depicts the initial core hole creation where one electron is photoexcited to the continuum. The right panel shows the relaxation of the excited ion state by filling the vacancy with an electron. The remaining energy is transferred to a valence electron (the Auger-Meitner electron) which is ejected.

A high energy photon can liberate an inner-shell electron (the photoelectron) leading to an unstable vacancy as shown in the left panel of Figure 2.2. The excited state relaxes via a more loosely bound electron filling the vacancy, where excess energy is liberated. This liberated energy may be carried away radiatively in the form of a photon, known as florescence. Alternatively, the energy can also be transferred to another bound electron which is liberated from the system with characteristic kinetic energy, referred to as *Auger-Meitner decay*, as shown in the right panel of Figure 2.2. The ejected electron is called an *Auger-Meitner electron* and will have a fixed energy dependent on the excess energy liberated by the energy transition.

The transition rate, W, of the Auger-Meitner decay is found by direct application of the Fermi golden rule, to first order perturbation theory [20]

$$W = \frac{2\pi}{\hbar} \left\langle \psi_f(E) \right| \frac{1}{r_{if}} \left| \psi_i \right\rangle^2 \rho_f(E), \tag{2.7}$$

where ψ_i is the initial state, ψ_f is the final state and $\rho_f(E)$ is the density of free electron states in the continuum with kinetic energy E and r_{if} is the matrix element of the static Coulomb interaction between the two electrons [21]. This means that the transition probability is related to the radii difference of the two electrons involved and thus it is more likely that deep lying vacancies will traverse up stepwise to the valence band rather than taking one long step.

The energy given to the emitted electron is equal to the energy released when shifting the electron vacancy. The liberated energy is essentially the energy difference between the binding energy of the two electron orbitals. In some larger atoms, the energy difference between two subshells with the same quantum number n is enough to eject an electron from a higher subshell. Such a transition is called a *Coster-Kronig* transition [22] and is usually associated with high transition rates. Furthermore, if the emitted electron also belongs to the same shell the decay is referred to as a *super Coster-Kronig* transition. The strong transition rates of the Coster-Kronig decays relate to the radial wave function, where the initial and final state can be very similar.

The lifetime of the core hole is inversely proportional to the sum of the rates from all allowed transitions, and is typically in the few femtosecond regime. The very fast Coster-Kronig transitions can have lifetimes, τ, several orders of magnitudes lower, resulting in a broadening of kinetic energies, ΔE, due to the uncertainty principle

$$\tau \Delta E \geq \frac{\hbar}{2}\,. \tag{2.8}$$

If a vacancy remains in a deep lying shell following Auger-Meitner decay, additional relaxation can occur, emitting more electrons in an Auger-Meitner cascade. The cascade can continue until all the vacancies are in the outermost shells, or if energetics prohibiting electron ejection.

2.2.3 Molecular fragmentation

Covalent molecular bonds are formed by the sharing of electron pairs forming molecular orbitals. By liberating these electrons, these bonds weaken and the molecule can break apart into smaller fragments.

Molecules are often modelled classically using harmonic oscillators. For a diatomic molecule, the atoms are viewed as point masses where the bond between them works like a spring and the oscillation corresponds to molecular vibration. This harmonic oscillating motion serves as a first approximation in quantum mechanics. The quantum harmonic oscillator vibrates back and forth in fixed vibrational modes of specific amplitudes. This model works rather well for the description of the lower vibrational levels, however, the model's primary issue is that since it is a symmetric potential, the atoms are permanently bound and can never dissociate.

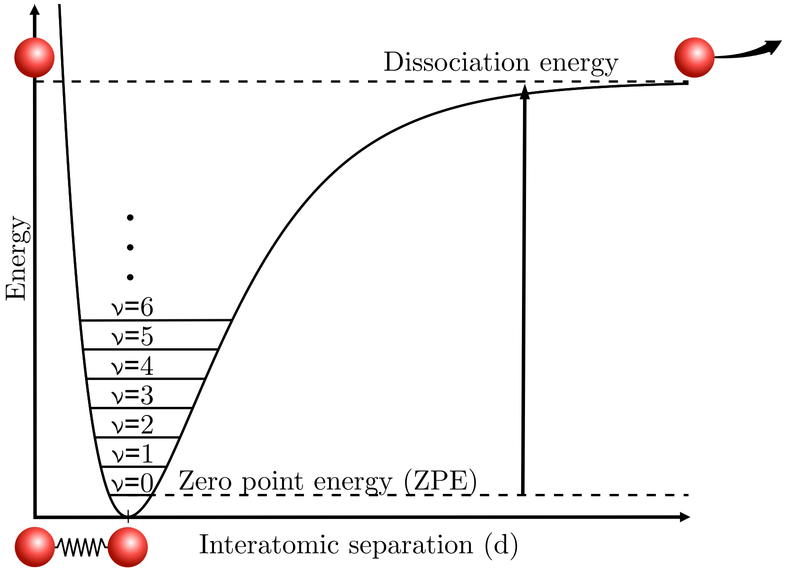

Figure 2.3: The Morse potential illustrating the interatomic separation of a diatomic molecule and different vibrational modes ν.

A better approximation for the molecules' vibrational structure is a Morse potential depicted in Figure 2.3 which can successfully predict bond breaking. The first vibrational level is denoted $\nu = 0$, called the zero point energy (ZPE), and is the lowest vibrational state the molecular system can occupy. Here, the atoms vibrate back and forth within the potential energy barrier. Higher vibrational levels can be found by exciting the molecule with more internal energy. By raising the energy of the system to higher than the

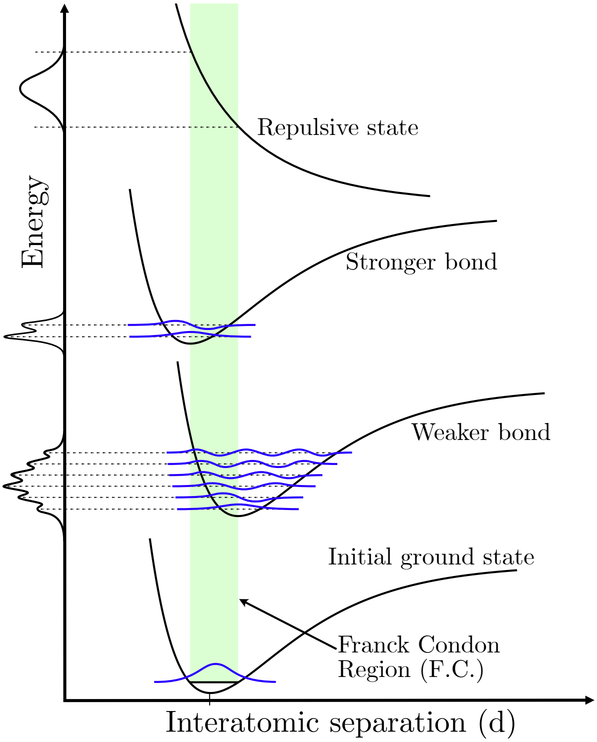

Figure 2.4: Illustration of the vertical transition within the Franck-Condon region, reaching excited or ionised electronic states with weaker or stronger bonding.

dissociation energy, the atoms will no longer be confined by the potential well and the atoms will be free to become infinitely separated, i.e. the bond is broken.

A diatomic molecule with a vibrational wavefunction at a mean bond distance yields a spatial probability distribution shown by the blue curve of the ground state in Figure 2.4. Within the validity of the Born-Oppenheimer approximation, supplying energy to the system may result in electronic transitions, on the femtosecond timescale, that are much faster than any nuclear motion. Thus, according to the Franck-Condon principle, the nuclear wavefunction traverses vertically, hence the name *vertical transition*. This is illustrated by the green box in Figure 2.4 called the Franck-Condon region and represents the spatial region where vertical transitions occur. Transitions lead to different states depending on the transition probability, which is proportional to the overlap of the initial and final state wavefunctions. If the bond distance is unchanged, transitions from the vibrational ground state to another states' vibrational ground state, called *adiabatic transitions*, have the largest overlap. In contrast, the overlap with higher vibrational states, whose form is more sine-like, mostly cancel out. However, if the final state is more strongly or weakly bound, as illustrated by Figure 2.4, the edges of the higher vibrational wave function may not fully cancel and higher vibrational levels can be populated. As shown in Figure 2.4, more states will be accessible for a weaker bond due to the asymmetrical form of the Morse-potential, which is observable experimentally. How the molecular bond gets stronger or weaker is realised by the bonding character of the molecular orbitals involved in the transition. Simple excitation from a bonding orbital to a non-bonding or anti-bonding orbital results in a weaker bond. Conversely, a transition from an anti-bonding orbital to a non-bonding or bonding orbital results in a stronger bond. Finally, a transition from the electronic ground state to a repulsive state shown in Figure 2.4 gives a broad feature, essentially projecting the initial state's wavefunction probability on-to the energy axis.

CHAPTER 3

Experimental techniques

The experimental techniques relevant to this thesis focus on the detection of charged particles (electrons and ions) produced by absorption of a single photon in the ultraviolet, soft and hard X-ray regions. The experimental set-up consists of two parts, one for the detection of ions and the other for the detection of electrons. The ion spectrometer can simultaneously detect multiple particles in coincidence and distinguish their individual mass/charge ratio by recording the ion flight times under Wiley-McLaren conditions [7]. The electron spectrometer collects all electrons emitted in 4π solid angle, whose flight times are measured and converted into kinetic energy. With a well-defined photon energy, the processes leading to multiply ionised final states can be described and the multi-ionisation energies can be determined. Electrons and ions may be collected simultaneously in a co-linear configuration for determination of final charge state selective ionisation energies.

3.1 Light sources

Two separate types of light source were used in the experiments described in this thesis: vacuum ultraviolet light produced by a pulsed helium discharge lamp and synchrotron radiation produced by electron storage ring facilities operated in single bunch mode. The emission lines of helium, in particular He Iα and He IIα, produced by the discharge lamp are well suited for studies of valence single and double ionisation in most atomic and molecular systems.

Inner shell ionisation experiments often require higher energy than the helium lamp can produce, which is where the synchrotron radiation facility is used.

These experiments require specific properties of the light. In order to unambiguously distinguish electrons from an individual ionisation event, the light must come in pulses that are both short (ideally < 1 ns) and sufficiently separated in time as to allow all the electrons and ions to reach the detectors before the next ionisation event occurs. The inter-pulse spacing required can be estimated by the slowest particle travelling a certain distance, which for electrons is at near-zero kinetic energy. For ions it is determined by the heaviest expected particle which for these studies is typically the parent molecule for a given experiment. The photon energy must be known, stable, and sufficiently high as to liberate one or more electrons. In this thesis energies in the range 21 eV - 5300 eV, i.e. the vacuum ultraviolet (VUV), extreme ultraviolet (XUV), soft and hard X-ray regimes are utilised.

3.1.1 Pulsed helium discharge lamp

In our home laboratory at the University of Gothenburg the light is produced using a pulsed helium discharge lamp, schematically illustrated in Figure 3.1 [23, 24]. Two electrodes are separated by a ceramic insulator which has a small capillary ($\sim$ 1 mm) drilled through it. Helium gas is allowed to flow into the capillary via a needle valve. The cathode is powered by a high voltage supply typically at 7-8 kV which is controlled by a fast high voltage solid state MOSFET switch [25]. The high potential on the cathode, generating a strong electric field across the capillary, will result in an electrical breakdown of the gas, which will excite and ionise the helium atoms leading to

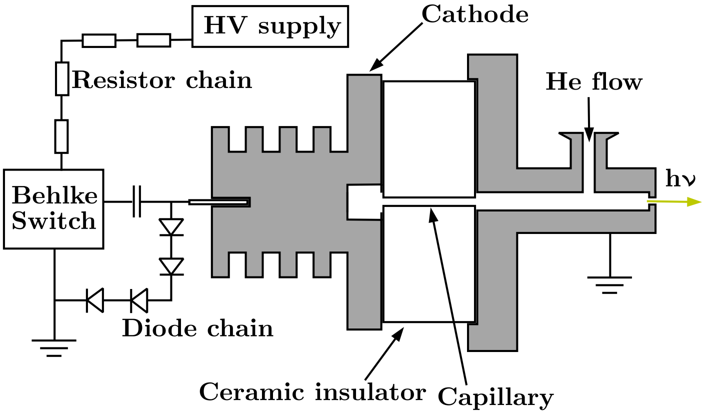

Figure 3.1: Schematic of the pulsed helium discharge lamp.

Table 3.1: The main strong helium lines [26] primarily used with the present apparatus.

Helium Line	Wavelength (Å)	Energy (eV)
He Iα	584.33436	21.218
He IIα	303.7804	40.814
He IIβ	256.32	48.37
He IIγ	243.03	51.02

a subsequent discharge. The electrons in the helium atoms relax by emission of photons at discrete emission lines, with the presently important lines listed in Table 3.1. These discharges occur at a repetition rate of about 4 kHz, limited by the switch, and yield light pulses with 10 ns pulse durations. These photons are emitted in all directions where some will go toward the spectrometer through a narrow capillary, reflected via a diffraction grating monochromator. The toroidal grating used will both focus and reflect the light with an outgoing angle depending on the wavelength. The grating is rotatable which changes the incident angle as to allow only one chosen photon energy to enter the narrow spectrometer entrance. The timing of the light pulse is monitored by either an antenna placed close to the cathode which will electrically pick up the discharge, or by a photomultiplier placed after the light/matter interaction zone. This is used in the acquisition system to determine the start of the electrons and ions flight times.

3.1.2 Synchrotron radiation

Liberating electrons bound to inner shells typically requires photons with more energy than the helium lamp can produce, i.e. in the soft and hard X-ray regime. X-ray light spans from 100 eV to several thousand eV, which can be offered by synchrotron radiation facilities. A synchrotron is a cyclic particle accelerator in which the charged particles travel around a closed loop of fixed length. Storage ring light sources take advantage of the phenomenon where electromagnetic radiation is emitted when the relativistic, charged particle is subject to acceleration perpendicular to its velocity.

A modern synchrotron radiation facility comprises a small synchrotron which in turn populates a much larger electron storage ring with a polygonal structure, consisting of many straight sections. Strong bending magnets are used at the intersections that transfer the electrons from one straight section to the next, emitting a broad spectrum of radiation. The straight sections are equipped with two very similar insertion devices called wigglers and undulators which both consist of a series of alternating, periodically spaced magnets. The electrons will oscillate in the axis tangential to their propagation when going through these devices, emitting photons in a forward cone. The primary difference between the two class of insertion devices is the magnetic field strength. The undulator has a much weaker magnetic field yielding fewer photons, but with the advantage that they are emitted in a smaller cone. Additionally, the undulator has a higher spectral precision with a narrower frequency distribution. The photons produced from the insertion device will be routed and focused by several mirrors and optical components and, most importantly, a wavelength selecting monochromator. The insertion device and the monochromator are tuned to optimise and select a specific wavelength, yielding a high flux beam with very precise photon energy. Finally, the light is focused by a set of mirrors to a very small spot, a few micrometers to some tens of micrometers.

The work in this thesis has utilised two undulator beamlines at two facilities: LUCIA [27] at SOLEIL in Paris and UE52-SGM [28] at BESSY II in Berlin. LUCIA is capable of producing X-rays in the range of 0.8 - 8 keV at the storage ring SOLEIL which has a circumference of 354 m with an electron orbit time of 1081 ns. UE52-SGM can produce XUV/X-rays in the range of 90 - 1500 eV at the storage ring BESSY II with a circumference of 240 m with an orbit time of 800.5 ns.

3.1.3 Mechanical chopper

In photoionisation coincidence time-of-flight experiments, it is highly desirable for the slowest electrons and/or ions from one event to reach its detector before the next pulse arrives, to avoid the simultaneous detection of particles from overlapping events. Electron flight times are typically < 5000 ns whereas ion flight times may easily be several 10s of μs, depending on the acceleration field strength and the mass of the parent molecule. In synchrotron storage rings the orbiting time of the electron bunch is only ~ 1 μs, which is much too fast for the present experiments even if only a single light pulse is produced per orbit. Increasing the light pulse interval is achieved by physically blocking a majority of the pulses with a mechanical chopper, ideally synchronised to the radio frequency signal of the storage ring. Our chopper consist of two concentric, rotating discs with 120 equidistant slits on their outer diameter with an additional set of 15 slits with a larger angular spacing located further in on the discs [29]. The two discs are coaxially aligned and can be manually shifted in angle relative to each other to make the slit width smaller, which reduces the opening time and the amount of light that pass through. At BESSY II, the light passes through at a rate of approximately 80 kHz (12.5 μs) and 10 kHz (100 μs) for 120 slits and 15 slits, respectively.

3.2 Light, electron, and ion detectors

The light pulses inducing ionisation pass through the light-matter interaction zone whereafter they are detected using a photomultiplier tube (PMT). The PMT, illustrated in Figure 3.2, where the incident light hits a photocathode surface made of Cu covered by a layer of BeO (or CsI), increasing the photosensitivity in the UV and X-ray regimes, respectively. The secondary electrons are accelerated down a Cu dynode chain coupled to a potential divider resistor chain. The avalanching cascade of electrons is multiplied by an order of 4×10^7 [30] and hit the anode with a signal strong enough to read directly on an ampere meter or an oscilloscope.

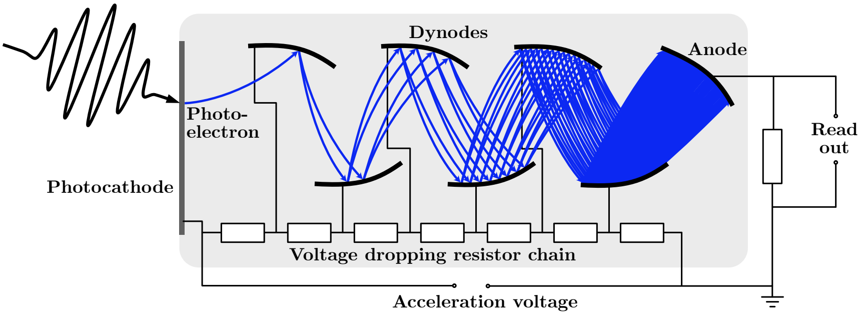

Figure 3.2: Photomultiplier tube. The signal of the incoming photon is multiplied to be readable.

For the detection of single particles, such as electrons and ions, micro-channel plate (MCP) detectors are placed at the end of the flight tubes. An MCP consists of a thin lead glass plate densely perforated by a periodic structure of small channels, each with a diameter of about 10 μm. The channels are coated with a semi-conducting material favouring the release of secondary electrons and additionally the channels lie at an incident angle of about 8° to increase the likelihood of the incoming particle hitting the inner wall of a channel, releasing such secondary electrons. The secondary electrons continue to cascade down the microchannel, creating an avalanche of electrons. To increase the gain of the detector, two or more MCPs are stacked where each consecutive plate is rotated 180 degrees relative to the other. Figure 3.3 illustrates a so called Chevron stack which comprises two plates, and for the experiments in this thesis a so called Z-stack has been used, with three stacked plates. In the MCP the particles must enter a channel and hit the inner surface in order to produce a detectable avalanche signal, and thus the detection efficiency is largely determined by the incoming particle energy and the open area ratio which in the present case is about 50-65%.

Each channel has a dead time where it must recharge before subsequent detection may occur, however, with the low number of electrons and large number of channels present this effect is negligible for the conditions under which our experiments are performed.

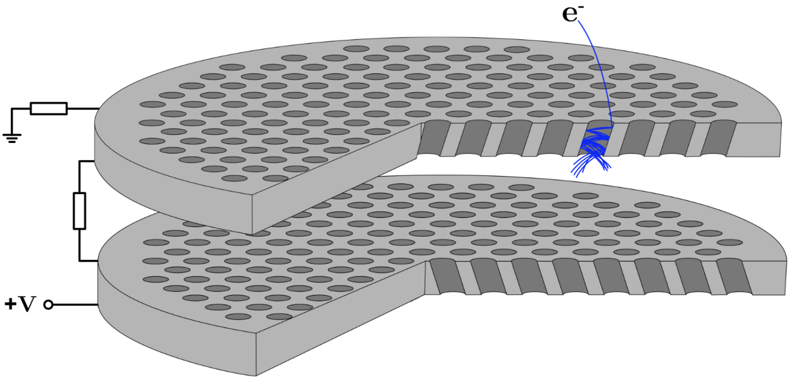

Figure 3.3: Chevron stack of micro-channel plates. An incoming particle enters a channel and is multiplied.

3.3 Magnetic bottle electron spectrometer

The basic underlying principle behind an electron time of flight spectrometer is that an electron's kinetic energy can be determined by measuring the time it takes to fly a known distance. A magnetic bottle electron spectrometer (MBES), originally developed by Kruit and Read [31], has been used in this thesis to obtain highly resolved coincidence double ionisation spectra of molecules ionised by single photons, a concept introduced first by John H. D. Eland at Oxford University [24]. The MBES can collect all electrons emitted in a single ionisation event simultaneously and continuously

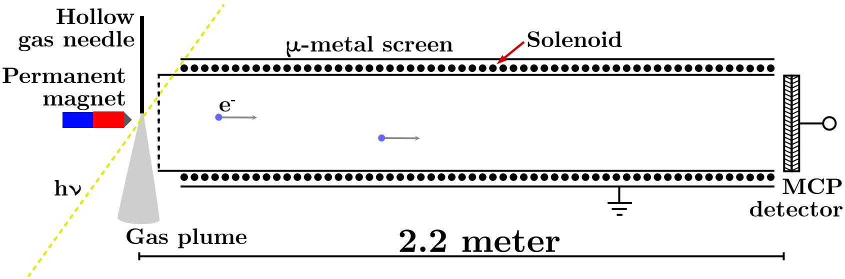

Figure 3.4: Schematic of one of our magnetic bottle time of flight spectrometers.

over a wide range of electron kinetic energies, from near zero eV to several hundred eV. A schematic figure of the apparatus is shown in Figure 3.4. Here, an effusive jet of target gas is let into the vacuum chamber using a hollow needle where it is intersected by wavelength selected, pulsed photons in the VUV or X-ray region. The needle is placed on an *xyz* motion stage which allows careful adjustments of the position to be made without opening the vacuum chamber.

The electrons released upon ionisation are initially emitted in all directions and fully collected in a 4π solid angle by a strong, divergent magnetic field which is coupled to a weaker solenoid field. The strong field is generated by a permanent neodymium-iron-boron magnet with an attached conical soft iron pole piece with a resulting magnetic field strength of ~ 1 T at the light-matter intersection point. The solenoid is formed by insulated copper wire wound around the entire electron flight tube, which is covered with a μ-metal shield to prevent interference from stray fields. This arrangement generates magnetic field lines that resemble the shape of a bottle neck, shown in Figure 3.5, stretching all the way to the detector.

An electron moving in the magnetic bottle experiences acceleration from the electric and magnetic fields according to the Lorentz force

$$\vec{F} = q(\vec{E} + \vec{v} \times \vec{B}) \,, \tag{3.1}$$

where q is the electron charge, $\vec{v}$ its velocity, $\vec{B}$ the magnetic field and $\vec{E}$ any electric field, wanted or not. The magnetic part of the Lorentz force causes the electron to spiral around the magnetic field lines resulting in a helical motion. In going from the strong field to the weak field region the Lorentz

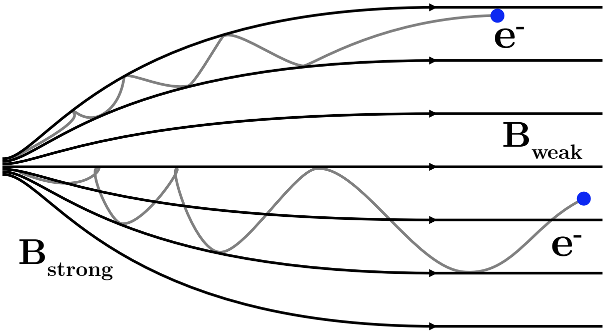

Figure 3.5: Illustration of the field lines of the magnetic bottle going from a strong magnetic field B_{strong} to the uniform weaker field of the solenoid B_{weak}, based on the figure in Ref. [31]. The electrons' helical motion is gradually parallelised regardless of initial velocity.

force acting on the electron always has a component along the guiding lines in 3.5. The small incremental changes in the direction of the field lines allow the longitudinal component to increase, and since the total velocity is unchanged the transverse component is consequently reduced, leading to parallelisation of the electron trajectories [31]. This early stage of the electrons' flight path during parallelisation is a limiting factor to the energy resolution of the apparatus, together with the length of the drift tube. The nominal energy resolution is $E/\Delta E = 50$ for our 2.2 m instrument.

The flight time is experimentally determined as the time difference between a reference start (that is concomitant with the ionisation event) and the detection of the electron. In the Gothenburg lab the start pulse is produced by an antenna placed inside the helium lamp, which picks up the electric impulse of the discharge. At synchrotron facilities an "AND"-logic gate generates a start on the coincident detection of a light pulse from the PMT tube with the precise timing of the ring frequency provided by the beamline. The PMT is used to determine which light pulses pass through the mechanical chopper, since the ring cycle signal has a much higher repetition rate than what is actually used by our set-up. The ring frequency, however, has much higher timing precision than the PMT, which is critical to achieve the best possible resolution.

3.4 Ion mass spectrometry

An early time of flight mass spectrometer called the "Velocitron" [32] was built in 1948, where a magnetic field is used to separate ions of different mass, based on the principles introduced by William E. Stephens [33] two years prior. Due to its very poor mass resolution, further development of this basic concept led to the improved design in 1953 by Stephens et. al [34]. The new apparatus used a non-magnetic, electrostatic principle where the accelerating electric fields are turned off before the ions have left the source region, giving them equal momenta rather than energy. The most significant breakthrough was proposed by W. Wiley and I. H. McLaren in 1955 [7], building on a two-field configuration, whose fundamental design is very similar to the apparatuses we use today.

3.4.1 The basic TOFMS

Ion spectrometers come in a wide range of shapes and sizes. A typical, and the most basic, set-up of a time of flight mass spectrometer (TOFMS) consists of an ionisation source region, an acceleration field, a field free drift region and a detector, as schematically illustrated in Figure 3.6. Here, gas is let into a chamber which is ionized by photon absorption or electron impact. The electrostatic field applied across the source region accelerates the ions into the drift tube toward the detector, where their flight times are registered upon arrival.

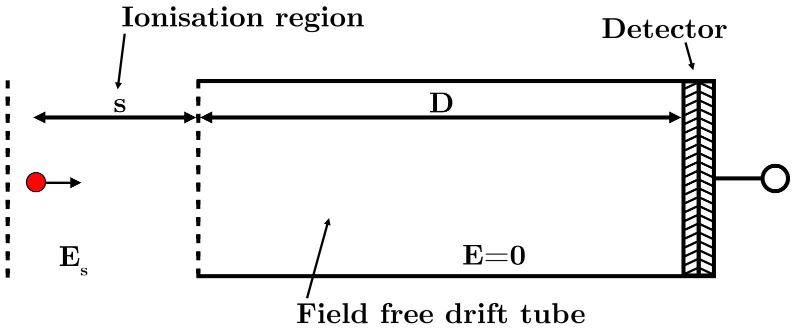

Figure 3.6: Simple illustration of the one-field time of flight mass spectrometer.

The total flight time of the ion is divided into the partial flight times in the ionisation region, T_s, and the time in the drift tube, T_D

$$T = T_s + T_D\,. \tag{3.2}$$

In the drift tube the ion has constant velocity equal to the final velocity v_f from the acceleration. Hence, the time spent in the drift tube is simply extracted from the known drift tube distance D using

$$T_D = D/v_f\,. \tag{3.3}$$

The velocity gained in the acceleration field depends on the strength of the acceleration and the time in the field

$$v = aT_s \tag{3.4}$$

where the acceleration is derived simply from Newton's second law and the Lorentz force

$$F = ma = qE\,. \tag{3.5}$$

An ion in the acceleration region may have some additional initial momentum due to kinetic energy release from fragmentation processes. Only the velocity component in the axis of the drift tube affects the flight time and this velocity difference is assumed to be $\pm v_0$, where both forward and backward initial directions are allowed. The final velocity of the forward flying ion with initial velocity $+v_0$ is given as

$$v_f = v_0 + aT_s\,. \tag{3.6}$$

The backwards flying ion with initial velocity $-v_0$ will decelerate to a complete stop whereby it regains all momentum once it reaches its original position with velocity $+v_0$. The extra turn around time is determined by setting the final velocity in Equation 3.6 to $+v_0$ with an initial velocity $-v_0$ and a turn around time $T_\pm$ as

$$v_0 = -v_0 + aT_\pm \tag{3.7}$$

such that

$$T_\pm = 2v_0/a\,. \tag{3.8}$$

Hence, the total flight time spent in the acceleration region is:

$$\text{Forward: } T_s = \frac{v_f - v_0}{a} \tag{3.9}$$

$$\text{Backward: } T_s = \frac{v_f - v_0}{a} + T_\pm = \frac{v_f + v_0}{a} \tag{3.10}$$

which can be combined to

$$T_s = \frac{1}{a}(v_f \pm v_0)\,. \tag{3.11}$$

From Equation 3.5 and the kinetic energy relation $U = \frac{1}{2}mv^2$, the times spent in both regions are

$$T_s = \frac{\sqrt{2m}}{qE_s}(\sqrt{U_k} \pm \sqrt{U_0}) \tag{3.12}$$

$$T_D = D\sqrt{\frac{m}{2U_k}}\,, \tag{3.13}$$

where the final kinetic energy U_k is dependent on the ion charge, the field strength and the distance the ion travels under the influence of the electric field

$$U_k = U_0 + qsE_s. \tag{3.14}$$

To this point, it was assumed that the ions originate only at a single spot. In realistic conditions the initial positions have a spatial distribution due to a finite size of the light beam and the wide plume from the effusive jet of the target gas, leading to a spread in the flight times. With a start position $\pm\delta s$ from the nominal initial position, the total energy obtained is

$$U_k = U_0 + q(s \pm \delta s)E_s\,. \tag{3.15}$$

Hence, an ion initially created further from the detector acquires more energy, and in turn velocity, and conversely closer ions acquire less energy. The furthest ions will eventually catch up and overtake the closer ions and arrive at a shorter flight time. To minimize the width of the detected peak, the detector should be placed at the point where the faster ions catch up to the slowest, determined by

$$\frac{dT}{ds} = 0\,. \tag{3.16}$$

The above equation is satisfied for $D = 2s$, implying that this so-called spatial focusing condition only depends on the size of the two regions, where the drift tube must be twice as long as the acceleration region. This is a major limitation that makes the resolution of the single-field apparatus very poor.

3.4.2 Improved Wiley & McLaren TOFMS

In 1955 Wiley & McLaren [7] improved the mass resolution of the time of flight mass spectrometer significantly by introducing a second acceleration field. The new apparatus comprised two fields, as shown in Figure 3.7: a relatively weak extraction field in the ionisation region and a much stronger acceleration field. The new adjustable parameters allow for a far greater degree of flexibility in the spectrometer dimensions for which spatial focusing conditions can be achieved.

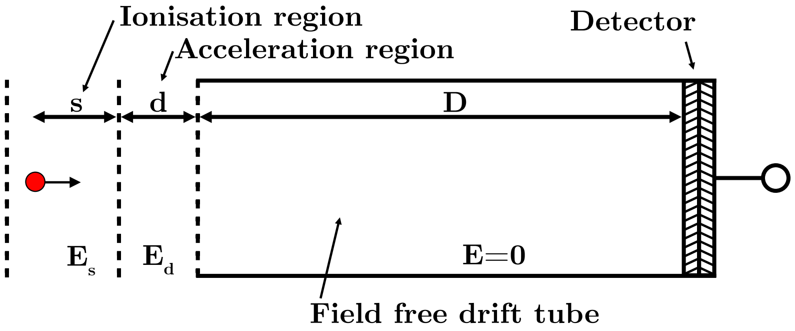

Figure 3.7: Simple illustration of the two-field spectrometer.

The total ion flight time of the two-field apparatus is divided into the partial flight times of the regions s, d and D

$$T = T_s + T_d + T_D\,, \tag{3.17}$$

whose derivation is similar to the single field apparatus with an additional intermediate velocity and kinetic energy. The partial flight times are

$$T_s = \frac{\sqrt{2m}}{qE_s}(\sqrt{U_{IM}} \pm \sqrt{U_0}) \tag{3.18}$$

$$T_d = \frac{\sqrt{2m}}{qE_d}(\sqrt{U_k} - \sqrt{U_{IM}}) \tag{3.19}$$

$$T_D = D\sqrt{\frac{m}{2U_k}}\,, \tag{3.20}$$

where U_{IM} is the intermediate kinetic energy at the point between the two field regions. The final energy is dependent on the particles charge, the field strengths and the distance travelled under acceleration

$$U_k = U_{IM} + qdE_d = U_0 + qsE_s + qdE_d\,. \tag{3.21}$$

The ± in Equation 3.18 is to account for ions with initial energy, as previously discussed. In reality, the ions will almost certainly have a distribution of initial velocities and direction, and the ± term specifies the two extremes of the ions' flight time. An ion initially flying perpendicular to the flight tube axis does not add any momentum on the flight axis and will have the same flight time as an ion (of the same mass/charge) of zero initial momentum. In experiments the aperture and diameter of the flight tube is typically limited and thus a sideways flying ion of sufficient energy may be lost by hitting the side wall. This can lead to an absence of ions that would otherwise fall in the centre of the time of flight peak.

As for the single-field derivations the equations above assume a single spot of initial light-matter interaction. To allow a small deviation $\pm\delta s$ within the ionisation region the time focus conditions derived from $\frac{dT}{ds} = 0$ yield

$$D = 2s\sqrt{k_0^3}\left(1 - \frac{1}{k_0 + \sqrt{k_0}}\frac{d}{s}\right)\,, \tag{3.22}$$

where

$$k_0 = \frac{sE_s + dE_d}{sE_s}\,. \tag{3.23}$$

This implies a much greater flexibility with the tunable parameters s, d, E_s and E_d, and confers several advantages in the design of the instrument. In addition to allowing much longer drift tube lengths (improving time and mass separation), it allows the ionisation region and acceleration region to be very small. This reduces external noise and limits the time spent within these regions, and allows for a greater time spent in the drift tube. This implies that the ions reach their final kinetic energy after about 5% of the flight time, thus greatly reducing disturbance.

3.4.3 Ion mass spectrometer

In the investigations of this thesis, two different ion mass spectrometers of the Wiley-McLaren two-field type have been used: a shorter instrument of about 12 cm length and a longer spectrometer of about 50 cm length. Both apparatuses can be mounted on our electron spectrometer and work together to detect both electrons and ions in coincidence, or can be used as stand-alone machines.

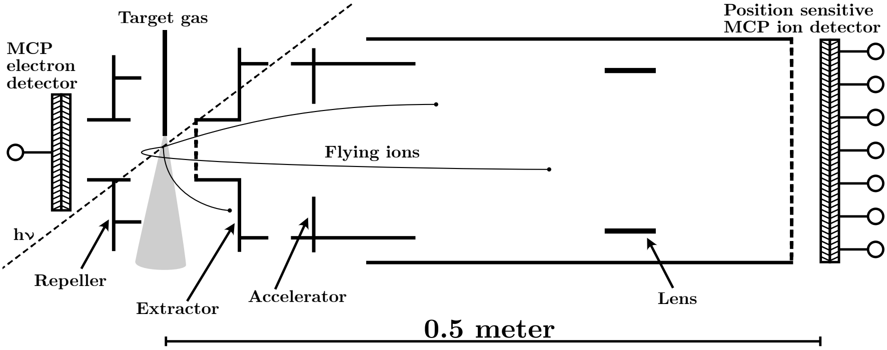

Figure 3.8: Ion apparatus used in paper I.

The longer 50 cm tube was used as a stand-alone apparatus in paper I. The ion mass spectrometer is illustrated in Figure 3.8 where the light intersects the effusive jet of the target gas. The strong static electric fields quickly extracts the electrons to a nearby MCP detector which are used as the start signal for the ions' time of flight. The ions are steered in the opposite direction, going through a mesh into the acceleration field. In experiments producing high kinetic energy release, the fragments, in particular the lighter ions, may fly too far sideways and thus miss the aperture but hit the surface of the extractor plate. The ions are accelerated about 4 kV in total and drift to a position sensitive MCP detector.

Compared to the magnetic bottle which collect almost 100% of the emitted electrons, the mass spectrometer suffers greater losses. The gradient of the electric fields is solely in the flight tube axis and thus no compensation exists for sideways flying ions, whose perpendicular momenta remain constant. Such ions often hit the front of the extractor plate or the side of the flight tube on the way to the detector. The apparatus in Figure 3.8 has a lens to partially limit the loss but this has the dire cost of any position information used for velocity map imaging. As the acceleration of the ions depends on both the mass and the charge, different ion species under the same experimental conditions will have different collection efficiencies with collection typically less for lighter, faster ions.

3.5 Augmented in-line electron and ion spectrometers

The magnetic bottle time of flight electron apparatus is very useful to experimentally analyse multi-ionisation processes. To dig even deeper an ion spectrometer can be mounted co-linearly such that both electrons and ions can be detected simultaneously [35]. This allows for thorough analysis of the ionisation energies leading to different dissociation channels and final ion states of molecules. In this configuration, the conical permanent magnet in Figure 3.4 is replaced by a hollow ring magnet shown in Figure 3.9. Ions are allowed to pass through the magnet into a short drift tube and their flight times are recorded by an MCP.

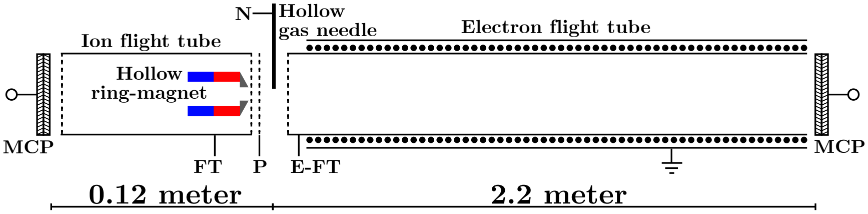

Figure 3.9: Electron-ion apparatus simultaneously utilising the ion mass selection in coincidence with the magnetic bottle electron spectrometer.

Upon photoionisation, electrons are emitted and captured by the magnetic bottle and steered through the 2.2 m electron drift tube. A mesh is placed at the beginning of the electron flight tube which allows an electric field to be applied across the ionisation region without affecting the electrons that have already passed through the mesh. About 150 ns after the light pulse, once all relevant electrons have passed through the mesh, a strong extraction field is applied on the needle (N) and pulser plate (P) to guide the ions through the hollow ring magnet toward the ion MCP. The ion flight tube (FT) is kept constant at -1000 V and the electron flight tube (E-FT) at or near ground. The signals from both the ion and electron MCP detectors can then be sent to the same acquisition system.

3.6 HNCS synthesis

Most presently used target samples come in gas form stored in lecture bottles or as vapour from liquids, both of which can be commercially procured. More unstable molecules, such as HNCS, have to be synthesised or produced in other ways shortly before use to avoid sample decomposition and polymerisation. The HNCS sample can be prepared in a test tube which is attached to the apparatus gas inlet system during the experiment.

HNCS can be synthesised by mixing potassium thiocyanate and potassium bisulphate at a specified temperature. The two reagents are dried separately over phosphorus pentoxide in vacuum desiccators for about two weeks. The reagents are finely ground and layered in a glass test tube, separated by glass beads, and the layers are pumped in rough vacuum for at least 24 hours. The layers are cooled in liquid nitrogen (LN2) to limit the reaction rate as the reagents are mixed. The tube is shaken vigorously for about 20 seconds and cooled again in LN2, which is repeated until fully mixed.

The mixture is put on the gas inlet system where it is pumped at -80 °C, cooled by an LN2-alcohol mixture, reaching a pressure close to what a rough pump can handle. Once the tube is sealed off from the vacuum pump and opened to the apparatus, the sample is warmed to -10 °C by a NaCl/ice which limits the reaction rate, reducing the polymerisation and allowing for the experiment to run for a sufficient amount of time (i.e. several hours). With the ice bath, the relative chamber pressure is much lower than typical gas phase experiments and the electron noise is very high, which is removed by selecting on ions. When only electrons are detected the sample is instead heated to 50 °C, quickly evaporating water and then allowing for a short run with high purity.

CHAPTER 4

Data analysis

The experimental data come in the form of time of flights, structured such that correlation information is preserved, separating electron and ion records. The first part of this chapter discusses the conversion from flight times to other useful scales, such as mass/charge for ions and kinetic energy and subsequently ionisation energy for electrons. This is followed by a description of coincidence analysis methods where the correlation of multiple particles is used to determine for example double ionisation energies.

Later on in the chapter, the numerical methods used to explain the experimental data are presented. First-principle quantum chemical calculations are used to determine the potential energy curves and dissociation limits. These yield possible pathways by calculating numerical appearance energies and kinetic energy releases. This is followed by numerical models used to describe dissociation mechanisms. The final ion fragments from the models are placed in a geometric replica of the apparatus where the ion's trajectory is calculated and recorded. These trajectories are explained in the final section and are used to quantify how the spectrometer operates by comparing the experimental data to these simulated experiments based on numerical models.

4.1 Time of flight conversion

The raw time-of-flight data exhibit varying utility, and typically require calibration and subsequent conversion into the more useful energy or mass scales. The raw time-of-flight ion-ion coincidence islands convey crucial information on kinetic energy release and are used both in converted and unconverted forms. Conversely, the electrons contain limited quantitative information in the time domain which necessitates conversion to kinetic energy in order to interpret them.

To understand the electron's flight time to energy relation it is practical to start with the kinetic energy formula $E_{\text{kin}} = \frac{mv^2}{2}$ known from mechanics. The electrons velocity can easily be determined by knowing the fixed distance, d, it flies to the detector together with the time, t, it takes to get there: $v = \frac{d}{t}$. This provides the ideal relation

$$E_{\text{kin}} = \frac{md^2}{2t^2} = \frac{D^2}{t^2}\,, \tag{4.1}$$

where the electron mass and travel distance are grouped into one calibration constant $\frac{md^2}{2} = D^2$. Experimentally measured flight times deviate from this ideal form and some extra calibration constants are necessary for a good fit. The ideal form assumes that the start signal triggered off the light is recorded by the acquisition system exactly at the time of ionisation, whereas in reality the signal must travel through cables and electronics that introduce additional delays and thus a calibration parameter t_0 is included where $t \to t - t_0$. Furthermore, in all the experiments in this thesis, a small voltage is applied across the interaction region to more efficiently capture the very slow, near zero kinetic energy electrons. This results in an offset in the kinetic energy and thus a calibration parameter E_0 is included as $E_{\text{kin}} \to E_{\text{kin}} + E_0$. The final form of the conversion formula from flight time to energy is expressed as

$$E_{\text{kin}} = \frac{D^2}{(t - t_0)^2} - E_0\,, \tag{4.2}$$

or the inverted

$$t = \frac{D}{\sqrt{E_{\text{kin}} + E_0}} + t_0\,. \tag{4.3}$$

Equations 4.2 and 4.3 are always approximations because in reality there are several regions, mainly the source; the space between the source and the flight tube; and the space between the flight tube and the electron MCP cathode, where different fields (intentional or not) are present. A more complete representation is a flight time which sums the contribution from all regions, modifying Equation 4.3 to

$$t = \frac{D_0}{\sqrt{E + E_0}} + \frac{D_1}{\sqrt{E + E_1}} + \frac{D_2}{\sqrt{E + E_2}} + \ldots + t_0\,. \tag{4.4}$$

Such an expression is a difficult task to invert, especially if the calibration data is limited to just a handful of points. In most cases, Equation 4.2 turns out to be sufficient but if a strong retardation is used or many unwanted fields are present, Equation 4.4 with two or more terms may be necessary.

The flight time of an ion, as discussed in chapter 3, depends on its mass, m, and charge, q, in addition to many other terms from the electric acceleration field strengths and lengths. The latter remains constant independent of the measured ion and can be grouped into the calibration constant A in the simple calibration equation:

$$\mathrm{TOF} = A\sqrt{\frac{m}{q}} + t_0 \,. \tag{4.5}$$

Similar as in electron calibration, a parameter t_0 is included to correct for the exact timing of the true start of the ions flight time. As mentioned, the kinetic energy release can be estimated from the raw time of flight spectrum by the width of the peak. The width is the time difference between an ion flying directly backward and directly towards the detector, and the only non vanishing term are from Equation 3.18

$$\Delta T = T_+ - T_- = \frac{\sqrt{2m}}{qEs}(\sqrt{U_0} - (-\sqrt{U_0}))\,, \tag{4.6}$$

which can be expressed as

$$U_0 = \frac{\Delta T^2 q^2 E_s^2}{8m}\,. \tag{4.7}$$

Here, U_0 is the kinetic energy release, ΔT is the full width of the peak at half max and E_s is the field strength in the source region.

4.2 Calibration of electron spectra

The conversion of electron time of flights to kinetic energies relies on finding the calibration parameters D, E_0 and t_0 which under ideal conditions are assumed to be constant for the duration of an experiment. Calibration spectra of well characterised samples are recorded before and after a series of runs to assess whether the calibration parameters have in fact changed. Most often E_0 may drift, e.g., due to electric charges building up on surfaces in the spectrometer due to chemically aggressive target gases. In these instances, the data is carefully checked over time and adjustments may be made, either to the experimental apparatus or accounted for in the analysis.

For a typical double photoionisation experiment in Gothenburg the standard calibration gas is molecular oxygen, O_2, using photon energies of

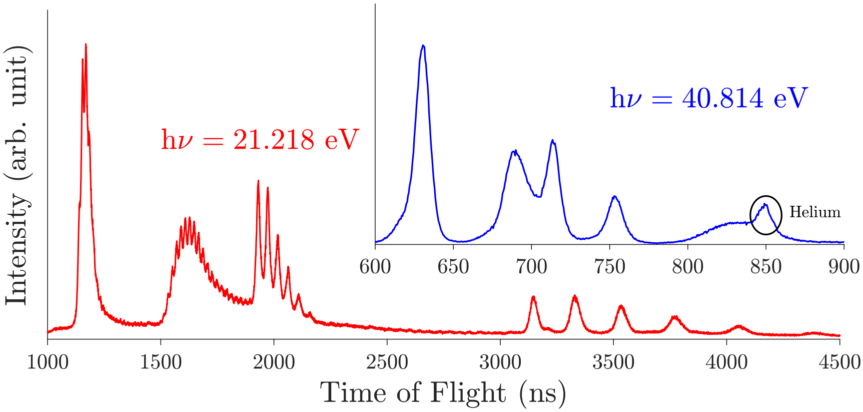

Figure 4.1: Raw time-of-flight spectra of O_2 ionised with 21.218 eV (red) and 40.81 eV photons (blue). The black circle shows an additional peak from the ionisation of helium that escape the light source and enter the interaction region.

Table 4.1: The relevant states and vibrational levels of O_2 [36] used in the calibration. Listed are the binding energies with the associated kinetic energies upon ionisation using 21.22 eV photons.

State	Vibrational level	Binding energy (eV)	Kinetic energy (eV)
X $^2\Pi_g$	0	12.083	9.135
	1	12.316	8.902
	2	12.544	8.674
	3	12.756	8.462
a $^4\Pi_u$	2	16.349	4.869
	3	16.469	4.749
	4	16.588	4.630
	5	16.703	4.515
	6	16.816	4.402
	7	16.926	4.292
	8	17.034	4.184
	9	17.138	4.080
	10	17.239	3.979
	11	17.338	3.880
b $^4\Sigma_g^-$	0	18.171	3.047
	1	18.315	2.903
	2	18.454	2.764
	3	18.590	2.628
	4	18.721	2.497
B $^2\Sigma_g^-$	0	20.296	0.922
	1	20.434	0.784
	2	20.566	0.652
	3	20.693	0.525
	4	20.815	0.403
	5	20.930	0.288

the strong helium emission lines from He I and He II. Figure 4.1 shows raw time-of-flight example spectra of O_2 recorded at the photon energies of 21.218 eV and 40.814 eV in red and blue, respectively. The lower photon energy produce electrons in the kinetic energy region 0 to 9 eV as shown in Table 4.1, where the binding energies and related kinetic energies of all vibrational levels included in the present calibration are listed. The higher photon energy ionises from the same states but the corresponding kinetic energies are higher where the ability to resolve the vibrational levels vanishes. Here, the peak average is used instead of the individual vibrational states. In addition, for the higher photon energy the single ionisation of helium is visible in Figure 4.1 with electrons of kinetic energy of 16.23 eV. The helium is not in the molecular jet but rather leaks in from the light source which might give misleading results. The calibration curve fitted by plotting the experimental flight times for each peak against the known energies is shown in Figure 4.2. For an accurate calibration it is necessary to have points over a broad range of energies with both high and low kinetic energy electrons. It is fortunate that the ionisation energy of the O_2^+ B states are just below the He I emission energy, which creates sub 1 eV kinetic energy electrons (fast electrons are much easier to come by) reflecting several vibrational levels of this state. At synchrotron radiation facilities the photon energy is tunable at very high accuracy and low energy electrons are easily created using photon energies just above an inner shell threshold using, for instance, argon or neon.

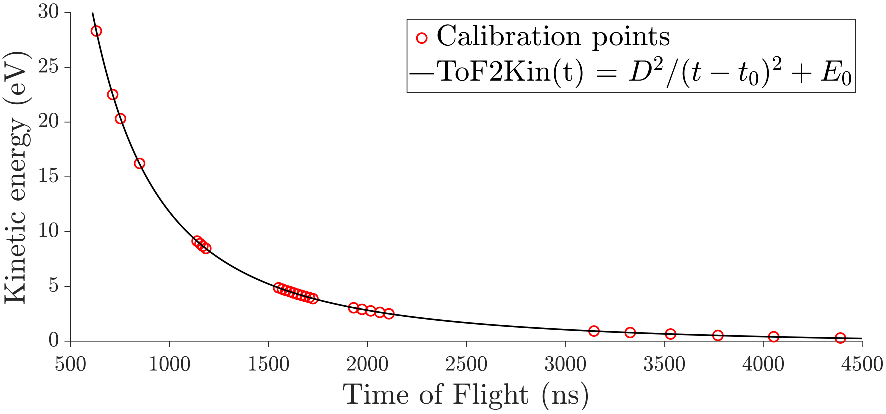

Figure 4.2: The curve fit using the binding energies in Table 4.1 and the TOF-peaks in Figure 4.1.

Once the calibration constants are accurately derived, they can be used to determine the kinetic energy of the electrons produced from any sample. Here, for simplicity, the calibration is demonstrated using O_2. Figure 4.3

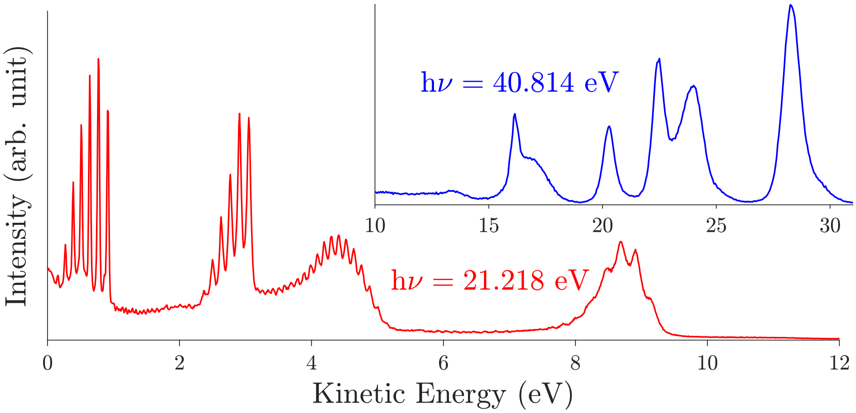

Figure 4.3: The time of flight in Figure 4.1 converted to kinetic energy using the curve fit from Figure 4.2. The red (blue) curve shows the kinetic energy of electrons from ionisation of O_2, initiated by photons at energy 21.218 eV (40.814 eV).

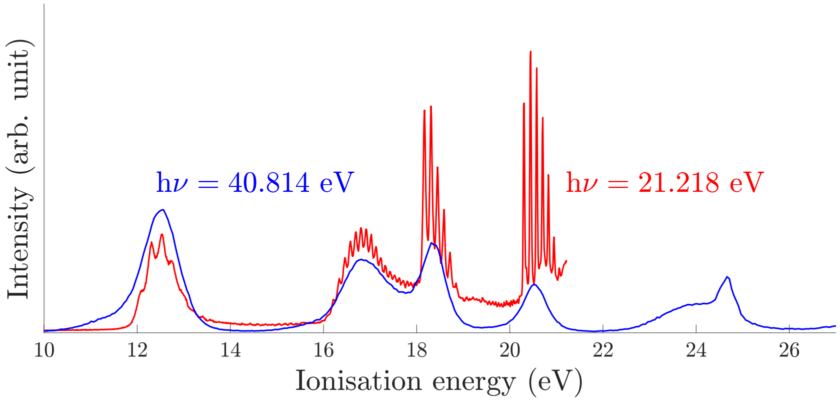

Figure 4.4: Ionisation energy spectra of O2 using photons at 21 eV and 41 eV. The spectra align as the ionisation energies are the same regardless of photon energy, however, the resolution differ.

shows the kinetic energy spectra of O_2 photoionisation for two photon energies after conversion. The features and their spacing in the two spectra resemble each other but the blue is shifted to higher kinetic energies due to the higher photon energy. Since the kinetic energy spectra depend on the photon energy used, it is necessary to convert to ionisation energy for a direct comparison with other experiments or theory. The spectra are shown on an ionisation energy scale by the simple conversion $E_{\mathrm{IP}} = h\nu - E_{\mathrm{kin}}$ as in Figure 4.4. Now, the peaks corresponding to identical ionisation energy overlap and the red curve ends at 21.218 eV since it is unable to ionise higher than the provided photon energy. The difference in resolution for the same states with different final kinetic energy is clearly seen where the blue curve does not reflect individual vibrational states which is expected when considering the resolving power of the time-of-flight magnetic bottle. Nominally, the apparatus is able to resolve differences in kinetic energy as $\frac{E}{\Delta E} = 50$ in electron only mode (as used for the examples) and $\frac{E}{\Delta E} = 20$ in electron-ion mode. In this example the first ionisation energy around 12 eV yield kinetic energies of $\sim$ 9 eV and $\sim$ 29 eV from the photon energies of 21.218 eV and 40.814 eV, respectively. The maximum resolving power at these energies are $\Delta E = \frac{9 \text{ eV}}{50} = 0.18$ eV and $\Delta E = \frac{29 \text{ eV}}{50} = 0.58$ eV and by Table 4.1 the X $^2\Pi_g$ vibrational levels are about 0.2 eV apart, which is clearly resolvable at the lower photon energy but not the higher.

4.3 Coincidence analysis

The core objective of coincidence analysis is to correlate the properties of particles produced by the same event to unambiguously identify the underlying process. Coincidence analysis relies on recording and storing, in our case flight times of all particles such that the correlation information is preserved. Experimentally this is realised by two factors: using a pulsed light source, and keeping the ionisation rate below 1% of the light pulse repetition rate. The pulsed light source has properties that ensure all electrons and ions created reach their respective detectors before the next ionisation event occurs. The low ionisation rate is to limit false coincidences involving uncorrelated electron emissions from different ionisation events that occur within the same, or from different, light pulse(s). Experimentally, the rate is controlled by monitoring the count rate relative to the light pulse rate and is adjusted by varying the target gas pressure, and at synchrotron facilities by varying the light intensity.

The records of all measured electrons and ions generated in the same event can be structured to retain the correlation information. The datasets are recorded as multiple rows of raw flight times, with each row corresponding to all the detected particles for a given event. To distinguish hits from different detectors, the detections on the electron MCP are flagged by artificially assigning a negative time-of-flight, whilst the detections from the ion MCP are positive. The ordering is based on the time of flight, with ion events taking precedence, followed by the electron events.

These data can then be presented in form of multidimensional plots called coincidence maps. A two-dimensional coincidence map may show the flight time of two particles with one particle on the x-axis and the other on the y-axis. Visually, correlation between the particles typically present as curves or islands. For higher order coincidences, the particles can be examined pairwise in multiple steps. A typical example is that of two electrons with one ion. Here, the correlation of the electrons are preferably studied together with a selected ion whose mass/charge is chosen but not viewed.

4.3.1 Electron-electron

In double ionisation processes, two electrons are emitted where it is sufficient to study correlated electron pairs in two-fold coincidence. The electron pair appear as points on the map with the flight time of electron 1 on one axis and electron 2 on the other axis. Figure 4.5 depicts a Monte Carlo simulation of electron pairs that share an excess energies of 4.5, 5, 5.5 or 10 eV, broadened by a random Gaussian distribution to emulate realistic experimental conditions. Here, noise is included by randomising two uncorrelated electrons uniformly across all possible flight times. The correlated electron pairs share their combined excess energy completely arbitrarily and as the kinetic energy scales to the inverse of the flight time squared, the energy sharing curves are parabolically shaped. For clearer illustration, the plots depict both e_1 versus e_2 and the transpose e_2 versus e_1 to cover both the lower and upper parts of the figure. On the diagonal, there is a small gap which is due to an experimental dead time. The dead time is

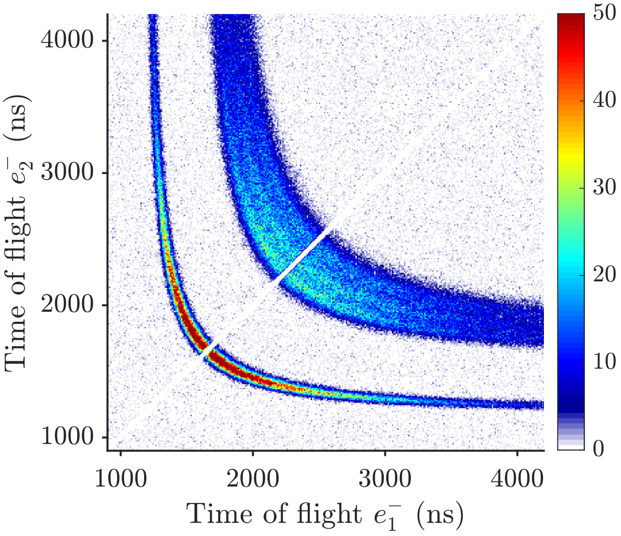

Figure 4.5: Illustration of an electron TOF coincidence map based on electron pairs sharing excess kinetic energy. The shared excess energies are 4.5, 5, 5.5 and 10 eV with an additional spread from a Gaussian distribution in the energy domain.

caused by the detection scheme where the discriminators are set to produce a pulse width of ≈ 10 ns and thus two signals closer in time than this will only broaden the discriminated signal which will be registered as one particle.

The electron flight times are converted to kinetic energy using Equation 4.2 and plotted thusly, the sharing of excess energy manifests as straight lines as shown in Figure 4.6. The straight lines on the anti-diagonal imply a constant electron pair energy sum, where the uppermost curve corresponds to 10 eV excess energy. The lower, wider band, corresponds to the three excess energies 4.5, 5 and 5.5 eV which due to the Gaussian distribution appear as one broad feature. There is a strong signal at the origin which comes from random noise. The noise is uniformly distributed in time, however, when converted to energy the noise at very long flight times (low energies) gets concentrated due to the larger flight time window corresponding to a single fixed width energy bin.

Figure 4.6 gives some idea about the electron pair energies but a clearer picture is realised by choosing one axis for the double ionisation energy using

$$\mathrm{DIE} = h\nu - \left(U(e_1^-) + U(e_1^-)\right), \tag{4.8}$$

where $U(e_1^-)$ and $U(e_1^-)$ are the kinetic energies for electron 1 and 2, respectively, and a photon energy $h\nu$=41 eV is assumed. Figure 4.7 shows

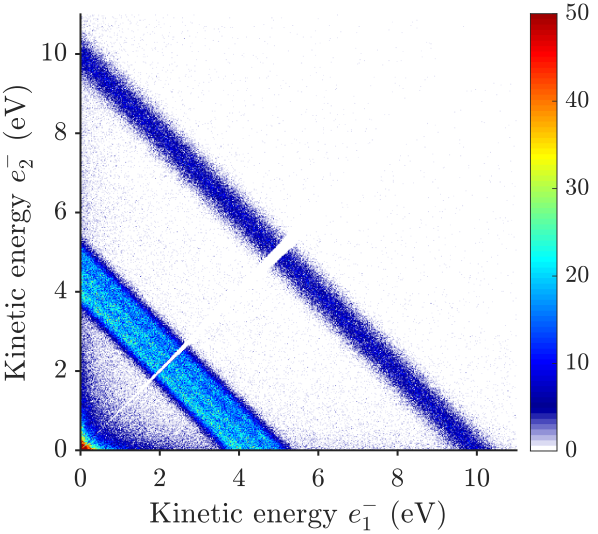

Figure 4.6: Illustration of an electron kinetic energy coincidence map converted from the data in Figure 4.5. Both axes show electron kinetic energy and the straight lines indicate that the energy sum is constant.

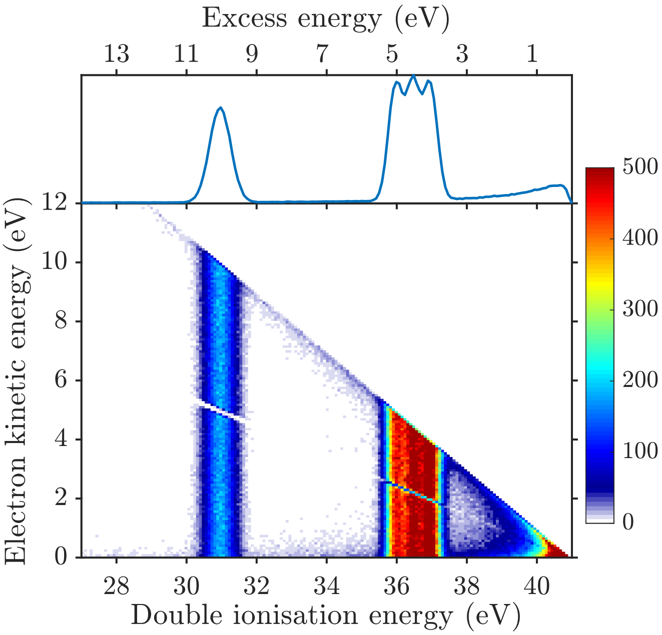

Figure 4.7: Illustration of an ionisation energy coincidence map, by assuming a photon energy of 41 eV from which the kinetic energy sum of the two electrons from Figure 4.6 are subtracted. The top panel shows the sum, or projection, of the coincidence map.

the double ionisation (excess) energy on the lower (upper) x-axis versus the two electron kinetic energies on the y-axis. The coincidence map is projected to show a one dimensional spectrum of the double ionisation energy, with the excess energy shown on its upper x-axis. The background's noise profile is clearly seen at the higher energies but more importantly the different excess energies 4.5, 5 and 5.5 eV are now more clearly separable.

These typical steps in analysing electron coincidences are crucial to determine the nature of a feature in the double ionisation data and distinguish real peaks from those generated by noise or artefacts. However, the final results are typically only presented using the 1D projection of the DIE spectrum. This work uses only two electron coincidences but the general concept can also be extended to studies of processes involving more electrons, as shown in Refs. [37, 38, 39].

4.3.2 Multi-ion

Fragmentation of multiply ionised molecules leads to several correlated ions whose origin can be explored with the use of coincidence maps. In diatomic fragmentations producing two ions, their momenta are equal and opposite. The initial molecule may be orientated randomly in space upon photoionisation and thus the ions fly in all directions. With full angular collection, the shape of the island in the coincidence map for these ions is a straight line with negative slope, as shown in the left panel of Figure 4.8. The ions flying perpendicular to the flight tube direction appear as zero kinetic energy, as they have no forward momenta, and land at the centre of the island. In processes leading to high kinetic energy release, the ions have a higher risk of not reaching the detector by hitting the inside surface of the spectrometer. Here, the centre of the island is diminished and in extreme cases the distribution will appear as two islets, as shown in the right panel of Figure 4.8.

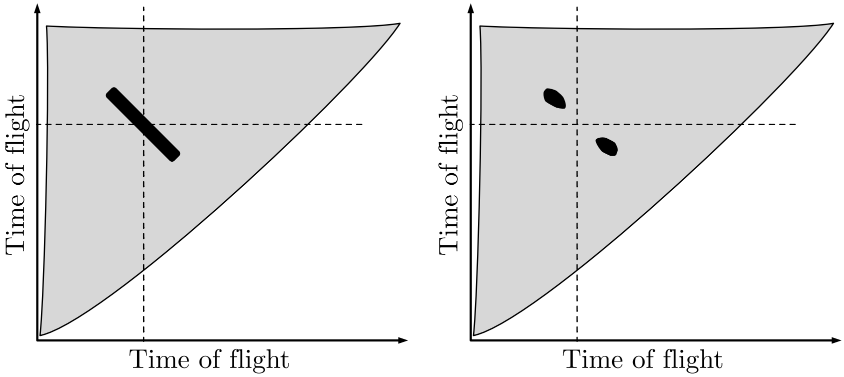

Figure 4.8: Simple illustration of an ion-ion coincidence island. The left panel shows an example with full angular collection and the right panel a similar example where sideways flying ions are lost, resulting in two smaller islets with an absence of signal in between them. The dashed lines indicates the position of thermal ions.

When studying events where more than two products are released simultaneously, a simple pairwise coincidence analysis is typically insufficient. A direct multi-dimensional coincidence is theoretically possible but the preferred method is by multiple pairwise coincidence maps. The following example show a case involving three ions A^{l+}, B^{m+} and C^{n+} with charges l, m and n assuming the ion flight times obey

$$\mathrm{TOF(A)} < \mathrm{TOF}(B) < \mathrm{TOF}(C) \tag{4.9}$$

The left panel in Figure 4.9 shows the pairwise coincidences of the second (B) and third (C) ion with charges of +2 to +3 correlated with +2 to +5, respectively. Selecting the specific third ion C^{3+} when viewing the pairwise coincidences of the first ion (A) with the second ion (B) as in the left panel of Figure 4.9 the dedicated decay channels A^{l+}+B^{m+}+C^{3+} are viewed. The left panel shows that all B and C ions are anti-correlated, meaning that they initially fly in opposite direction. In contrast, ions A and B have a positive slope and are thus correlated, initially flying in the same direction.

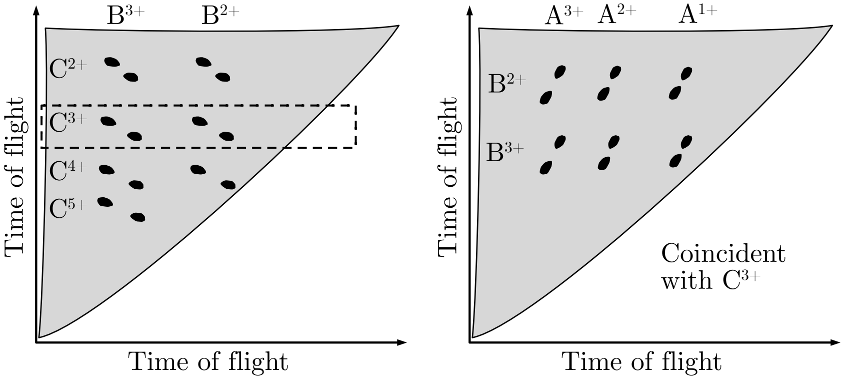

Figure 4.9: Stepwise analysis of triple coincidences using two separate coincidence maps reflecting pair correlations. The left panel shows ions B and C with a dashed box, indicating a selection region of the slowest ion C. The right panel shows ions A and B selected on C^{3+}. The slopes indicate that A and B are released in the same direction, but opposite to C.

4.3.3 Sequential ion fragmentation processes

The formation and dissociation of dications can be investigated using a simple two-fold coincidence map. Information about the process is encoded in the shape and slope of the ion-ion islands. For a molecule breaking into two fragments, the linear momenta is shared equally and opposite, illustrated by a straight line of slope -1 shown by (A) in Figure 4.10.

Double ionisation leading to three-body dissociation $ABC^{++} \rightarrow A^+ + B^+ + C$ is more challenging and can be discussed in form of three prototype mechanisms [40]:

$$\textit{deferred charge separation: } ABC^{++} \rightarrow AB^{++} + C \quad \rightarrow A^+ + B^+ + C \tag{4.10}$$
$$\textit{immediate explosions: } ABC^{++} \quad \rightarrow A^+ + B^+ + C \tag{4.11}$$
$$\textit{sequential dissociation: } ABC^{++} \rightarrow A^+ + BC^+ \quad \rightarrow A^+ + B^+ + C\,. \tag{4.12}$$

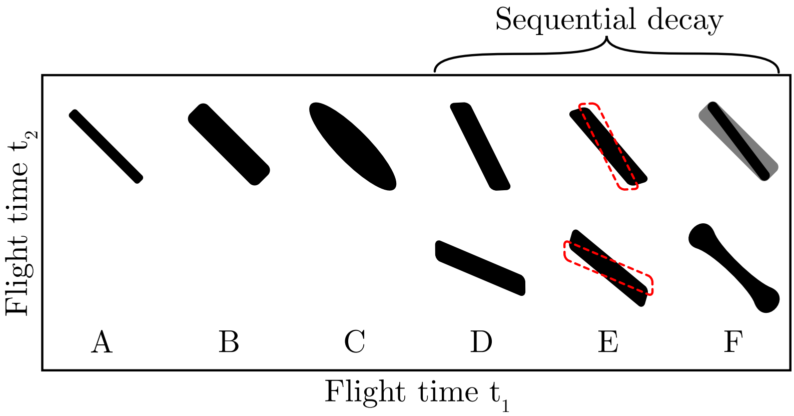

Figure 4.10: Illustrated peak shapes for common prototype mechanisms: (A) two-body dissociation; (B) deferred charge separation; (C) immediate explosion; (D) sequential decay with an expected slope; (E) sequential decay with a slope between the expected limited slope (red dashed) and slope -1; (F) twisted slope with different intense inner slope and outer edge slope (upper) and bow-tie (lower).

In *deferred charge separation*, (B) in Figure 4.10, the separation of the charges is delayed and the initial neutral separation acts equal on both observable fragments typically in arbitrary direction, similar to thermal velocity. The detectable fragments have the shape of a broadened two-body decay where the major part of the momenta are equal and opposite.

In the *immediate explosion* the fragments separate simultaneously where they are typically thought to have non-180 degree angle between them. This means that if one of the ionic fragments is released on axis, the other detectable fragment is not. The result is an oval shape, considerably wider at the centre, with a slope near -1, as seen by (C) in Figure 4.10. It's a frequent experimental shape and is very easily recognisable, but due to the large number of variables needed to describe its dynamics not much can be deduced from its shape.

Sequential dissociation is a two-step fragmentation process with an initial two-body separation between fragments A^+ and BC^+ and a subsequent decay of BC^+ to $B^+ + C$ (or $B + C^+$). In the simple case shown in (D) the initial two-body dissociation yield equal momenta to A^+ and BC^+ as the fragments separate beyond the effective Coulomb range. The BC^+ fragment may rotate to any direction before subsequent dissociation, leading to a broadening only seen in B^+, resulting in the parallel long sides, with vertical ends. The slope is different from the simple two-body dissociation since B^+ gains its momenta as the heavier pair BC^+ before it breaks and continues to travel as a lighter fragment. Linear momentum conservation dictates that the slope at the limit is $-(m_B + m_C)/m_B$, or the inverse $-m_B/(m_B + m_C)$, depending on if B is lighter or heavier than A, as the lighter fragment is typically projected onto the x-axis due to the flight time ordering of the coincidence data. If the second decay occurs at shorter times (on the femtosecond timescale) it can happen within the effective Coulomb range. In the initial fragmentation, B^+ will gain some of its momentum at the early stage as a heavier molecule BC^+ and subsequently, after 'losing mass', as the lighter B^+. This will affect the total momentum given to both A^+ and B^+ and change their slope, shown by (E) in Figure 4.10 where the dashed red box is the limiting slope. The slope can become steeper or more moderate. In addition, at shorter secondary lifetimes the timing is important as the BC^+ fragment may rotate with some lifetime to fixed time dependent angles. In general, these short lifetime sequential decays can produce twisted slopes with different inner and outer edge slopes (upper F), or bow-tie shapes (lower F).

It is critical to consider both the island shape and its slope simultaneously since some similar shapes can in theory be reproduced by different dissociation mechanisms. For example, the bow-tie shape was initially thought of as an immediate explosion where the unseen neutral centre fragment is released with momentum perpendicular to the separation axis of the charged fragments [41]. Additionally, fragmentation pathways leading to a neutral centre fragment $A^+ + B + C^+$ can break sequentially where the neutral is attached to either end, i.e an initial decay to AB^+ or BC^+. The two mechanism can have different limiting slopes, which in some cases can appear bone shaped.

4.3.4 Electron-ion

In experiments where both electrons and ions are detected simultaneously the ions are used to estimate kinetic energy releases and determine the final state products. In presentations of these data, the ions are typically a 'hidden parameter' where the ionisation energy of the electrons emitted is plotted separately for each ion species or decay channel in correlation. Figure 4.11 shows simulated threefold coincidences extended from Figure 4.7 where one ion is selected to show the appearance energy (AE) for specific fragmentation channels, compared with the full spectrum of all ions in black. The doubly charged parent ion ABC^{++} typically has the lowest DIE as it does not require crossing any potential barriers to be formed. Dissociation processes leading to A^+, B^+, C^+ and AB^+ fragments are shown where some pairs have the same ionisation energy. This implies a correlation where A^+ is formed together with B^+ plus a neutral C, or with BC^+.

In fourfold coincidence analysis (two electrons and two ions), both ions can be selected to unambiguously reveal the AE required to produce particular

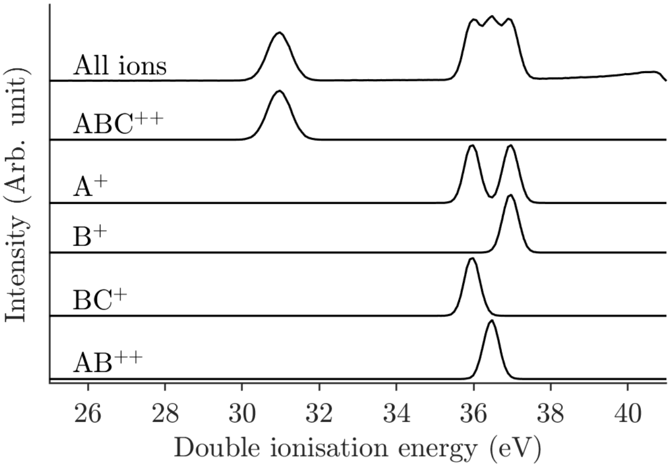

Figure 4.11: Simulated ion specific double ionisation energies based on Figure 4.7, which contain all ions shown by the black top curve. In this threefold coincidence illustration, the different final charge states are assigned a separate fragmentation channel. Here, one ion from each channel is selected together with the two electrons.

fragmentation channels, shown in Figure 4.12. These are plotted similarly to those as shown in Figure 4.11 but with much more clarity into the process, as a threefold analysis of four fragments may contain unwanted correlations from a contamination molecule with similar structure but an added part D, for example BCD.

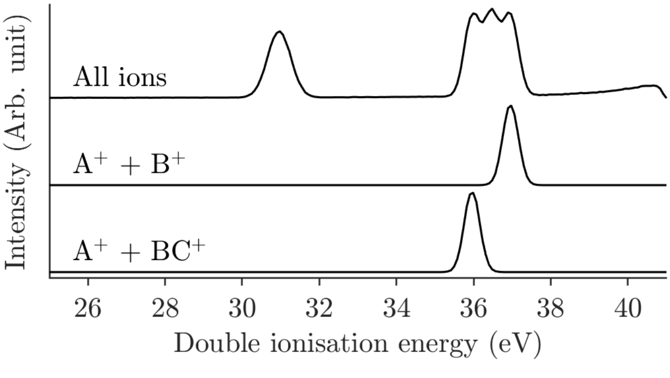

Figure 4.12: Simulated ion specific double ionisation energy as in Figure 4.11. In this fourfold coincidence representation, both ions from each channel are selected together with the two electrons, removing the ambiguity from threefold coincidence.

4.4 First-principle computations

In molecular ionisation, the electronic states may take a multitude of pathways leading to their final state, including isomerisation or fragmentation. To shed light on the experimental results it is often necessary to compare these to quantum chemical calculations.

4.4.1 Geometric minima and dissociation limits

To determine stable geometric configurations of molecular systems, the bond lengths and bond angles are varied as the total energy is computed for each step until convergence is found at some energy minimum. For the complete picture, all known isomers and all different fragments of the parent molecule are computed.

To determine the energy of local minima the method "partially spin restricted coupled cluster including perturbative treatment of triple excitations" (RCCSD(T)) [42, 43, 44] is used. The advantage of the couple cluster method is that it is size consistent, which means that computing two particles infinitely far apart yields the same energies as by computing the particles separately. i.e. $\mathrm{E}_{\mathrm{AB}}(r = \infty) = E_{\mathrm{A}}+E_{\mathrm{B}}$. This makes the RCCSD(T) method useful for computing dissociation limits since the dissociation limit of AB → A+B is precisely moving them infinitely far apart.

For quantum chemical computations, a basis set is specified to define the space in which the computational method operates. Here, the correlation-consistent basis set cc-pVXZ introduced by Dunning et. al [45, 46, 47] is used. X is replaced by the number of Z-functions included, X = D,T,Q,5,6,..., and for the work presented in this thesis Q and 5 are used. For sulphur containing molecules an additional tight d-function might be used (Q+d or 5+d) for improved accuracy [48]. This basis set follows a pattern, converging to the limit of the complete basis set (CBS) according to a fit function [49, 50]

$$E_{\mathrm{X}} = E_{\mathrm{CBS}} + \frac{A}{X^3}\,, \tag{4.13}$$

where E_{CBS} and A are fitting parameters for the energy calculated at $X = 4$ (Q) and $X = 5$.

The coupled cluster method is a single reference method where only one configuration is used, typically the Hartree-Fock configuration. One configuration means that only one specific occupation of molecular orbitals is included, for any given spin multiplicity. Hence, the drawback of the RCCSD(T) method is that it cannot compute excited states or map potential energy surfaces.

4.4.2 Electronic Structure Computations

To compute the excited states and map the potential energy surface (PES) multi reference methods are used. Here, the wave function is prepared using the "complete active space self consistent field" (CASSCF) method [51, 52]. The excited states within the same spin multiplicity for a given geometry are computed using the internally contracted "multi reference configuration interaction" (MRCI) method [53, 54, 55]. The MRCI method can be slowly convergent and quite computationally costly. In instances where it fails, within this work, the explicitly correlated MRCI-F12 [56] is used.

In CASSCF the "CAS" part refer to the space of active and inactive orbitals used in the computation. If computationally possible, all orbitals are used, but in larger molecules the inner orbitals are kept frozen and only the valence orbitals are used in the calculations. The SCF part means that the orbitals are optimised by slight variations in repeated iterations until the solution converges to the mean field, something that MRCI does not do. Hence, the wave function and orbitals are prepared using CASSCF. MRCI is a variational procedure that can accurately determine the total energy for several excited states at a given geometry. In varying the geometry by changing bond lengths and bond angles the PES is mapped. In contrast to the couple cluster method, MRCI is not size-consistent and thus typically fail for large molecules or long bond distances.

4.4.3 Interpretation and comparison to experiment

To understand the full picture the RCCSD(T) and MRCI calculations are used complementarily and are compared to the experimental results. The methodology is to analyse the experimental fragmentation pathways by studying the ion yield curves and ion-ion coincidence maps.

Figure 4.13 illustrates an example where both methods are used. The green area depicts potential energy curves for a doubly charged molecule ABC^{++}. Each geometry along the bond distance r_{AB} are computed for fixed bond length r_{BC} at the geometry from the neutral molecule, yielding a 1D potential energy curve for the dissociation leading to the fragments A and BC. The appearance energy shown in the figure corresponds to the experimental double ionisation energy where this fragmentation channel starts to occur. In typical computations, all angles $\angle$ABC are computed for each bond distance r_{AB} mapping a potential energy surface. When the density of states is high, with many curve crossings allowing a path downward in energy, the PES to be reduced to the minimum energy path. The minimum energy path, in the three-body system, is obtained by finding the lowest energy angle at each bond distance. Due to computational costs and the MRCI method being size inconsistent the PESs are computed only to the necessary bond lengths, i.e. beyond all potential energy barriers. Here, the RCCSD(T) method is used to compute the dissociation limits as depicted in the blue box. The kinetic energy release is obtained by the energy difference from the appearance energy and the dissociation limit, which may be directly compared to experiment. The dissociation limits are extracted for each charge state (and their spin multiplicities) for all involved fragments in the decay channel. Additional excited states may be included from tabulated values such as NIST [12].

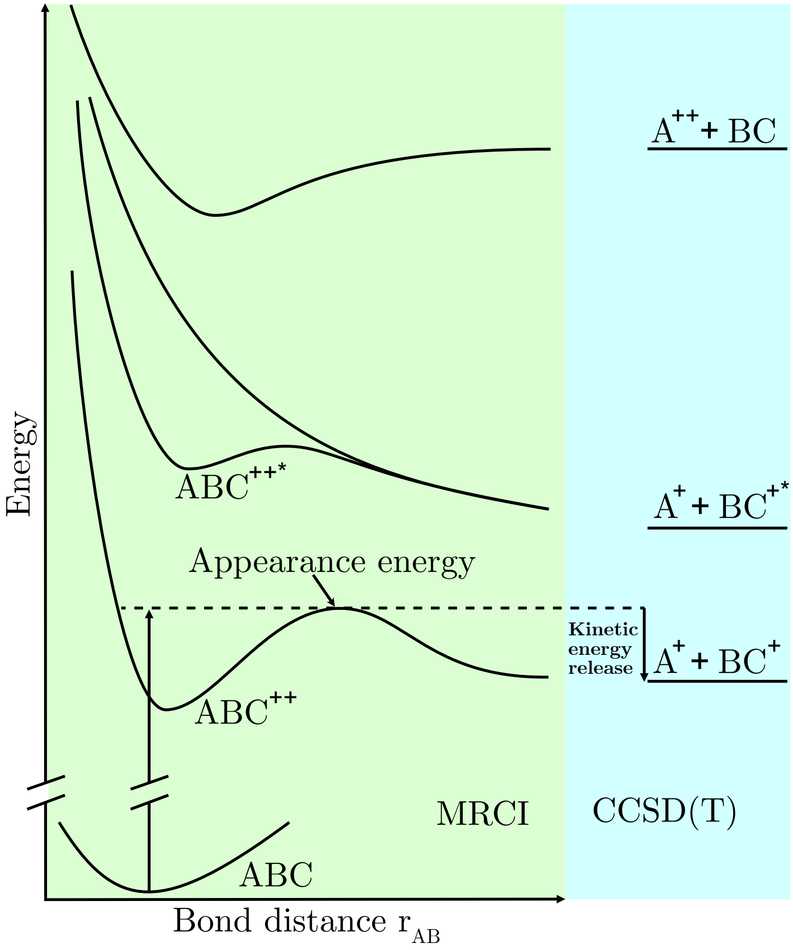
Energy
$A^{++} + BC$
ABC^{++*}
$A^{+} + BC^{+*}$
Appearance energy
Kinetic energy release
$A^{+} + BC^{+}$
ABC^{++}
MRCI
CCSD(T)
ABC
Bond distance r_{AB}

Figure 4.13: Examples of typical potential energy curves of a doubly charged diatomic molecule. To the right are the fragments at their dissociation limits.

4.5 Modelling fragmentation dynamics

In order to quantify the shapes of ion-ion coincidence islands it is necessary to understand the underlying fragmentation processes and what happens to these fragments when placed in a mass spectrometer. Typically, the modelling can be done in two steps: a classical trajectory (CT) simulation followed by a Monte-Carlo (MC) simulation. The CT determines how a molecule breaks into its constituent fragments by integrating the equation of motion under the influence of repulsive and attractive forces. The output from the CT simulations, the kinetic energy releases and directions of each charged fragment, are stored such that the correlation information is kept and used in the subsequent MC simulations.

4.5.1 Coulomb explosion

The Coulomb explosion, which is a highly charged form of immediate explosion, is modelled in a similar way to what Thomas A. Carlson and R. Milford White originally described in 1966 [57]. The charged fragments separate simultaneously, mutually governed by the strong Coulomb repulsion.

The molecule is placed in a Cartesian molecular frame with bond lengths and angles of the initial neutral molecule. Slight geometry variations can be applied to account for molecular vibrational modes, however, in the strong Coulomb repulsion this often has a negligible effect.

The fragments are given their respective final charges observed from experiment, either instantaneously or sequentially. The sequential charge build-up comes from the timing of the Auger-Meitner cascade which is typically involved when achieving very high charge states. The Auger-Meitner cascade can be triggered by filling of one or several deep core holes, whereby the charge is sequentially transferred to the other fragment ions after some time.

The charge repulsion is calculated using Lagrange mechanics, where the physical constraints on the system are built into its generalised coordinates, q, which defines the path of motion. It operates on a variational principle based on the action

$$S = \int_a^b \mathcal{L} dt \tag{4.14}$$

which define the overall motion of the system by integrating the Lagrangian $\mathcal{L}$ from point a to point b while following the path of minimum action. Introducing a small deviation to the minimum path yields the equations of motion for the physical system. In the present mechanical system this produces the Euler-Lagrange equation

$$\frac{\partial \mathcal{L}}{\partial q_j} - \frac{d}{dt}\frac{\partial \mathcal{L}}{\partial \dot{q}_j} = 0 \ . \tag{4.15}$$

The Lagrangian $\mathcal{L}$ is divided into the systems kinetic energy T and potential energy V:

$$\mathcal{L}(q, \dot{q}) = T(\dot{q}) - V(q) \ . \tag{4.16}$$

In the molecular system, the atoms' kinetic energy is from classical mechanics and the potential energy is the Coulomb repulsion experienced by the presence of each of the other charged fragments:

$$T = \sum_j \frac{m_j}{2} \dot{\boldsymbol{q}}_j^2 \tag{4.17}$$

$$V = k_e \sum_{j \neq i} \frac{Q_j Q_i}{|\boldsymbol{q}_i - \boldsymbol{q}_j|} \ , \tag{4.18}$$

where m_j is the ion mass and Q_j is the charge of ion j, k_e is Coulomb's constant and $\boldsymbol{q}$ is a generalised coordinate. Solving Euler-Lagrange yields the equation of motion

$$m\ddot{\boldsymbol{q}}_{\boldsymbol{j}} + k_e Q_j \sum_{i \neq j} Q_i \frac{\boldsymbol{q}_i - \boldsymbol{q}_j}{|\boldsymbol{q}_i - \boldsymbol{q}_j|^3} = 0 \ . \tag{4.19}$$

As the time dependent charges are building up and being transferred, the differential equation is solved numerically in small iterations, allowing for this change in charge, to a distance where the fragments no longer feel the Coulomb repulsion. The ion velocities are stored such that correlations are preserved for MC simulations.

4.5.2 Deferred charge separation

To model the dicationic sequential decay all molecules are approximated as a triatomic species ABC^{++}. The initial geometry ABC is defined by the neutral ground state and can be both linear or bent. The precise relative locations of A, B and C are distributed about the mean geometry with variations based on the vibrational modes of the harmonic ground state wavefunctions. The classical trajectories (CT) are calculated in two separate parts. The initial separation $\text{ABC}^{++} \rightarrow \text{A}^+ + \text{BC}^+$ always include Coulomb repulsion but may also include other effects such as: (i) polarisation of the charge cloud of A^+ by the charge cloud of BC^+ as an attractive force; (ii) the BC^+ dipole moment interacting with the charge of A^+; (iii) the strong short range repulsive part of the Lennard-Jones potential to stop the atoms from merging where attractive effects dominate over Coulomb repulsion at short distances. The strength of the interactions (i)-(iii) can be tuned and removed completely by setting their parameters to zero. The ion motions are calculated and allowed to propagate until a randomised time based on an exponential lifetime of the secondary decay of the BC^+ fragment. As BC^+ dissociates to $B^+ + C$, with a specified secondary kinetic energy release, the simulation propagates the trajectories where the motion of A^+, B^+ and C are only governed by the simple Coulomb repulsion. At long distances the fragments no longer affect each other, whereby the positions and velocities are stored.

4.5.3 Ion trajectory calculations

To compare the calculated CTs of the Coulomb explosion and deferred charge separation with experimental findings it is necessary to emulate the ion time-of-flight mass spectrometer (TOF-MS) computationally. This can be done in software such as SIMION [58] which can simulate the geometry and calculate the electrostatic potentials present in the apparatus, that govern the ion flight paths and can calculate them for particles with a given initial kinetic energy, velocity, mass, charge, and position. The output from the CTs are the fragments' kinetic energies and velocities in the molecular frame. It is important to correctly map the molecular frame of each individual CT event to the laboratory frame of the TOF-MS. This is done by carefully rotating the molecule uniformly, avoiding common mistakes of increased densities at the spherical poles. The initial positions are distributed in the source region of the TOF-MS to account for the finite volume of the intersection of the light path and the gas plume of target gas. The static electric fields are set to replicate the experimental conditions.

CHAPTER 5

Results

The experiments presented in this thesis all explored multi-ionisation processes leading to fragmentation in molecules, employing the experimental techniques outlined in Chapter 3. Specifically, data collection was conducted using a two-field ion mass spectrometer in conjunction with a magnetic bottle time-of-flight electron spectrometer. The light sources utilised included a pulsed helium discharge lamp in Gothenburg and synchrotron radiation provided by SOLEIL in Paris and BESSY II in Berlin.

The comprehensive results obtained from these experiments are presented in papers I-IV. In the subsequent sections, the most significant findings derived from these studies are highlighted.

5.1 Coulomb explosion of CD_3I upon L-shell photoionisation

Paper I builds on, and extends substantially the original work of Carlson and White from 1966 [57] where they first explored Coulomb explosion in methyl iodide/iodomethane. The multi-ion coincidence apparatus, described in Section 3.4.3, was used to investigate the Coulomb explosion mechanism in fully deuterated methyl iodide, CD_3I. With modern advancements in synchrotron radiation storage rings with tunable photon energy, we could extend the investigation by using three different X-ray photon energies, 4660, 4950 and 5290 eV, to generate core vacancies in the iodine's deep inner shells

L3 ($2p_{3/2}$), L2 ($2p_{1/2}$) and L1 (2s), respectively. These deep lying orbitals remain predominantly atomic in character, and efficient Auger-Meitner decay is initially localised on the iodine atom. As the decay cascade traverses to higher lying orbitals it reaches the orbitals of molecular character, and thus the charge is transferred to the other atoms. The charged moieties rapidly repel each other by the strong Coulomb repulsion, leading to fragmentation via Coulomb explosion. The efficient relaxation yields charge state sums up to 16+ where the charges are spread across the molecule.

Time dependence of ionic charges can, in principle, be calculated by solving a large set of rate equations involving all possible Auger-Meitner decay. However, this is very time inefficient. Instead, a comparatively simple two-parameter model initially employed by Koji Motomura et al. [59] was explored. Motomura studied the same molecule but used instead an intense X-ray free electron laser for few-photon absorption over a 10 fs pulse duration.

With a final fragmentation channel: $3D^{+}+C^{n+}+I^{m+}$, the two-parameter model assumes the time dependent total charge Q_{tot} to be built up sequentially, predominantly by Auger-Meitner cascade, initially at the site of the iodine atom. This is according to:

$$Q_{\text{tot}}(t) = (m+n+3)(1-e^{-t/\tau}) \,, \tag{5.1}$$

where τ is a parameter for the charge build-up time and Q_{tot} is the time dependent total charge. As the total charge increases, the charge imbalance lead to simultaneous charge transfer to the methyl group according to the rate function

$$\frac{d}{dt}Q_{\text{CD}_3}(t) = R \cdot Q_{\text{I}}(t) \,, \tag{5.2}$$

where R is a rate constant for the charge transfer, Q_{I} and Q_{CD_3} are the time dependent charges currently located at the iodine and the methyl group, respectively, and at any time t they sum to the total charge

$$Q_{\text{tot}}(t) = Q_{\text{CD}_3}(t) + Q_{\text{I}}(t) \,. \tag{5.3}$$

The ions are allowed to have fractional charges during charge build up, reflecting the effects of delocalisation and screening, but all fragments have integer-charge final states. When the methyl group's total final charge is at least 4, the deuterium atoms each get 1 charge and the carbon the remaining charge.

Using the model in comparison to our experimental results, an overall agreement is found for $\tau = 7$ fs and $R = 0.37$ fs^{-1}, a slightly lower time constant than the $\tau = 9$ fs found by Motomura [59]. Example comparisons to the experimental ion islands are shown in Figure 5.1 together with the very

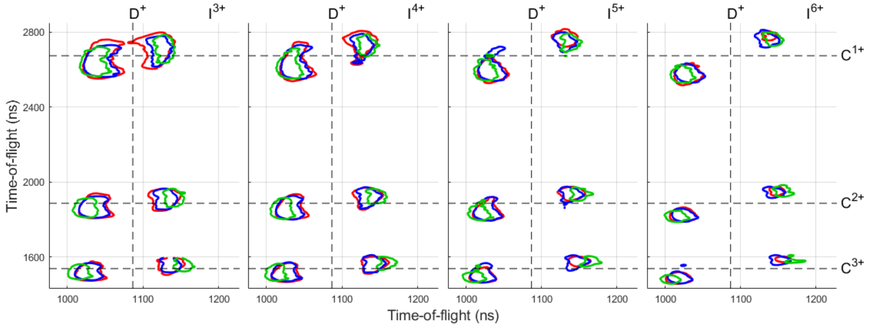

Figure 5.1: Ion pair contours of the deuterium-carbon ions of charges 1+ and $n+$, respectively, correlated with different charges $m+$ of iodine. The dashed lines indicate the flight time of thermal zero kinetic energy ions. The red contour represents the experimental data. The blue contour reflects numerical data using the charge build-up model with charge transfer. The green contour is based on the instantaneous model. The contour lines represent for 6% maximum intensity.

simplistic instantaneous model where all fragments are immediately given their final respective charges. It is very clear that the instantaneous model poorly predicts the dynamics as it overestimates the kinetic energy releases (KERs), whereas the charge build up model align with the experimental data rather successfully.

The light-weight deuterium fragment is by far most sensitive to variations in the simulation model and charge build up parameters. For this reason it is used to depict a comprehensive reflection of all charge states, as shown in Figure 5.2. Here, the time-of-flight (TOF) peak separation of D^+ correlates with carbon and iodine with charges 1-4 and 1-9, respectively. The islet separation is selected as the time at half the full peak height on the outside of each peak (forward and backward). The experimental TOF data with intensity I are assumed to have a statistical error $\sqrt{I}$, following the concepts of Bevington [60], and from this the deuterium separation extremes are deduced. The extremes of the deuterium peak shapes are estimated by using the maxima, $I + \sqrt{I}$, at the top of the peak together with the minima, $I - \sqrt{I}$, at the wing and conversely the peak minima with the wing maxima. Effectively, the full width half maximum is shifted and these extremes are shown by the error bars in Figure 5.2. It is clear that the charge build-up model agrees best with the experiment for intermediate n from 1 to 3, and m from 3 to 6, where the experimental statistics are reasonably high.

The total charge state distribution for initial L1, L2 and L3 core vacancies can be determined by subtracting the data sets in a well thought-through way, making use of an additional data set at 4300 eV where only the

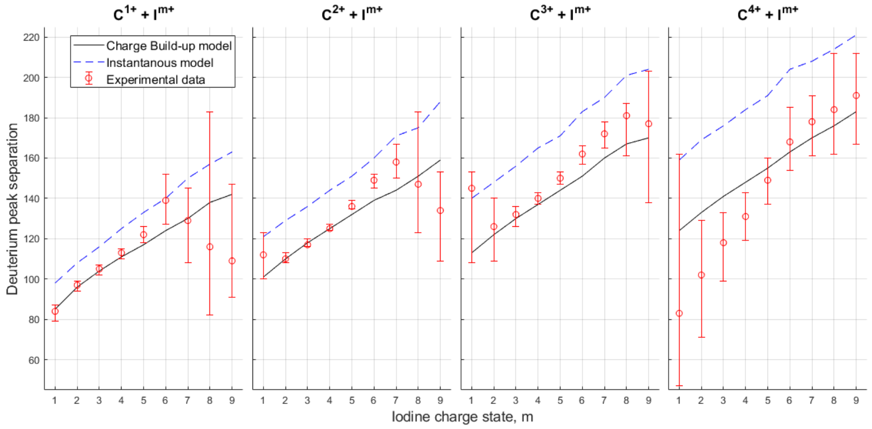

Figure 5.2: Comparison of the deuterium islet peak separation (in ns) in triple coincidence events with C^{n+}+I^{m+}. Dashed blue lines are the instantaneous model, the solid black lines are from the charge build up model with charge transfer, and the red error bars are the experimental data. The error is estimated using the FWHM at the extremes of the statistical intensity error.

higher lying orbitals are ionised. The cross section of an orbital is strongest just above threshold and goes down according the polynomial photoelectric cross section with $E^{-7/2}$ [61] as the dominating term. To separate core vacancy contributions in the data sets, the relative partial cross sections at a specific photon energy are estimated by fitting the polynomial to the total photoelectric cross section from the NIST database XCOM [62]. Denoting the data sets as $D1, D2, D3$ and $D4$ for the data acquired at the photon energies of 5290 eV, 4950 eV, 4660 eV and 4300 eV, respectively, combined with the theoretical relative partial cross sections the following set of equations is obtained:

$$\mathrm{L3} = D3 - 0.3251 \cdot D4 \tag{5.4}$$

$$\mathrm{L2} = D2 - 0.7518 \cdot D3 + 0.0125 \cdot D4 \tag{5.5}$$

$$\mathrm{L1} = D1 - 0.8076 \cdot D2 - 0.0704 \cdot D3 + 0.0121 \cdot D4. \tag{5.6}$$

Figure 5.3 shows the abundance of final charges extracted after the subtraction, in addition to correcting for the relative collection efficiencies of each fragment using SIMION [58] trajectory simulations for each ion at their respective KER. The three shells display similar distributions, albeit L1 is shifted to higher charge states. This can be related to a fast Coster-Kronig transition, filling the L1 hole with an L2 or L3 electron, emitting

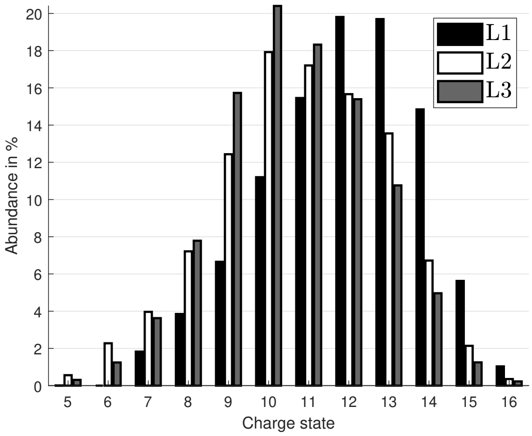

Figure 5.3: Relative charge state abundance of CD_3I estimated from the experimental data and corrected for the simulated collection efficiency. The bars show the abundance of each charge state present after initial ionisation from the iodine 2s, $2p_{1/2}$ and $2p_{3/2}$, shown in black, white and grey, respectively.

an M electron after which the relaxation may proceed similarly to the case where the initial hole is created in L3, with an additional M hole. A similar transition for an initial L2 hole is expected to be much less probable for energetic reasons where the energy available only suffice to emit an N electron and the increased radial distance slows down the transition.

5.2 Dissociative double ionisation dynamics in molecules

Small, doubly charged molecules are in constant balance between Coulombic repulsion and attractive Coulombic bonding forces. A small, polyatomic dication AB^{2+} is generally unstable or at least only meta-stable, and these species are expected to predominantly dissociate by charge separation to A^+ + B^+, as this final state is typically lower in energy than the competing AB^{2+} or A + B^{2+} final states. Recently, both theoretical and experimental studies show that some molecules experience specific state-to-state fragmentation in unexpected ways.

By combining a high collection efficiency magnetic bottle electron spectrometer and a mass/charge separating ion spectrometer, the advantages of both techniques can be used simultaneously. The charged final products can be correlated to specific ionisation energies, providing detailed insight into the electronic processes leading to dissociation dynamics associated with specific electronic states. Papers II-V each explore the multi-channel dissociation dynamics upon removal of two valence electrons in small molecules. The central experimental work of this thesis is complemented by high-level ab initio theoretical calculations to explain the isomerisation and dissociation pathways leading to expected and unexpected fragmentation channels.

5.2.1 SO_2

Small molecules like SO_2 have long been used as prototypical systems to study bond-breaking processes. SO_2 has been involved in numerous studies and its pathways leading to sulphur containing compounds are fairly well known [63, 64, 65, 66]. Paper II shows the unusual state-to-state selective behaviour in fragmentation of SO_2 upon double ionisation, and reveals a newly identified mechanism leading to the production of SO^{2+} + O [67]. Paper III investigates and explains a roaming mechanism leading to a new quasi-stable isomer O-O-S^{2+} whose subsequent fragmentation produces the unexpected dissociation channel $S^+ + O_2^+$ [68], which is proposed by us as a new channel of abiotic production of molecular oxygen. A possible pathway to neutralise the oxygen ion via charge exchange involving other atmospheric molecules implies that O_2 can be present in SO_2 rich environments, even in the absence of water.

The SO_2^{2+} species is unstable and upon creation it quickly dissociates. SO_2^{2+} has previously been shown to dissociate via four principal channels [69, 64, 65]:

$$SO_2^{2+} \rightarrow O^+ + SO^+ \tag{5.7}$$

$$SO_2^{2+} \rightarrow O^+ + S^+ + O \tag{5.8}$$

$$SO_2^{2+} \rightarrow O_2^+ + S^+ \tag{5.9}$$

$$SO_2^{2+} \rightarrow O + SO^{2+}. \tag{5.10}$$

The branching ratios of these fragmentation channels are, at first glance, surprising. The expected dominance of the charge separating $O^+ + SO^+$, is true only for the lower energies, where the other channels are energetically inaccessible. In Figure 5.4, the experimental, ion-selected double ionisation spectra for all detectable fragmentation channels, together with a more highly resolved electron-only double ionisation spectrum in black are shown in the top panel. The percentage yields in the bottom panel clearly show that the charge separating channel SO^+ + O^+ is dominant at lower ionisation energies starting at the very onset of double ionisation around 34 eV and

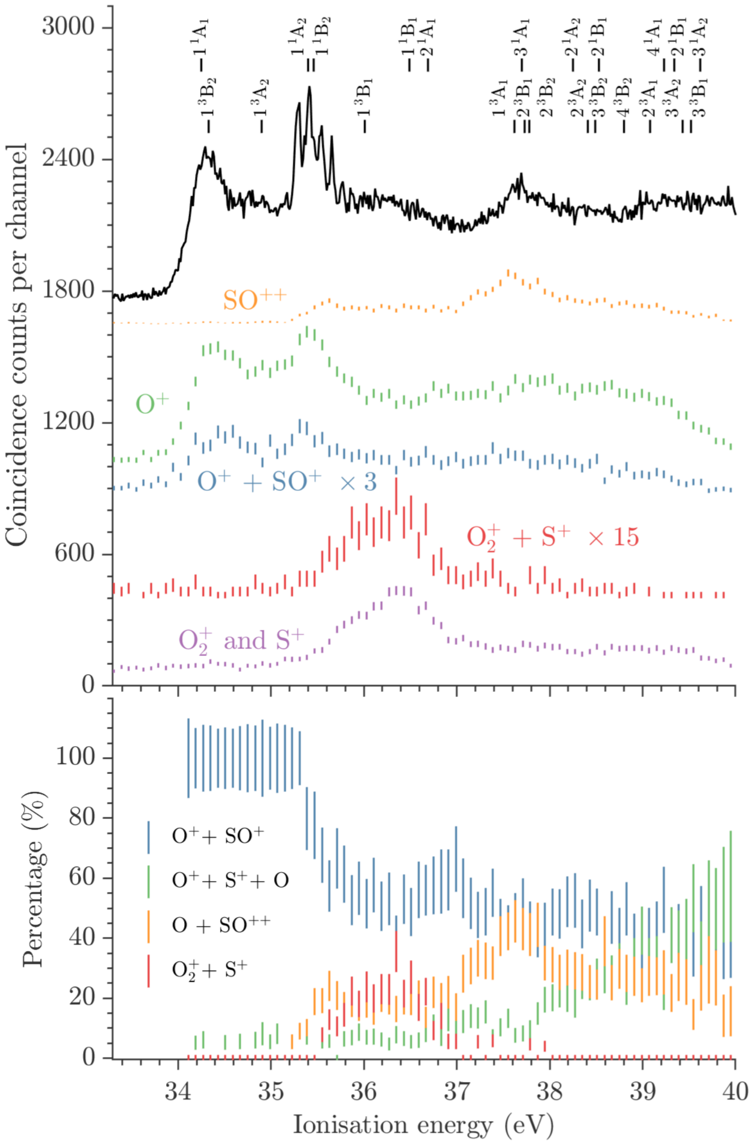

Figure 5.4: Dissociation pathway specific double ionisation spectra of SO_2. The top panel shows spectra of electron pairs correlated with a specific ion or ion pair, compared to an electron only spectrum in black. The combs mark the MRCI/aug-cc-pV(Q+d)Z computed vertical double ionisation energies of SO_2. The bottom panel shows a percentage yield curve for the four detectable dissociation channels.

remains one of the stronger channels over the entire energy range. SO^{2+} + O is found to have two distinct peaks, the first in the 35.2-36 eV range and the second in the 37-38 eV range. The lower energy feature appears to be produced via population of the 1^1A_2 state at 35.3 eV as marked by the vertical combs, which coincides with the thermodynamical threshold at ca 35.46 eV. The vertical combs at the top of Figure 5.4 represent the vertical transitions directly from the ground state within the Franck-Condon region from the neutral molecule. The states are labelled in the $C_{2\nu}$ point group symmetry in accordance with the ground state molecule, regardless of the point group of the dication.

For deeper insight, ab initio calculations of the potential energy surfaces (PESs) along the O-SO distance have been calculated for all excited states in the energy region 33-40 eV above the neutral ground state. This was done in the C_s point group with its two symmetries, A' and A'', for both singlet and triplet electronic states. The calculations show a high density of states which is typically associated with multiple mutual vibronic and spin-orbit interactions. The intersystem crossings will allow pathways leading downwards in energy, converging to the ground state products, which is apparent as the $O^+ + SO^+$ pathway persists over the full range of energies. However, it seems that there is little change to the KER across the range of energies and only a little of the energy can be accommodated by vibrational and rotational energy by SO^+. Thus, much of the excess energy must be that of electronic excitations in the final products, which implies that not only the ground state product is formed.

For the SO^{2+} + O products we refer to the minimal energy paths (MEPs) of the $^1A'$, $^1A''$, $^3A'$ and $^3A''$ states along the O-SO distance, shown by Figure 5.5. The product SO^{2+} (X $^1\Sigma^+$) + O (^3P_g) is suggested to be formed via $^1A''$ or via $^1A'$, which agrees well with the experiment. For $^1A'$ we find a Morse like potential with a plateau very close in energy to the asymptote products, and the other curve, $^1A''$, is slightly more energetic with a barrier of about 0.04 eV. The end products can be reached by intersystem crossings from one of these surfaces to a triplet surface, correlated to the fragmentation products, which are expected to be relatively flat at this bond distance in absence of Coulomb repulsion. At such distances, competitive curve crossings which could lead to $SO^+ + O^+$ are rare. The dissociation limit with the excited oxygen fragment at 37.43 eV is suggested to be reached via 4 $^1A'$. The experimental yield curve for SO^{2+} in Figure 5.4 shows a distinct peak at 35.7 eV suggesting that the vertically accessed 1 $^1A_2$ decays directly to this fragment rather than to the low energy products. This is similarly true for the SO^{2+} production in the IE above 37 eV. In both cases, however, the states are expected to follow the curve crossings to the low energy products.

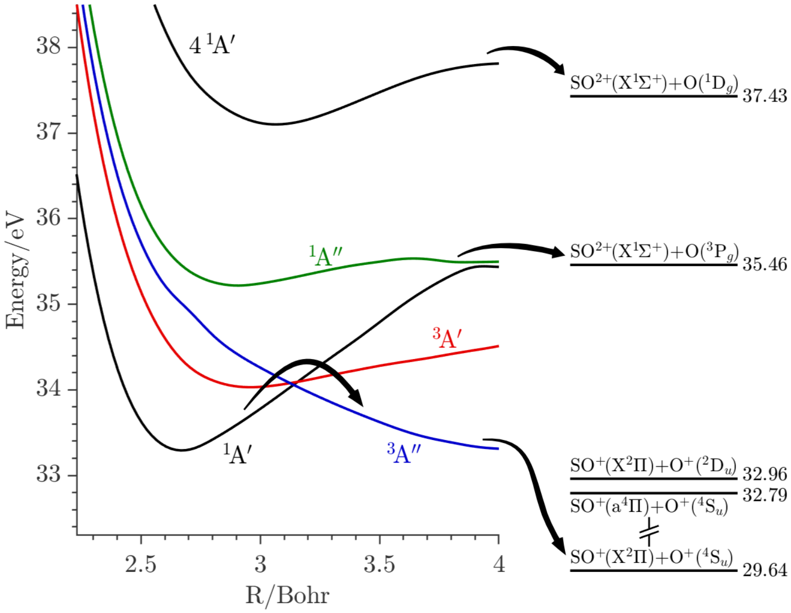

Figure 5.5: Minimal energy path along the SO distance for the $^1A'$, $^1A''$, $^3A'$ and $^3A''$ PESs. These MEPs are deduced from the SO_2^{2+} PESs by looking for the minimal energy for each SO distance along the OSO angles. The 4 $^1A'$ for $R_{SO} = 2.7$ Bohr and $\theta = 120°$ is shown at the top. The dissociation limit fir this ground state is obtained with CCSD(T), and dissociation limits for the excited states are from Refs. [70, 71, 72]. The arrows indicate suggested pathways.

For these states to lead directly to the SO^{2+} + O channel the competitive curve crossings must somehow have been 'turned off' which is unrealistic and highly unlikely.

Thus we propose a new mechanism via a super-excited singly charged state of the parent molecule, SO_2^{+*}, whose bond is elongated prior to auto-ionisation. The clue to such states lie in the observation of the auto-ionising $O^*(3p'\ ^3D) \rightarrow O^+$, providing electrons near 0.5 eV. These low energy electrons are correlated with those from SO^+ over a wide range of energies, shown in Figure 5.6, necessitating the presence of its precursor, SO_2^{+*}, which must also be populated over the same range of energies.

The possibility of such an auto-ionising superexcited state is a reasonable assumption due to the quasi-infinite number of singly charged 2h-1p Rydberg states available that converge onto the dicationic state. The high Rydberg states have a long lifetime [73], and the cores, O^+ and SO^+, will be hardly influenced by the extra electron: they repel each other in the most favourable path of O^+-SO^+ bond breakage. The departing O^+ may capture the Rydberg electron on its way out, creating the observed auto-ionising O^*. In some cases, however, the long-lived Rydberg states may also lead to significant extension of the SO-O bond before producing SO_2^{2+}, which at long bond distance experience PESs well beyond any curve crossings, described earlier, allowing the formation of energetically unfavourable electronic states of SO^{2+}.

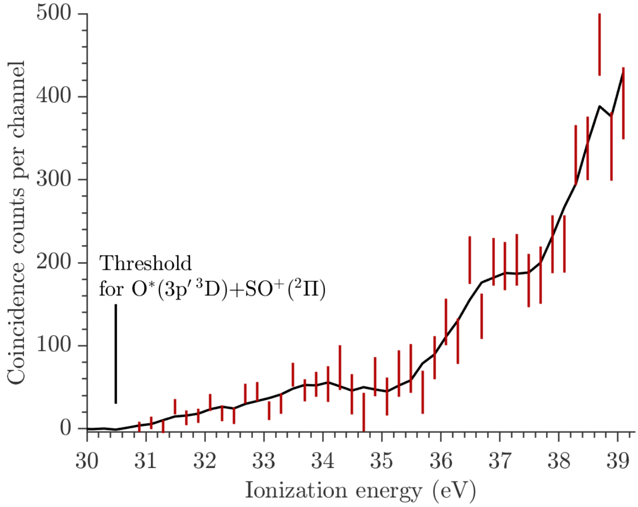

Figure 5.6: Yield for the $O^* \to O^+$ autoionising states leading to electrons at near 0.5 eV kinetic energy over the whole range of ionization energies. Because this is a weak channel and strong underlying SO_2^{2+} formation had to be subtracted, the error bars are large and the smoothed curve is primarily indicative.

The formation of $O_2^+ + S^+$ is not immediately obvious as the sulphur is typically assumed to be located between the two oxygen atoms in the neutral bent configuration. The experimental data in Figure 5.4 show that O_2^+ is produced in considerable yield for ionisation energies from 35.5 eV to 36.8 eV. The most straightforward pathway to imagine is by sulphur being ejected perpendicular to the tangent of the diatomic as they join together to form O_2^+. The PESs cuts corresponding to this geometry are shown in panel A of Figure 5.7, and from these it is clear that the potential energy barrier of about 39 eV is much too high, compared to what is experimentally observed, for O_2^+ to be produced by this mechanism.

The dense manifold of quantum states and spin-orbit crossings motivates an MEP analysis and for SO_2^{2+} this is done by following the valley bottom of the PESs in Jacobi coordinates. In practice, this is achieved by finding the angle θ of minimum energy for each bond distance R, shown by the

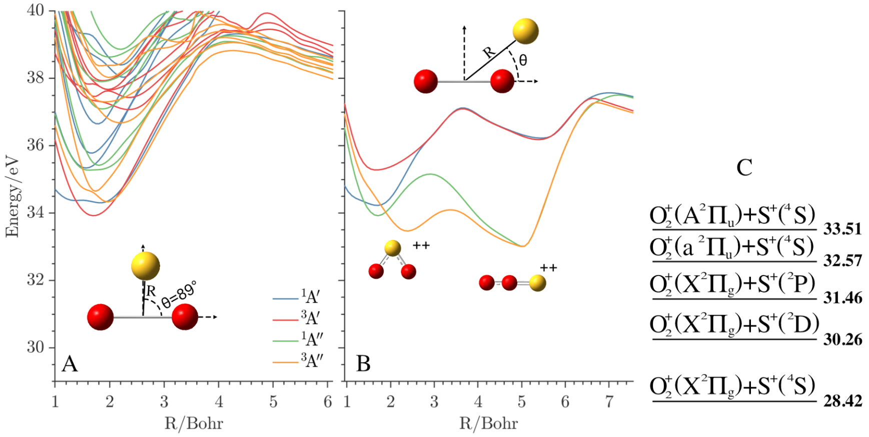

Figure 5.7: Potential energy surface cuts and minimum energy paths of the lowest electronic states of SO_2^{2+} for varying bond distance of S. (A) 1D cuts for the in-plane angle $\theta = 89°$ along the distance R. The O-O bond distance is kept fixed at its value in the neutral SO_2 (X $^1A_1$) ground state equilibrium. (B) Corresponding MEP for bent SO_2^{2+} and O-O-S^{2+}. (C) Thermodynamic thresholds of O_2^++S^+ with reference energy of SO_2 (X $^1A_1$).

illustration at the top of panel B of Figure 5.7. The MEPs, shown in the same panel, revealed that the angle is gradually decreasing from $\theta = 89°$ at $R = 2.5$ Bohr to $\theta = 1°$ at $R = 5$ Bohr, providing a new quasi-linear form O-O-S^{2+}. This new form is reached by roaming, crossing a potential energy barrier at about 34 eV, which is accessible within the range of experimentally observed energies. The new isomer is confirmed by coupled cluster (RCCSD(T)) computations, shown in Figure 5.8 depicting three local minima of SO_2^{2+}.

The potential energy barrier in panel B of Figure 5.7 is still too high to allow the sulphur to be ejected, but by allowing the oxygen atoms to come closer, to within the bond distance of free O_2^+, the situation changes.

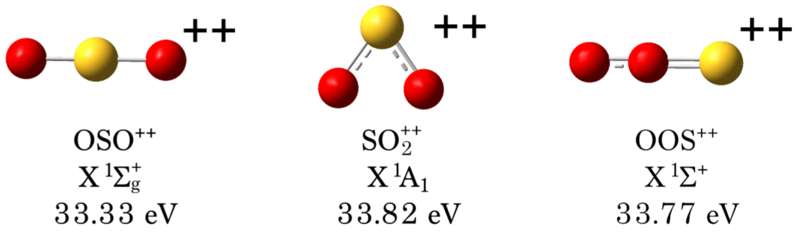

Figure 5.8: Metastable isomers of SO_2^{2+} which are accessible in the energy region where O_2^++S^+ is detectable. The reference energy is that of SO_2 (X $^1A_1$).

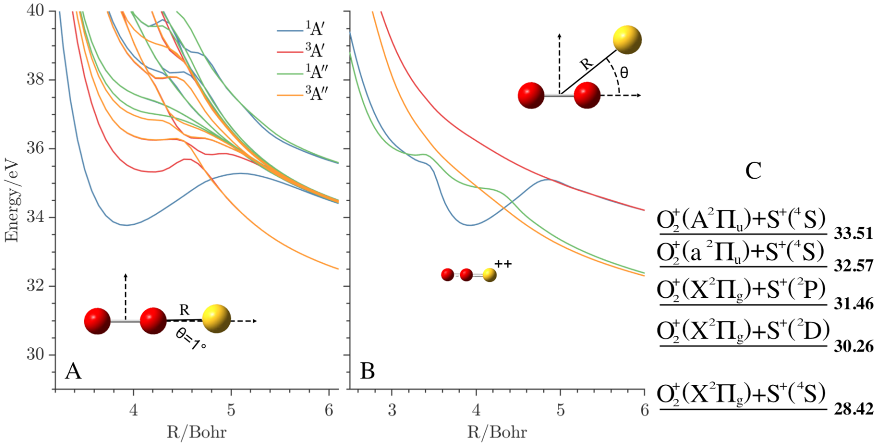

Figure 5.9: Potential energy surface cuts and minimum energy paths of the lowest electronic states of OOS^{2+} for varying bond distance of S. (A) 1D cuts for the in-plane angle $\theta = 1°$ along the distance R. The O_2 bond distance is kept fixed at its value in the neutral O_2 (X $^3\Sigma_g^-$) ground state equilibrium. (B) MEP for OOS^{2+} with a stable $^1A'$ state in a quasi-linear configuration. (C) Thermodynamic thresholds of O_2^++S^+ with reference energy of SO_2 (X $^1A_1$).

Panel A of Figure 5.9 shows all computed excited states as the sulphur is ejected at $\theta = 1°$. The MEPs are shown in panel B of this figure, and both panels show similar potential energy barriers where the plausible lowest pathway is by spin-orbit conversion from $^1A'$ to $^3A''$ with a barrier around 34.5 eV, which agrees well with the experimental appearance energy (AE). Panel C in both figures 5.7 and 5.9 show the dissociation limit products at their computed energies with reference to the neutral ground state of SO_2 (X $^1A_1$). By going to the lowest state from the barrier crossing, a KER of about 6 eV is found, whereas the experiment suggest a KER of 4.7 ± 0.3 eV. The excess energy may be explained by energy converting to rotational or vibrational energy of the O_2^+ fragment. Another explanation could be that the final product ends not in the ground state but instead in the excited S^+ (^2D) state, located 1.8 eV above the ground state.

5.2.2 OCS

Paper IV investigates the dissociation of OCS^{2+} ions formed by the photoionisation of neutral OCS at 40.81 eV photon energy, again utilising the electron-ion apparatus for detecting electrons and ions in coincidence [74]. Previous work has suggested the experimental AE of the fragmentation channel CO^+ + S^+ to be much higher than theoretical predictions.

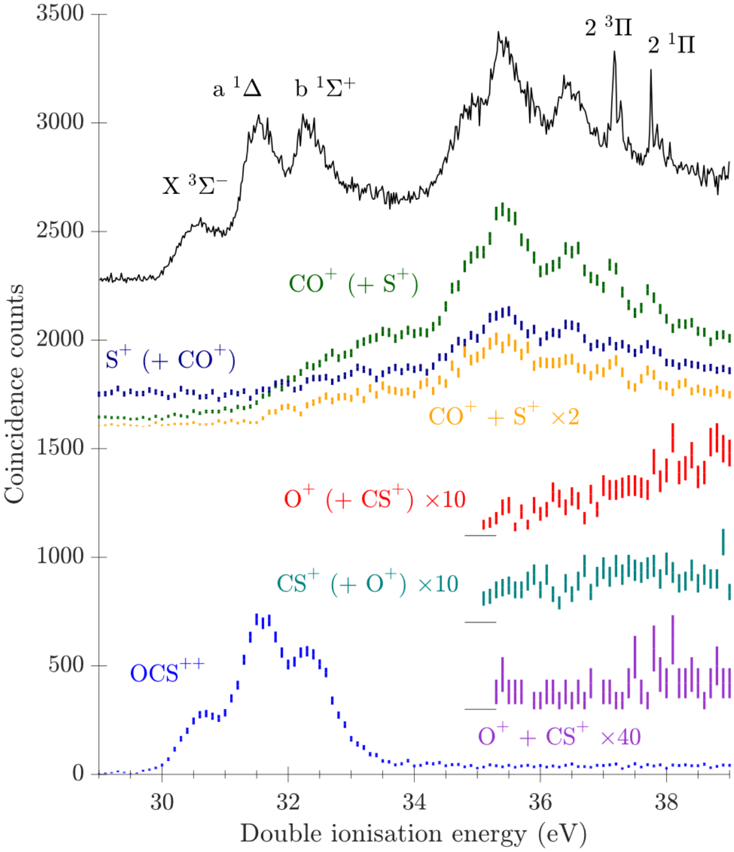

Figure 5.10: Double photoionisation spectra of OCS from threefold and fourfold coincidences with the parent ion and fragment ions formed by photoionisation at $h\nu = 40.81$ eV. A more highly resolved electron only spectrum of OCS^{2+} taken at the same photon energy is shown by the solid black line. The threefold coincidence labels include the implied second ion in parentheses, supported by the full fourfold coincidences explicitly stating both ions. The counts in each spectra are scaled by the factors denoted, and the lines correspond to 2σ error bars.

In addition, the theoretical pathways via OCS^{2+} did not fully account for the experimental observations and energetics, such as KERs and AE. With our investigation, we complement the work of Brites et al. [75] by new experimental findings which resolves the onset discrepancy, in addition to providing new possible pathways with intramolecular isomerisation via COS^{2+}. Such bond rearrangement is evidenced by the pretty weak presence of the decay channel producing C$^+$ + SO$^+$, which has been seen in previous experiments using lasers [76]. This fragment pair is present but only amounts to 0.05% of the threefold coincidences, despite the fact that the thermodynamic limit for its formation at 30.4 eV is well below the 40.81 eV photon energy, even allowing for substantial KER from passing a potential barrier.

Figure 5.10 shows the yield curves for the different threefold and fourfold coincidences on the double ionisation scale. The parent dication is found at the lowest ionisation energy with an AE of 30 eV, and this final state remains dominant up to 32 eV, which is not surprising since it is reached directly in the Franck-Condon region by vertical transition. The fragmentation channels observed are the dominant $CO^+ + S^+$, and the much weaker $CS^+ + O^+$ and to some extent $SO^+ + C^+$ (not included in Figure 5.10).

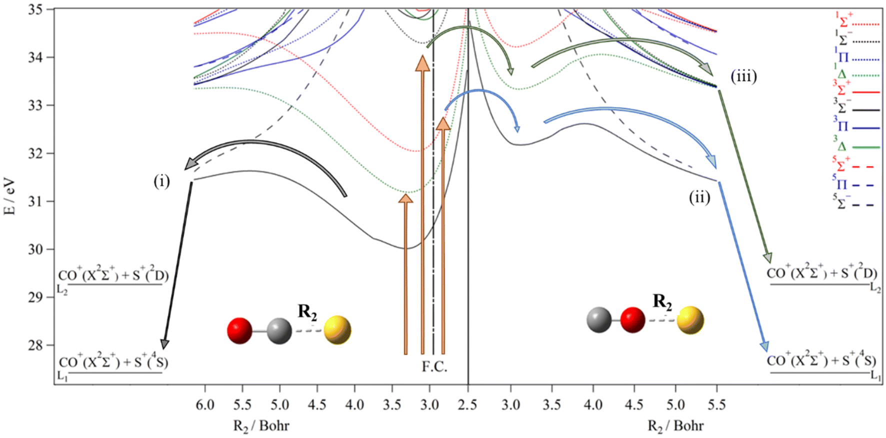

Figure 5.11: MRCI/aug-cc-pV(Q+d)Z potential energy curves of the lowest electronic states of OCS^{2+} (left) and COS^{2+} (right). F.C. denotes the Franck-Condon zone accessed from the ground state of OCS. The reference energy is that of the OCS ($X\ ^1\Sigma^+$) neutral ground state.

Previous experimental work have estimated the onset of $CO^+ + S^+$ to 34 eV with an estimated KER of 5.5 eV [75]. The thermodynamical threshold of 27.5 eV with the estimated KER would infer an AE at $27.5 + 5.5 = 33$ eV, with some additional rotational and vibrational energy. This is higher than the computed AE of 31.6 eV with accompanied KER of 4.17 eV, shown as pathway (i) in Figure 5.11. In fact, our experimental data, shown in Figure 5.10, show this AE as the onset at 31.7 ± 0.4 eV, much weaker compared to the strong rise at 34.1 ± 0.5 eV, coinciding with the previous measurements. This lowest onset is suggested to be weak as the initial state population at this energy is predominantly to the $a^1\Delta$ and $b^1\Sigma^+$ states of OCS^{2+}. This implies that the old KER is estimated too high, and thus we split the data into two energy regions. Figure 5.12 shows the time difference

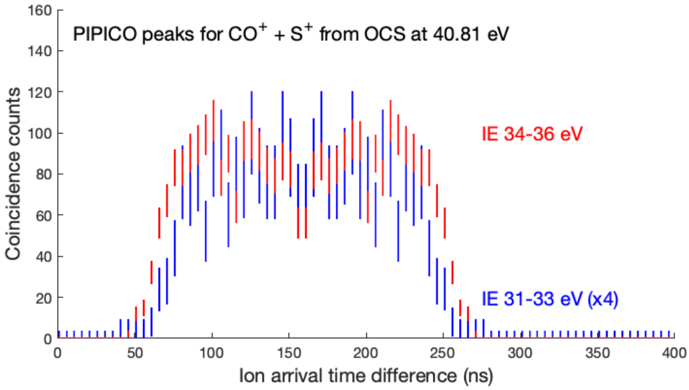

Figure 5.12: Arrival-time difference peaks for CO$^+$+ S$^+$ ion pairs coincident with photoelectron pairs from double ionisation in the energy ranges shown. The peaks have been artificially symmetrized about the time difference for thermal ions, using the later half of the peak.

between the two arriving ions for selected ionisation energy ranges of 31-33 eV and 34-36 eV, respectively. Because the mass numbers for the two ions are relatively close, and the strong OCS^{2+} lie in between, only the latter part of the peak is free from interfering signals. Thus, the peaks are symmetrized by the latter half of the peak, centred around thermal ions. To the extent that the limited statistics allow, this gives the indication that the lower energy process leads to noticeably less kinetic energy than the high energy process. It is not possible to accurately determine the KERs. However, it can be inferred from the thermodynamical limits together with experimental appearance energies. The lower energy region is expected to have a KER $\leq$ 4.2 eV and the higher energy region a KER $\leq$ 6.5 eV.

For the higher energy regions we identify pathways via newly identified metastable states of COS^{2+} which can be reached within this ionisation energy region as shown in Figure 5.13. RCCSD(T) computations [74] reveal that the most stable form is OCS^{2+} at 30.01 eV with respect to neutral OCS, and that COS^{2+} state is about 2 eV higher at 32.03 eV. The COS^{2+} appear lower in energy in Figure 5.13 since the O-S bond distance is too long. As shown in Figure 5.13, the metastable isomer can be reached by crossing the first barrier at 2.25 eV above the OCS^{2+} geometry. With respect to the neutral ground sate of OCS, the energy required to reach COS^{2+} is 32.26, 33.98 or 34.63 eV, depending on whether double ionisation populates the OCS^{2+} (X $^3\Sigma^-$), (1 $^1\Delta$) or (1 $^1\Sigma^+$) states, respectively.

A summary of the newly identified pathways via both OCS^{2+} and COS^{2+}, as denoted (i), (ii) and (iii), are shown in Figure 5.11. Pathway (i) has an

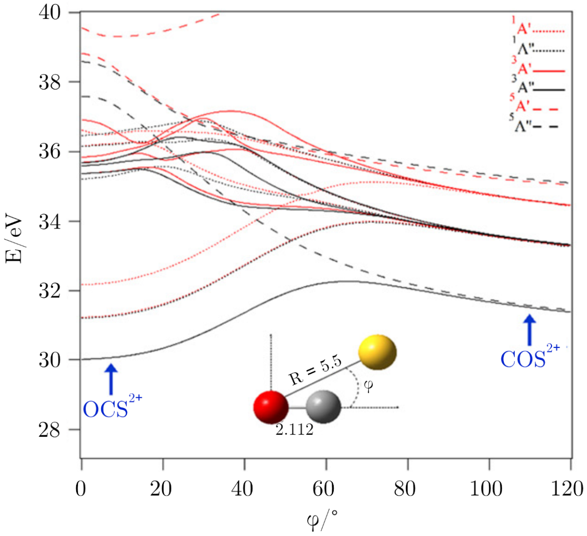

Figure 5.13: MRCI/aug-cc-pV(Q+d)Z 1D cuts of the PESs of the electronic states of the OCS^{2+} system along its bending coordinate ϕ. The reference energy is that of the OCS (X $^1\Sigma^+$) neutral ground state.

AE of 31.6 eV, lower than required for isomerisation and thus this pathway is only present as the black arrow via OCS^{2+}. Its KER is computed to be 4.17 eV, which is in good agreement with the lower KER expected from the experiment. Pathway (ii) has an AE of 32.62 eV and leads to the same final state as (i) but via COS^{2+}, and thus appears at higher energy with a higher accompanied KER. Pathway (iii) via the COS^{2+} ($^1\Delta$) state has an AE of 34.06 eV with an accompanied KER of 4.79 eV. A competing mechanism leading to the same final state via the $^1\Delta$ state in OCS^{2+} has a lower AE of 33.4 eV, and a KER of 4.1 eV, which is ruled out by the present experiment. Additionally, population of the OCS $b^1\Sigma^+$ state leading to the $^3\Pi$ state by spin-orbit conversion has its crossing at about 34 eV, coinciding with the energy of pathway (iii). However, this channel may be ruled out by making use of the results of the laser experiments where Zhao et al. [76] demonstrated that the angular distribution of the KERs of CO^+ + S^+ and SO^+ + C^+ exhibit similar behaviour, indicating the same type of process, where the latter necessarily involves bond rearrangement. In addition, Endo et al. [77] revealed a phase shift of 270° between the high energy and low energy KER subchannels, which they attribute to a population transfer between electronic states. This implies that different mechanisms are at play in the two KER regions, suggesting that the higher energy process is in fact likely to be due to bond rearrangement.

5.2.3 HNCS

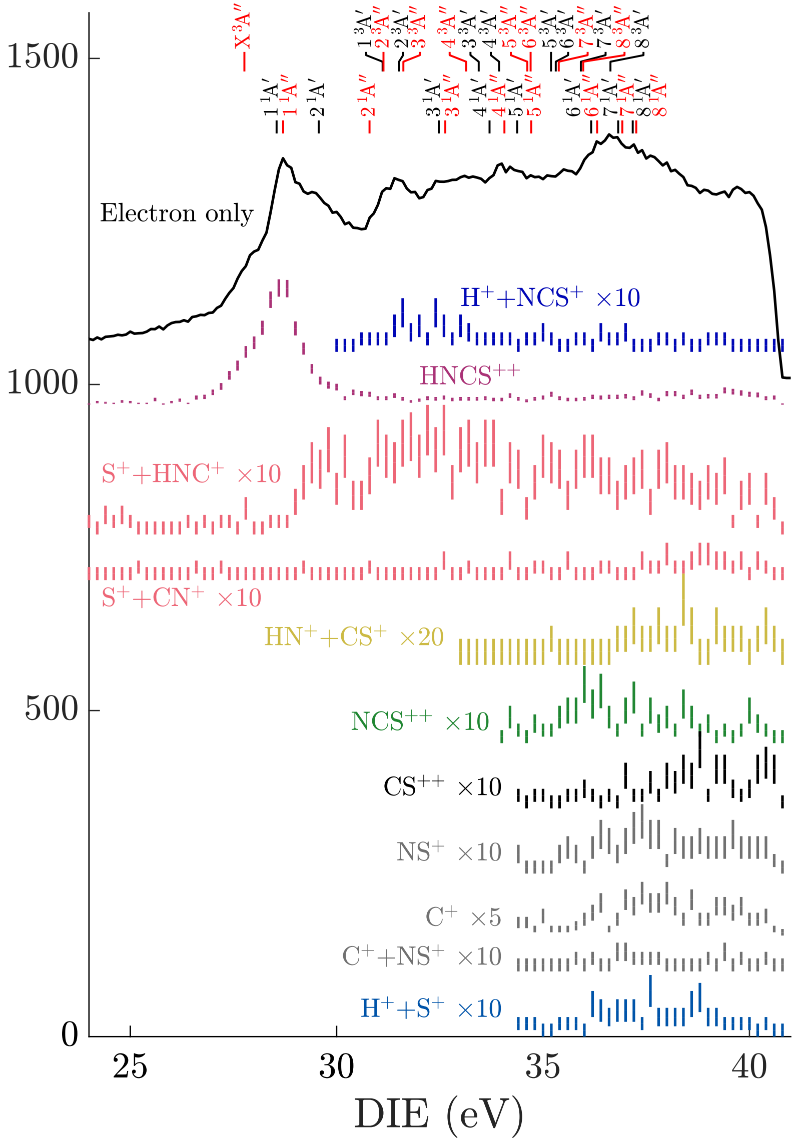

Figure 5.14: Ion channel specific double ionisation electron pair spectra of HNCS using 40.81 eV photons. In addition, an electron only double ionisation electron spectrum is shown at the top as a solid black curve. The remaining spectra are presented in error bars selected on 1 or 2 ions, where the ions used for the selection are explicitly stated. The curves are scaled for visibility with a statistical error $\sqrt{N}$, where zero counts are artificially given error=1.

Isothiocyanic acid (HNCS) has been irradiated by photons of 40.81 eV and recorded using again the in-line electron-ion coincidence apparatus, described in Section 3.5. The double ionisation spectra are shown as projections of threefold and fourfold coincidences for the detectable decay channels in Figure 5.14, together with an electron only spectrum that comprises all mechanisms shown as a solid black curve. At this photon energy, the doubly charged parent ion HNCS^{2+} is most dominantly formed, starting at 27.1 eV, with the ground state HNCS^{2+}(X ^{3}A$''$). Here, we will continue to discuss the most dominant fragmentation channels, focusing primarily on the ones reached simply by elongating one bond to infinity. The channels which fully dissociate or require bond rearrangement are not discussed.

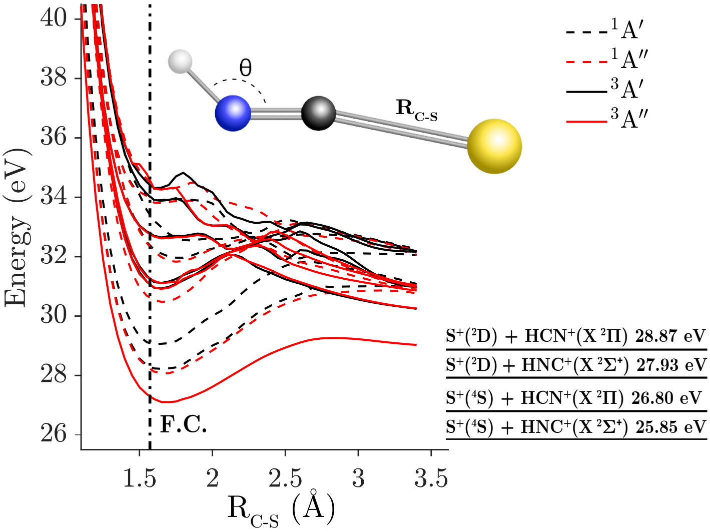

Figure 5.15: The curves on the left side show PES cuts elongating the C-S bond in the HNCS dication, at the lowest energy θ. The remaining bonds and angle are kept fixed at their values in the neutral ground state of HNCS (X ^{1}A$'$). The right side shows thermodynamic thresholds of HNC$^+$/HCN$^+$+S$^+$ with reference energy of the neutral ground state of HNCS (X ^{1}A$'$).

The most dominant decay channel produces HNC$^+$ + S$^+$, which is a two-body fragmentation by breaking the C-S bond. As shown in Figure 5.14 this channel has an AE of 29.1 ± 0.2 eV, and the ion-ion coincidence map yields an estimate for the overall KER of 3.2 eV. The KER increases for higher ionisation energies, which is seen by investigating the KER for a set of small ionisation energy intervals. The regions are selected based on the HNC$^+$ + S$^+$ four-fold peak, shown in Figure 5.14, with ionisation energy regions of 29.0 − 30.4 eV, 30.8 − 34.4 eV and 30.8 − 34.4 eV, and with KERs of 2.5 eV, 2.8 eV and 3.4 eV, respectively. The PESs for this decay channel are shown in Figure 5.15 by elongating the C-S bond for all angles ∠ H-N-C. In addition, the dissociation limits for $HNC^+/HCN^+ + S^+$ are shown. The lowest state is the X $^3A''$ whose curve resembles a Morse potential, and a barrier at 29.26 eV, which is in good agreement with the experimental AE. Additionally, the KER by going via the X $^3A''$ state to the lowest dissociation limit is estimated to 3.4 eV, about 1 eV higher than the experiment, suggesting that the fragment ion yields significant internal rotational and/or vibrational energy. Another explanation may be that isomerisation takes place to form the HCN^+ fragment, about 1 eV above the HNC^+ ground state.

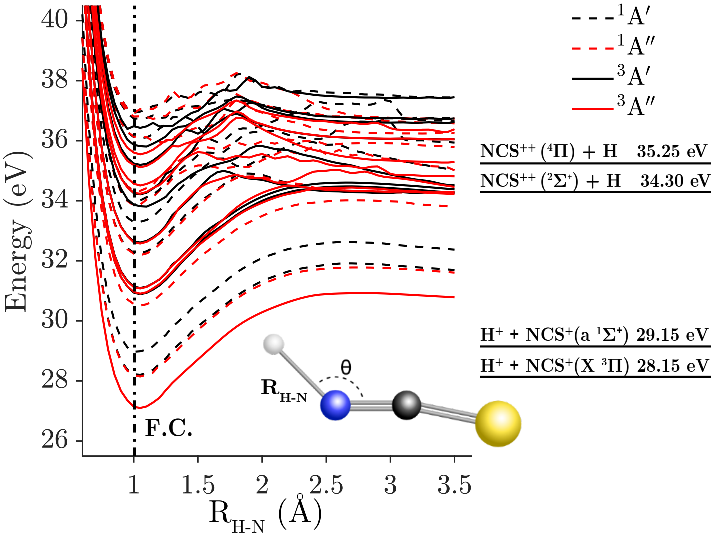

Figure 5.16: The curves on the left side show PES cuts elongating the H-N bond in the HNCS dication, at the lowest energy θ. The remaining bonds and angle are kept fixed at their values in the neutral ground state of HNCS (X $^1A'$). The right side shows thermodynamic thresholds of H^++NCS^+ and H+NCS^{2+} with reference energy of the neutral ground state of HNCS (X $^1A'$).

Figure 5.16 shows the elongation of the H-N bond, reaching the final states of $H^+ + NCS^+$ and $H + NCS^{2+}$. The first few PESs have the form of a Morse-potential with the lowest being the X $^3A''$ state with a potential barrier at 30.93 eV, followed by the degenerate states $^1A'$ and $^1A''$ with a barrier at 31.8 eV. The experimental onset is at 31.2 ± 0.5 eV, which agree reasonably with both the ground state triplet and the degenerate singlets. The most plausible route is via the singlet states as population of X $^3A''$ is expected to primarily go to the most dominant decay channel. The very light H^+ is highly affected by experimental conditions which implies a considerable uncertainty in determining the KER from the ion-ion coincidence map, where it is estimated to be less than 4 eV. The lowest theoretical KER from X ^{3}A$''$ to the lowest asymptote is calculated to be 2.78 eV compared to that of the ^{1}A$'$ and ^{1}A$''$ at 3.65 eV. Both of which, considering the large uncertainty in the experimental value, agree reasonably. The figure also shows the pathway to the charge retaining final state H + NCS^{2+}, which is present, albeit very weakly, in the experimental data. The PESs show a high density of states at the energy of the limit (34.3 eV), suggesting a very low KER. This is supported by the 0 eV KER found by the ion TOF curve where the width of the NCS^{2+} peak is comparable to its much stronger neighbour and parent HNCS^{2+}, which inherently have 0 eV KER. The experimental onset appears at an energy of 35.0 ± 0.4 eV which is higher than the dissociation limit of H + NCS^{2+} ($^2\Sigma^+$) state, suggesting a KER of some 0.5 eV, or population of the H + NCS^{2+} ($^4\Pi$) state.

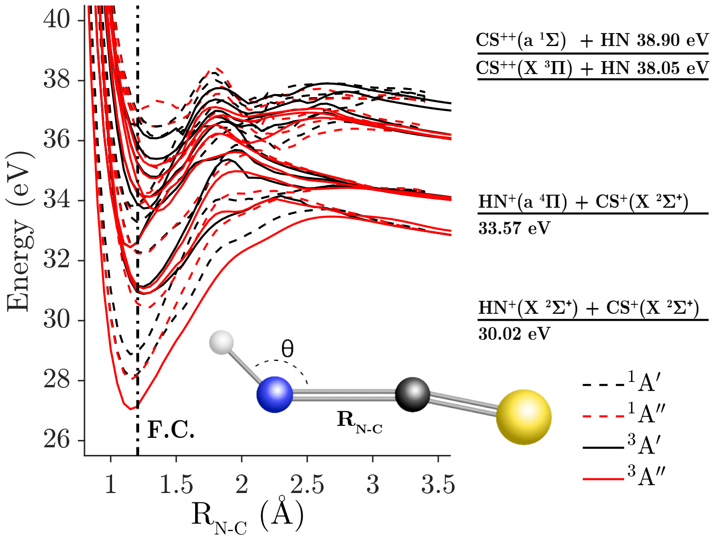

Figure 5.17: The curves on the left side show the PES cuts elongating the N-C bond in the HNCS dication, at the lowest energy θ. The remaining bonds and angle are kept fixed at their values in the neutral ground state of HNCS (X ^{1}A$'$). The right side shows thermodynamic thresholds of HN$^+$+CS$^+$ and HN+CS^{2+} with reference energy of the neutral ground state of HNCS (X ^{1}A$'$).

Figure 5.17 shows the PES cuts found by elongating the central N-C bond. The experimental data in Figure 5.14 has an AE at 36.9 ± 1 eV whereas the lowest numerical value comes at 33.47 eV as the top of the X ^{3}A$''$ barrier. The experimental KER is estimated to 2 eV which is well below compared to what is obtained by reaching the ground state products from

X ^{3}A$''$. Instead, the suggested pathway is via one of the many surfaces in the energy region of 35.0-36.8 eV, all converging to the excited final product HN$^+$ (a $^4\Pi$) + CS$^+$ (X $^2\Sigma^+$) with a reasonable KER that matches the 2 eV found in the experiment. In this energy region, significant bending into the cis or trans-configurations are required to reach curve crossings leading to states that adiabatically reach the lowest asymptote. Thus it may be possible to produce excited fragments in this way, although, it will require more calculations to continue this idea, or to find other possible explanations.

5.3 Femtosecond lifetimes in sequential decay

The shape of an ion-ion coincidence island carries rich information about the underlying decay mechanism(s). The ions' total flight times scale with $\sqrt{m/q}$ and reveal which ionic species are in a particular island. The underlying mechanism is identified by its slope in addition to comparing its shape to those in Figure 4.10 from Chapter 4. Previous work by Eland [40, 41] provides good explanations for the mechanisms leading to islands with shapes (A)-(D) in Figure 4.10, in addition to assuming the bow-tie shape to be part of the immediate explosion. Paper VI suggests that the previous prototypes were insufficient to explain the full range of island shapes encountered in practice, and extends previous works to explain the additional island shapes (E) and (F). We show by simple Monte-Carlo type simulations that slopes deviating from the expected limit, and the twisted and bow tie-shaped islands can form from the sequential decay:

$$\mathrm{ABC}^{++} \rightarrow \mathrm{A}^{+} + \mathrm{BC}^{+} \rightarrow \mathrm{A}^{+} + \mathrm{B}^{+} + \mathrm{C} \tag{5.11}$$

with short secondary decay lifetimes in the femtosecond region.

Perflouro-propyl iodide, C_3F_7I, is an interesting case as the two charges can go in three ways when breaking the same bonds CF_3-C_2F_4-I, and its two isomers produces all of the sequential decay forms discussed in this thesis. The two isomers are n-C_3F_7I and iso-C_3F_7I, with the iodine located at the end and in the middle of the molecule, respectively. Both forms can break into the same three fragments I, C_2F_4 and CF_3, with masses 127, 100 and 69, respectively. In the n-form, the iodine is bound in series with the carbon atoms, directly attached to the centre mass 100 moiety. In the iso-form the iodine switches place with one fluorine atom attached to the centre carbon atom and thus it is still attached to the larger mass 100 moiety. This means that even though the iodine is placed in the middle it can only fragment in steps where it is attached to the C_2F_4, at a different angle to the molecular axis.

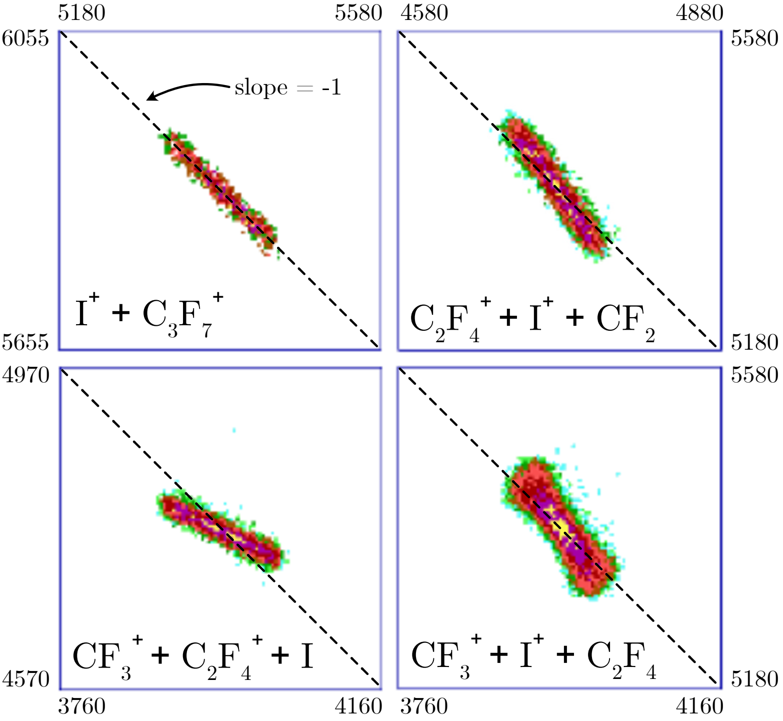

Figure 5.18: Experimental ion-ion coincidence islands of n-C_3F_7I.

Table 5.1: Comparison of the relative intensities and slopes for the three main islands for perfluoro-propyl and iso-perfluoro-propyl iodide, the former at three different photon energies.

Product masses	$-m_B/m_{BC}$ or $-m_{BC}/m_B$	Relative intensity and slope n-C_3F_7I						iso-C_3F_7I	
A + B + C		at 48 eV		at 41 eV		26.8-31.7 eV		at 41 eV	
$I^+ + C_2F_4 + CF_3^+$	-2.45, (-0.56)	100	-1.4	100	-1.3	100	-1.5	100	-1.95
$I + C_2F_4^+ + CF_3^+$	-0.44	16	-0.48	49	-0.49	78	-0.46	9	-0.48
$I^+ + C_2F_4^+ + CF_3$	-1.69	62	-1.4	43	-1.4	3	-1.33	51	-1.4

Figure 5.18 shows the experimental data of the three pathways in the n-form, in comparison to the two-body dissociation at 41 eV photon energy. In addition, the left panel of Figure 5.20 shows the most intense channel, $I^+ + C_2F_4 + CF_3^+$, from the experimental data of the iso-form, which shows a twisted shape. The other decay channels of the iso-form are referenced, but not shown in separate figures as they share similar slope and shape of

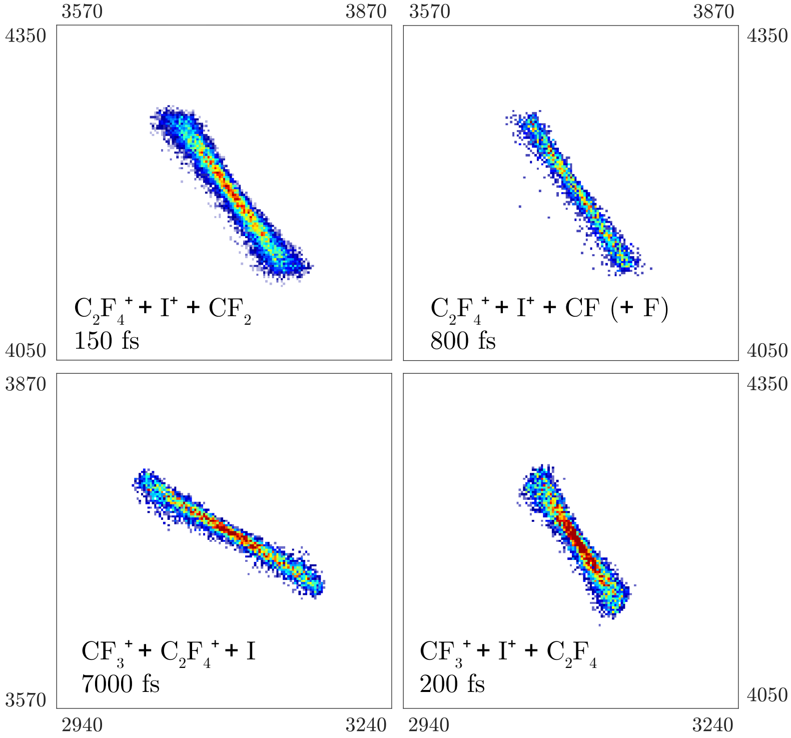

Figure 5.19: Simulated ion-ion coincidence islands of n-C_3F_7I.

the n-form. The slopes for both isomers are listed in Table 5.1 at several photon energies, in comparison to the expected limits and experimental yield. The photon energies of 41 eV and 48 eV are provided by the emission lines of helium whereas energies in the range 26.8-31.7 eV are from several simultaneous emission lines of neon. The slopes are compared to simulations shown in figures 5.19 and 5.20.

The upper right panel of Figure 5.18 shows the sequential decay $C_2F_7^+(169) \rightarrow C_2F_4^+(100) + CF_3(69)$ whose slope is consistent in both isomers at -1.4. The reaction, which disappears at the lowest energy, has an AE 25 eV + KER and a measured onset at 31 eV. The alternative four-body decay has an estimated AE at 31.5 eV + KER. If it is a three-body decay, it must be fast since the slope deviates significantly from the expected slope -1.69. To match the slope, simulations predict a lifetime of 150 fs, as shown in the upper left panel of Figure 5.19. However, the shape of the island is a twisted bow-tie as a result of the fast secondary dissociation. The lifetimes are distributed around 150 fs and the reactions occurring faster come at a closer distance in the Coulomb field, which here results in a higher total KERs.

The fact it diminishes at low energy suggests the more probable explanation with the initial loss of a fluorine atom prior to the initial fragmentation. The loss implies a final mass 50, rather than 69, and the secondary decay $C_3F_6^+(150) \rightarrow C_2F_4^+(100) + CF_2(50)$ has an expected slope of -1.5. This value is much closer to the experimentally measured value, suggesting a longer lifetime, which is supported by the simulated island in the upper right panel of Figure 5.19 using 800 fs and zero secondary KER.

Of the three main reactions, only I + $C_2F_4^+$ + CF_3^+, shown in the lower left panel of Figure 5.18, is necessarily a three-body reaction with sequential decay $IC_2F_4^+(227) \rightarrow I(127) + C_2F_4^+(100)$. This comes at the expected slope, and thus a long lifetime must be suspected. The prediction is confirmed by simulations, shown in the lower left panel of Figure 5.19, which suggests a lifetime of 7000 fs with zero secondary KER.

The lower right panel of 5.18 shows the sequential decay leading to $I^+ + C_2F_4 + CF_3^+$ with a distinct bow-tie shape. Here, two different pathway mechanisms are possible, via $IC_2F_4^+(227)$ and $C_3F_7^+(169)$, however only the latter is present. The former process would take some of the momentum from iodine, giving a slope between -1 and 0. $C_3F_7^+(169) \rightarrow C_2F_4(100) + CF_3^+(69)$ appears strongly at all photon energies, and a slope of -1.4, compared to the expected slope of -2.45, indicates the reaction must be fast. Because it appears strongly at the lowest energy there is good reason to assume that it is a three-body decay and the AE is estimated at 23.8 eV + KER [78], whereas the lowest four-body AE comes at 32 eV + KER. Simulations, shown in the lower right panel of Figure 5.19, assume a lifetime of 200 fs with zero secondary KER. The distinct bow-tie shape arises from the spread of the monocation lifetimes. The timing of the secondary dissociation places the fragment BC^+ at a distinct point in the Coulomb field of A^+. The

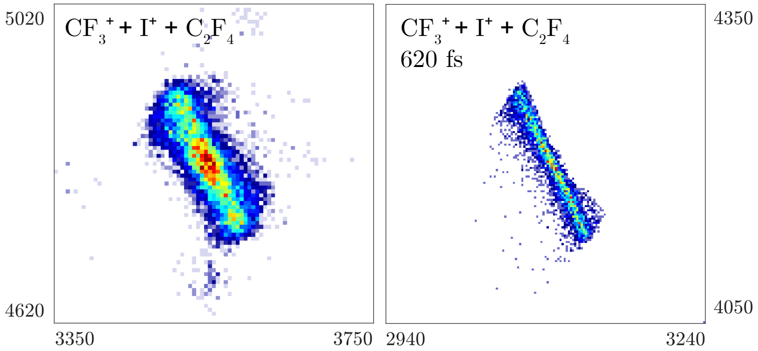

Figure 5.20: Experimental (left) and simulated (right) ion-ion coincidence islands of iso-C_3F_7I.

dissociation time is distributed about its lifetime and the shorter lifetimes yield a slope closer to -1, and a longer lifetime yield a slope trending to the dissociation limit, $-\mathrm{m_B}/\mathrm{m_{BC}}$. All slopes go through the island centre and thus the spread of lifetimes give broadened wings: a bow-tie. The symmetrical form occurs in particular at lifetimes where the deviations of the secondary dissociation in the Coulomb field generate similar total KERs (compared to the 150 fs lifetime scenario from before).

In contrast, the analogous reaction in the iso-form, leading to $\mathrm{I}^+ + \mathrm{C_2F_4} + \mathrm{CF_3^+}$, is shown in Figure 5.20 (experiment (left panel) and theory (right panel)). The experimental island shows a strong centre slope at -1.95, steeper than the n-form, with a weaker, less steep, outer slope. The strong centre slope is closer to the expected slope and a longer lifetime is suspected, confirmed by simulations at 620 fs. A systematic study was done by simulating this reaction for increasing lifetimes. At 20 fs (almost immediate) a slope of -1.1 is found with a slight bow-tie shape. Increasing to 320 fs shows a clear bow-tie shape at a slope of -1.78 which diminishes by increasing further to 620 fs at the twisted form. The twist persists until about 1000 fs whereafter it shifts to a regular bar at lifetimes around 2000 fs, with a slope of -2.2, eventually reaching the limiting slope of -2.45.

CHAPTER 6

Conclusions and outlook

6.1 Conclusions

This thesis has explored the intricate phenomena of dissociative multi-ionisation in gas-phase molecules through a series of detailed experimental and theoretical studies. The experimental investigations have been carried out using a versatile time-of-flight magnetic bottle electron spectrometer together with an ion mass time-of-flight spectrometer.

In paper I of this thesis a standalone 50 cm long ion-ion coincidence apparatus was used to capture the Coulomb explosion of CD_3I at tender X-ray photon energies provided by the storage ring SOLEIL. The photon energies were tuned to be above the $2p_{3/2}$, $2p_{1/2}$ and 2s edges of iodine, i.e. $h\nu = 4660$ eV, 4950 eV and 5290 eV, respectively. These initial core holes lead to efficient Auger-Meitner cascades, creating cumulative charge states up to 16. The charge state abundance for each initially created hole is obtained by subtracting the different datasets (using an additional dataset at 4600 eV) taking into account the total cross section for photoabsorption for each subshell where extrapolation estimated the partial cross sections at the different photon energies. The core hole creation of 2s leads to shifts to higher charge states, indicating a rapid Coster-Kronig decay, transferring the hole to 2p, with an additional hole in the n=3 shell.

In papers II-V the molecules SO_2, OCS and HNCS were investigated by photoelectron-photoion coincidence measurements using the helium emission line at 40.81 eV. These measurements resulted in ion mass-selected double ionisation spectra for all detectable dissociation pathways. Some of the fragmentation pathways that were previously not fully understood were investigated in greater detail.

In paper II an explanation is presented for the charge-retaining pathway of SO_2^{2+} leading to SO^{2+} + O. To avoid the intersystem curve crossings, leading to the ground state products, the suggested pathway is by the initial photoionisation reaching a superexcited autoionising singly charged 2h-1p Rydberg state. The two holes repel each other similar to the doubly charged molecule, and as the moieties separate, at long bond distance, the superexcited cation decays to a doubly charged state. At these bond distances the lack of potential energy curve crossings, that would otherwise lead to SO^+ + O^+, allow for state-selective fragmentation to SO^{2+} + O.

In paper III the pathway producing molecular oxygen from double ionisation of SO_2 was identified in the form of a roaming mechanism leading to the linear O-O-S^{2+} configuration prior to the two-body decay to O_2^+ + S^+. Subsequently, O_2^+ is suggested to exchange charge in exothermic reactions in atmospheric environments, producing neutral O_2.

In paper IV new pathways are explained where OCS^{2+} is shown to rearrange its bond structure to COS^{2+}. This can occur in certain energy regions upon double photoionisation, evidenced by the weak pathway leading to C^+ + OS^+ which would be unobtainable without such rearrangement. Comparison to theory suggested that the fragment CO^+ + S^+ is possible in two principal ways: directly via OCS^{2+}, or via the meta-stable COS^{2+}. In the low energy region, 31-33 eV, the ground state products are populated via OCS^{2+}, where the energy is too low for bond rearrangement. In the energy region 34-36 eV, new pathways, where the ground state and first excited state of CO^+ + S^+ are populated via COS^{2+} with about 5.5 eV kinetic energy release, agree with the experiment. The new mechanisms via COS^{2+} resolves the discrepancies from previous works where the appearance energies and kinetic energy releases of the theoretically allowed pathways did not agree with the experimental data.

In paper V the decay channels with a single bond break in doubly ionised HNCS were studied and compared with numerical computations. The most dominant decay channel S^+ + HNC^+ is produced with an AE 29.1 ± 0.2 eV, which agrees well with crossing the potential energy barrier of the X $^3A''$ state. The much weaker fragmentation channel producing H^+ + NCS^+ had an AE of 31.2 ± 0.5, which was assumed to form via 1 $^1A'$ or 1 $^1A''$, and population of the $^3A''$ state then favours the dominant decay channel. When the centre bond was broken, leading to HN^+ + CS^+, the experimental onset of 36.9 ± 1 eV is much higher than the lowest theoretical AE at 33.47 eV. The likely pathway involves instead one of the many surfaces in the energy region 35-36.8 eV, with relatively few curve crossings in the linear quasi-linear structure, to reach the excited state fragmentation HN^+ (a $^4\Pi$) + CS^+(X $^2\Sigma$).

In paper VI the ion-ion coincidence island peak shapes of sequential three-body fragmentation in dicationic systems were investigated and characterised. Dissociation channels with coincidence ion island slopes that deviate from the expected limiting slopes were simulated. The simulations show that a sequential decay with femtosecond lifetimes affect the repelling ions such that the expected slope gets closer to a slope of -1. As the ion ABC^{++} initially separate to A^+ + BC^+ and within a few hundred femtoseconds separate to B^+ + C, the second fragmentation occurs within the effective Coulomb range of A^+. Experimental shapes that were previously unexplained, showing up as bow-tie and twisted shapes, are attributed to such femtosecond lifetimes. Systematic simulations for different lifetimes showed that shorter lifetimes look more like the instantaneous explosion, the intermediate lifetimes (200 fs for perflouro-propyl iodide) give the bow-tie shape and longer lifetimes (620 fs for iso-perflouro-propyl iodide) give a twisted form. At even longer lifetimes (2000 fs) the simple bar converges to the expected slope.

6.2 Outlook

Single photon ionisation experiments of molecules give insight into the chemical processes in low density matter areas such as the interstellar or atmospherical environments where the light intensity is low but photon energies can be relatively high. By studying these molecules in a controlled laboratory environment, specific processes can be probed and carefully analysed and compared to state-of-the-art theory. In contrast, laser driven experiments which are getting more and more important in atomic and molecular physics, typically involve very high intensity light pulses that probe multi-photon ionisation where, in addition, the strong coherent laser fields can heavily influence the molecules electric fields and potential surfaces. This may prohibit or specifically drive processes that would only occur in similar environments. Here, single photon absorption from low photon flux of the molecular sources is crucial to yield the true “field free” picture of nature. Ideally, both methods should be used complementarily to deepen our understanding of, and to test quantum chemical models of dissociation mechanisms in multi-ionisation.

Paper I compared a relatively simple two-parameter model, already tested for the same molecule in a strong laser field driven experiment. It has been shown to be applicable to other molecular systems in the realm of lasers, which should also be the case for single-photon experiments. Experiments targeting other molecular systems with a strong absorber will further demonstrate the usefulness of the model, e.g. 5-iodouracil [79, 80] or possibly the more complicated diiodomethane [81, 82] with two absorbers.

Papers II-V demonstrated new an interesting fragmentation pathways by observation of the final fragments in comparison to static potential energy surfaces, showing energetically allowed pathways. The unconventional pathway found in SO_2 leading to SO^{2+} paves the way for similar studies in other systems with state selective behaviour. Another possible next step is to fully evaluate the pathways directly by pump probe laser experiments, in comparison to real time molecular dynamics simulations. The numerical investigation of the pathways in paper V are simplified as the added complication of having four atoms creates many uncertainties. Further calculations can be made to complete the picture of the fate of doubly ionised HNCS by investigating rearrangement mechanisms, sequential dissociation and immediate explosion. The fragmentation channel H + C^+ + NS^+ is weakly observed in three- and four-fold electron-ion coincidences above 36 eV, and can clearly be seen in the two-fold ion-ion coincidence map at 41 eV photon energy. This decay channel requires some form of bond rearrangement, which in HNCS is expected to occur above 35 eV where states with minima in the cis or trans configuration start to occur. Pathways where one or two atoms are undetected, such as S^+ + H^+ imply a sequential mechanism or an immediate explosion. In addition, to compare new theory of the weak channels the experimental conditions may need to be tweaked by improving the sample purity as well as collecting data for a longer time. The acquisition time is drastically increasing with the number of particles. E.g. fourfold coincidences require the detection of all created charged particles in double ionisation. However, the acquisition time can be reduced by increasing the overall collection efficiency. Currently, the primary limiting factor is from the detectors themselves where the detection efficiency is determined by the open-area-ratio (OAR), i.e. the area of the holes versus the area of the entire plate. In the current plates the OAR is about 60%, which by switching to a funnel type MCP could be increased to 90% [83].

The simulations of the sequential decay used in paper VI are, for each slope, repeated several thousand times to incorporates a distribution of lifetimes, kinetic energy releases and initial geometry from vibrational modes. Future work should focus on mapping an experimental slope to a lifetime based on a simple function that incorporate the expected slope and the fragment masses. If a mapping could be done quickly in this way, it would substantially speed up the determination of sequential decay lifetimes in new systems. The function should in some form be based on the results of the algebraic model:

$$\text{slope} = -\frac{m_{\mathrm{B}}/m_{\mathrm{BC}} + p_1/p_0 \pm p_2/p_0}{1 + p_1/p_0} \tag{6.1}$$

where m_B is the mass of ion B, m_BC is the mass sum of particles B and C, p_0 is the momentum release in separation of the two primary ions from d_0 to d_sec, p_1 is the momentum release in separation of the primary (A^+) and secondary ion (B^+) from d_sec to infinity. Finally, p_2 is the forward and backward momentum release in the secondary decay, which in most cases is set to zero.

Acknowledgements

My 11 years in physics have gifted me many great experiences and this journey have given me the pleasure of meeting many wonderful people of whom I am immensely grateful.

First, I want to sincerely thank my supervisor Raimund Feifel. During your supervision I have learned much more than a thesis could possibly fit. You took me on my first beamtime, and then eight more, which I consider my most memorable times. The goofy night shifts or ending the day with a beer at the Italian. Nine times in Germany and my vocabulary is still basically limited to “danke” and “morgen”.

I am grateful to Richard Squibb for imparting valuable knowledge about experimental techniques and simulation softwares, along with a pun or two of “Nobel Prize quality”.

I express immense gratitude to Professor John H. D. Eland, whose involvement in every project I undertook was invaluable, with his endless knowledge and commitment to unravelling the truth. I want to thank Majdi Hochlaf for making my papers “sexy”. I also want to thank Gunnar Nyman and Stephen Price for their valuable support with my papers.

As an experimentalist, I really would be nothing without my fellow lab-rats. I wish to express my warmest thanks to my PhD studs Emelie Olsson and Veronica Daver Ideböhn. MLI, I will miss the high quality GIFs. Veronica, I will forever think of you when I see a horoscope. I am grateful for Andreas Hult-Roos and Jonas Andersson. Andreas, I still can’t juggle. Jonas, “alla minns en fegis”. Thanks to all current and former members of the research group, including Dimitris, Hélène, Sylvain, Alex, Marco and Massume.

I extend my respect and gratitude to the monumental structures of Synchrotrons. Special thanks to BESSY II, FLASH, Lund laser lab, and

PETRA III for allowing me to work at these facilities and to SOLEIL for providing data for my first paper.

Thanks to my colleagues at the Department of Physics at GU. Thanks to everyone in administration. Special thanks to the technical staff and technical service for agreeing to do all my odd requests - Ludi, Jan-åke, Lasse, Lennart, Mats, Eddie, Joy.

These past years I have devoted much time to teaching. From my first assignment 'basåret' in 2014 to my last in subatomic physics in 2023, each experience has been truly amazing. I thank everyone involved, every student, and every co-worker, every black board and every textbook. Notable individuals I want to thank include (but are probably not limited to) Jonathan Weidow, Andreas Isacsson, Remi, Christian Forssén, Andreas Heinz and Lars Hellberg.

Jag vill speciellt tacka fysiks uppehållsrum Hilbert och alla dess invånare. Hilbert var min trygga plats där det alltid fanns någon att samtala eller spela dominion med. Jag vill även varmt tacka alla studentföreningar som förgyllt så mycket av min tid. Alla resor med ReKo, CLC och Senil6. Alla möten med IIU. Alla cocktails med HSoCS. Alla julbord med SG-Fysik. Såklart vill jag också tacka alla underbara människor som funnits där för mig de senaste 11 åren - Jesper, Filip, André, Emil, Allan-brallan, Fjället, Piff, Fredrik, Kåre, Nils, Basse, Emelie, Veronica, Louise, Frida, Julia, Annie, Moa, Anesa och Ossian.

Jag vill även tacka min familj. Min mor Gunilla och min far Stefan. Mina syskon Fanny, Amanda och Nellie. Mina bonussyskonen Sebastian, Felicia och Emilia. Alla svågrar, alla syskonbarn och såklart mina svärföräldrar Maria och Jörgen.

Slutligen vill jag tacka min underbara fru Linnéa, Lino, Jack O' Lantern Panic. Vi träffades under mitt första år som doktorand och har haft en otroligt underbar resa tillsammans. Vi har flyttat ihop, skaffat en tredje katt, förlovat oss, gift oss och nu väntar vi en liten pojkskrutt. Från start har du beskrivit min forskning med "Måns jobbar med stora lampor". Nu släcker jag lampan och öppnar dörren för nya framtida äventyr. Tack för allt.

Måns Wallner

Bibliography

[1] J. C. Maxwell, Philos. Trans. R. Soc. London, **155**, 459 (1865).

[2] H. Hertz, Ann. Phys. **267**, 983 (1887).

[3] M. Planck, Ver. Phy. Ges. Berlin **2**, 237 (1900).

[4] A. Einstein, Ann. Phys. **322**, 132 (1905).

[5] J. J. Thomson, London Edinburgh Philos. Mag. & J. Sci. **44**, 293 (1897).

[6] J. J. Thomson, London Edinburgh Philos. Mag. & J. Sci. **24**, 209 (1912).

[7] W. C. Wiley and I. H. McLaren, Rev. Sci. Instrum. **26**, 1150 (1955).

[8] K. Siegbahn, *Esca : atomic, molecular and solid state structure studied by means of electron spectroscopy*, English, "Presented to the Royal Society of Science of Uppsala, Dec. 3rd, 1965." (Uppsala : Alquist and Wiksells, 1967).

[9] B. Brehm and E. von Puttkamer, Z. Naturforsch. A **22**, 8 (1967).

[10] N. Bohr, London Edinburgh Philos. Mag. & J. Sci. **26**, 1 (1913).

[11] W. Heisenberg, Z. Angew. Phys. **43**, 172 (1927).

[12] A. Kramida et al., NIST Atomic Spectra Database (ver. 5.11), [Online]. Available: `https://physics.nist.gov/asd` [2016, January 31]. National Institute for Standards and Technology, Gaithersburg, MD. (visited on 14 Dec. 2023).

[13] B. P. Tsai and J. H. D. Eland, Int. J. Mass Spectrom. Ion Phys. **36**, 143 (1980).

[14] R. D. Molloy et al., Chem. Phys. **335**, 49 (2007).

[15] T. Schneider et al., Phys. Rev. Lett. **89**, `10.1103/PhysRevLett.89.073002` (2002).

[16] T. Pattard et al., J. Phys. B: At. Mol. Opt. Phys **36**, 189 (2003).

[17] J. Andersson et al., Sci. Rep. **9**, 17883 (2019).

[18] P. Auger, J. Phys. Radium **6**, 205 (1925).

[19] L. Meitner, Z. Angew. Phys. **9**, 131 (1922).

[20] B. H. Bransden and C. J. Joachain, *Physics of atoms and molecules* (Longman Science & Technical, 1983).

[21] D. Chattarji, *The theory of auger transitions* (Adacemic Press, 1976).

[22] D. Coster and R. D. L. Kronig, Physica **2**, 13 (1935).

[23] P. Choi and M. Favre, Rev. Sci. Instrum. **69**, 3118 (1998).

[24] J. H. D. Eland et al., Phys. Rev. Lett. **90**, 053003 (2003).

[25] Behlke, *Product lines: hv switch, variable on-time, low coupling capacitance, mosfet, Product code: hts-201-40-lc2*, `https://www.behlke.com/separations/separation_c3.htm`, (visited on 6 Dec. 2023).

[26] NIST, *Strong lines of helium (he)*, `https://physics.nist.gov/PhysRefData/Handbook/Tables/heliumtable2.htm`, (visited on 31 Jan. 2024).

[27] A. M. Flank et al., Nucl. Instrum. Methods Phys. Res. B **246**, 269 (2006).

[28] P. S. Miedema et al., JLSRF **2**, `10.17815/jlsrf-2-79` (2016).

[29] S. Plogmaker et al., Rev. Sci. Instrum. **83**, `10.1063/1.3677329` (2012).

[30] Hammatsu, *Electron multiplier tube, Product code: r595*, `https://www.hamamatsu.com/us/en/product/optical-sensors/electron_ion-sensor/em/R595.html`, (visited on 12 Jan. 2024).

[31] P. Kruit and F. H. Read, J. Phys. E: Sci. Instrum. **16**, 313 (1983).

[32] A. E. Cameron and J. Eggers D. F., Rev. Sci. Instrum. **19**, 605 (2004).

[33] W. E. Stephens, Bull. Am. Phys. Soc. **21**, 22 (1946).

[34] M. M. Wolff and W. E. Stephens, Rev. Sci. Instrum. **24**, 616 (2004).

[35] J. H. D. Eland and R. Feifel, Chem. Phys. **327**, 85 (2006).

[36] O. Edqvist et al., Phys. Scr. **1**, 25 (1970).

[37] J. H. D. Eland et al., Sci. Rep. **10**, `10.1038/s41598-020-59217-7` (2020).

[38] V. Ideböhn et al., Phys. Chem. Chem. Phys. **24**, 786 (2022).

[39] A. Hult Roos et al., Phys. Chem. Chem. Phys. **21**, 9889 (2019).

[40] J. H. D. Eland, Mol. Phys. **61**, 725 (1987).

[41] J. H. D. Eland, Laser Chem. **11**, 259 (1991).

[42] C. Hampel et al., Chem. Phys. Lett. **190**, 1 (1992).

[43] M. J. O. Deegan and P. J. Knowles, Chem. Phys. Lett. **227**, 321 (1994).

[44] P. J. Knowles et al., Chem. Phys. **112**, 3106 (2000).

[45] R. A. Kendall et al., J. Chem. Phys. **96**, 6796 (1992).

[46] D. E. Woon and T. H. Dunning, J. Chem. Phys. **98**, 1358 (1993).

[47] T. H. Dunning et al., Chem. Phys. **114**, 9244 (2001).

[48] T. Trabelsi et al., Chem. Phys. **149**, 064304 (2018).

[49] T. Helgaker et al., J. Chem. Phys. **106**, 9639 (1997).

[50] C. Puzzarini, J. Phys. Chem. A **113**, PMID: 19799385, 14530 (2009).

[51] P. J. Knowles and H.-J. Werner, Chem. Phys. Lett. **115**, 259 (1985).

[52] H.-J. Werner and P. J. Knowles, Chem. Phys. **82**, 5053 (1985).

[53] H.-J. Werner and P. J. Knowles, Chem. Phys. **89**, 5803 (1988).

[54] P. J. Knowles and H.-J. Werner, Chem. Phys. Lett. **145**, 514 (1988).

[55] K. R. Shamasundar et al., Chem. Phys. **135**, 054101 (2011).

[56] T. Shiozaki et al., J. Chem. Phys. **134**, 034113 (2011).

[57] T. A. Carlson and R. M. White, J. Chem. Phys. **44**, 4510 (1966).

[58] *SIMION: The field and particle trajectory simulator. Version 8.1.0.47.*

[59] K. Motomura et al., J. Phys. Chem. Lett. **6**, 2944 (2015).

[60] P. R. Bevington, *Data reduction and error analysis for the physical sciences* (MrGraw Hill, New York, 1969).

[61] J. Berkowitz, *Photoabsorption, photoionization, and photoelectron spectroscopy* (Adacemic Press, 1979).

[62] M. Berger et al., *Xcom: photon cross sections database*, `https://www.nist.gov/pml/xcom-photon-cross-sections-database`, (visited on 26 Feb. 2024).

[63] G. Dujardin et al., Chem. Phys. **88**, 339 (1984).

[64] D. Curtis and J. Eland, Int. J. Mass Spectrom. Ion Processes **63**, 241 (1985).

[65] M. Hochlaf and J. H. Eland, J. Chem. Phys. **120**, 6449 (2004).

[66] T. A. Field and J. H. Eland, Int. J. Mass Spectrom. **192**, 281 (1999).

[67] M. Jarraya et al., Sci. Rep. **11**, `10.1038/s41598-021-96405-5` (2021).

[68] M. Wallner et al., Sci. Adv. **8**, 5411 (2022).

[69] G. Dujardin et al., Chem. Phys. **88**, 339 (1984).

[70] A. Ben Houria et al., J. Chem. Phys. **122**, 054303 (2005).

[71] A. Ben Houria et al., J. Chem. Phys. **124**, 054313 (2006).

[72] NIST, *Atomic spectra database levels form*, `https://physics.nist.gov/PhysRefData/ASD/levels_form.html`, (visited on 23 Feb. 2024).

[73] M. N. R. Ashfold and S. R. Langford, ‘Spectroscopy and photochemistry of rydberg states of small polyatomic hydride molecules’, in *The role of rydberg states in spectroscopy and photochemistry: low and high rydberg states*, edited by C. Sándorfy (Springer Netherlands, Dordrecht, 1999), pp. 23–56.

[74] M. Jarraya et al., Phys. Chem. Chem. Phys. **25**, 19435 (2023).

[75] V. Brites et al., Chem. Phys. **346**, 23 (2008).

[76] S. Zhao et al., Phys. Rev. A **99**, `10.1103/PhysRevA.99.053412` (2019).

[77] T. Endo et al., Front. Chem. **10**, `10.3389/fchem.2022.859750` (2022).

[78] S. Lias et al., *Gas-phase ion and neutral thermochemistry*, Vol. 17, J. Phys. Chem. Ref. (American Chemical Society and the American Institute of Physics, 1988).

[79] K. Nagaya et al., Faraday Discuss. **194**, 537 (2016).

[80] H. Fukuzawa and K. Ueda, Adv. Phys.: X **5**, 1785327 (2020).

[81] H. Fukuzawa et al., Nat. Commun. **10**, 2186 (2019).

[82] T. Takanashi et al., Phys. Chem. Chem. Phys. **19**, 19707 (2017).

[83] Hammatsu, *MCP (microchannel plate) assembly*, `https://www.hamamatsu.com/content/dam/hamamatsu-photonics/sites/documents/99_SALES_LIBRARY/etd/MCP_assembly_TMCP0003E.pdf`, (visited on 31 Jan. 2024).